BRNO UNIVERSITY OF TECHNOLOGY
VYSOKÉ UČENÍ TECHNICKÉ V BRNĚ

FACULTY OF ELECTRICAL ENGINEERING AND COMMUNICATION
FAKULTA ELEKTROTECHNIKY
A KOMUNIKAČNÍCH TECHNOLOGIÍ

DEPARTMENT OF BIOMEDICAL ENGINEERING
ÚSTAV BIOMEDICÍNSKÉHO INŽENÝRSTVÍ

FLUORESCENT METHODS IN RESEARCH OF EUKARYOTIC CELLS

FLUORESCENČNÍ METODY VÝZKUMU EUKARYOTICKÝCH BUNĚK

DOCTORAL THESIS
DIZERTAČNÍ PRÁCE

AUTHOR AUTOR PRÁCE	Larisa Chmelíková
SUPERVISOR ŠKOLITEL	prof. Ing. Ivo Provazník, Ph.D.

BRNO 2021

ABSTRACT

This work examines the application of the fluorescent methods in use in *in vitro* studies to the field of cardiac tissue regeneration. Confocal fluorescence microscopy is an appropriate microscopic technique for studies in this field because it enables the visualisation of 3D structures and cell distribution in 3D models. The applied fluorescent markers should remain stable for a long period, are biocompatible, and are non-toxic for living cells. Nanoparticles such as superparamagnetic iron oxide nanoparticles (SPION) are currently very popular, and many studies have shown that they are suitable for long-term experiments. This research makes use of rhodamine-derived superparamagnetic maghemite nanoparticles (SAMN-R) and describes their excitation and emission spectra, size, and location within cells. A toxicity assay was performed by measuring reactive oxygen species (ROS) and non-quantitative measurements were conducted using fluorescence microscopy, confirming that a dose value of 20 $\mu g \cdot cm^{-2}$ is optimal for the treatment of living cells. This research also looks at the effects of SAMN-R treatment on cell proliferation and motility. The 3T3 fibroblast cell line was used for the cell proliferation test and scratch assay, after which human adipose-derived mesenchymal stem cells (MSCs) were used to examine single-cell migration. The subsequent statistical analysis revealed that it cannot be confirmed that the SAMN-R treatment exerts a significant effect on either cell proliferation or collective and single-cell migration, and it can be assumed that SAMN-R are appropriate fluorescent cell markers for living cells research, including the field of regeneration studies. Adipose-derived MSCs have enormous potential for cardiac tissue regeneration. Their interactions with HL-1 cardiac muscle cell line were studied using the scratch assay, and this model seems to be a promising and useful way to study cell-to-cell contact and its role in cell repairing.

KEYWORDS

Fluorescence, confocal microscopy, mesenchymal stem cells, cell migration, superparamagnetic iron oxide nanoparticles.

ABSTRAKT

Tato práce zkoumá aplikaci fluorescenčních metod používaných v *in vitro* studiích v oblasti regenerace srdeční tkáně. Konfokální fluorescenční mikroskopie je vhodnou mikroskopickou technikou pro výzkum v této oblasti, protože umožňuje vizualizaci 3D struktur a distribuce buněk ve 3D modelech. Používané fluorescenční markery by měly být dlouhodobě stabilní, biokompatibilní a netoxické pro živé buňky. V současné době je použití nanočástic jako superparamagnetické nanočástice oxidu železa (SPION) velmi populární; velké množství studií ukazuje, že jsou vhodné pro dlouhodobé experimenty. Tento výzkum využívá superparamagnetické maghemitové nanočástice s vázaným rhodaminem na jejich povrchu (SAMN-R) a popisuje jejích excitační a emisní spektrum, velikost a lokalizaci v buňkách. Stanovení toxicity bylo provedeno měřením reaktivních forem kyslíku (ROS) a nekvantitativním měřením pomocí fluorescenční mikroskopie bylo zjištěno, že hodnota dávky 20 $\mu g \cdot cm^{-2}$ je optimální pro aplikaci na živé buňky. Dále byl zkoumán vliv aplikace SAMN-R na buněčnou proliferaci a motilitu, kdy ve studii buněčné proliferace a *scratch assay* byla použita buněčná linie fibroblastů 3T3. Poté byla studována migrace jednotlivých buněk s použitím mezenchymálních kmenových buněk (MSCs), izolovaných z lidské tukové tkáně. Následná statistická analýza nepotvrdila, že by aplikace SAMN-R měla významný vliv na buněčnou proliferaci, kolektivní migraci nebo na migraci jednotlivých buněk. Lze tedy předpokládat, že SAMN-R jsou vhodným fluorescenčním markerem pro výzkum živých buněk, včetně experimentů v oblasti regenerace tkáně. MSC buňky izolované z tukové tkáně mají velký potenciál v regeneraci srdeční tkáně. Jejich interakce s buněčnou linií srdečních svalových buněk HL-1 byly studovány pomocí *scratch assay,* kdy se tento model jeví jako nadějný a vhodný pro studium buněčných kontaktů a jejich roli při regeneraci buněk.

KLÍČOVÁ SLOVA

Fluorescence, konfokální mikroskopie, mezenchymální kmenové buňky, migrace buněk, superparamagnetické nanočástice oxidu železa.

BIBLIOGRAPHIC CITATION

CHMELÍKOVÁ, Larisa. *Fluorescent methods in research of eukaryotic cells.* Brno, 2021, 118 s. Doctoral thesis. Brno University of Technology, Faculty of Electrical Engineering and Communication, Department of Biomedical Engineering. Doctoral thesis supervisor: prof. Ing. Ivo Provazník, Ph.D.

DECLARATION

I declare that I have written the doctoral thesis titled “Fluorescent methods in research of eukaryotic cells” independently, under the guidance of the supervisor, and using the technical literature and other sources quoted within the thesis and detailed in the list of literature in the final section.

As the author of thesis, I furthermore declare that, as regards the creation of the work, I have not infringed any copyright. In particular, I confirm that I have not violated anyone’s personal and/or ownership rights and I am fully aware of the consequences of breaking Regulation § 11 of the Copyright Act No. 121/2000 Coll., as amended, and intellectual property rights or changes in related Acts (the Intellectual Property Act), as amended, inclusive of possible consequences resulting from the provisions of the Criminal Act No. 40/2009 Coll., Section 2, Head VI, Part 4.

Brno, …………………….. ………………………………..

Larisa Chmelíková

ACKNOWLEDGEMENT

I would like to thank all the people who supported me during my doctoral studies. Especially, I would like to thank my supervisor prof. Ing. Ivo Provazník, Ph.D. for his interest and professional mentoring. Furthermore, I wish to thank my colleagues for support, constructive and suggestive discussions during my studies. I especially grateful to colleagues with whom I was fortunate enough to work on conference and journal papers. Also, I would like to thank colleagues from Department of Physiology (Masaryk University, Brno) and Department of Pharmacology and toxicology (Veterinary Research Institute, Brno) for providing access to their laboratories, cells, some materials and consultations. Furthermore, I wish to thank Regional Centre of Advanced Technologies and Materials (Palacký University, Olomouc) for providing nanoparticles. I also acknowledge institutional support given by project CZ.02.1.01/0.0/0.0/16_017/0002581, namely "Development of infrastructure for interdisciplinary research of technologies in biomedicine and bioinformatics" whereby excellent conditions for the research in the Department of Biomedical Engineering have been created. Special thanks belong to my family and friends for their great patience and generous support.

Brno, …………………….. ………………………………..

Larisa Chmelíková

TABLE OF CONTENTS

1 INTRODUCTION

Mesenchymal stem cells (MSCs) are widely used in tissue engineering and regenerative medicine research [1, 2]. The most common sources of MSCs are bone marrow and adipose tissue due to the presence of a large number of these cells, the simplicity of the procedure, and most importantly, the lower risk for the patient that this method represents. The adipose tissue that is removed during a routine liposuction procedure is widely used in *in vitro* experiments because it is a waste product, and therefore there is no need to expose patients to additional risks to isolate cells for research. The bone marrow aspirate procedure offers a lower risk of morbidity and mortality, but the number of cells obtained from adipose tissue is usually larger than that from bone marrow aspiration. The choice of which procedure to perform tends to depend on the required number of isolated cells [1, 3]. MSCs have the ability to differentiate into a variety type of cells such as osteoblasts, adipocytes, chondroblasts, hepatocytes, myoblasts, epithelial cells, cardiomyocyte-like cells, and neuron-like cells, which is one of the reasons for their widespread use in regeneration and therapy [2, 4]. Their main areas of application are bone regeneration [5, 6], liver regeneration [7, 8], cardiovascular regeneration [9, 10], skin regeneration [11, 12], neuronal regeneration [13, 14], cartilage defect repair [15, 16], corneal reconstruction [17, 18], and tracheal reconstruction [19, 20], among others.

The effect of acute myocardial infarction (MI) on MSCs is a significant field of study. The process of regeneration depends on the ability of cells to migrate towards the necrotic cells that result from a MI [21–23]. Studies have shown that MSCs can express different amounts of growth and regenerative factors, cytokines, and chemokines. This occurs during tissue regeneration, which is a process that is still not fully understood. Studies of directional cell migration toward concentrations of various immunomodulatory factors are often performed in microfluidic chambers and scaffolds [24, 25], while transwell chambers with porous membranes are also used to create gradients of chemokine concentrations [26].

Various types of MSCs (including adipose-derived and bone marrow varieties) have the potential to differentiate into cardiomyocyte-like cells in certain *in vitro* cultivation conditions such as during long-term cultivation in a culture medium containing 5-azacytidine [27–30]. Different types of co-culture experiments have been performed to come to a better understanding of cells' involvement in cardiac tissue regeneration. In the study [31], porcine bone marrow MSCs and freshly isolated porcine primary adult cardiomyocytes were co-cultured in a transwell chamber with a porous membrane. Here, cells are cultured without contact, which makes it possible to study the effect of chemokines and growth factors. The results show that cardiomyocytes in a co-culture with MSCs display better survival and viability, without affecting the main mitochondrial and contractile functional parameters. In a previous study our team used bone marrow MSCs and adult cardiomyocytes isolated from rat hearts, and in that case, the wells with different types of cells were separated by a small collagen-filled tunnel [32]. We looked at the effects of chemotaxis and collagen fibrils orientation but, in these examples, the cells did not make contact. Cell-to-cell contact was examined in study [33], where human bone marrow MSCs and cardiomyocytes isolated from the hearts of rat embryos were placed in co-culture. The communication pathways between the cells were also considered [33].

Both *in vitro* and *in vivo* studies have been carried out and many of the latter have revealed successful MSC grafts by either intravenous injections or injections to a damaged tissue (the infarct zone) [9, 26, 34–39]. Despite the fact that a large amount of research has already been published, the use of MSCs in therapy may contribute to complications such as tumorigenicity, proinflammation, and fibrosis, proving that further research in this field is still necessary [40, 41]. Cardiac tissue engineering is currently an expansive area of research in this field [42]. It often focuses on the development of biocompatible scaffolds of various shapes with appropriate conditions for cell culture. The MSCs cultured in these scaffolds can be used as substitutes for infarcted cells, which makes it possible to keep grafted cells on damaged tissue. The development of the field of tissue engineering has the potential to significantly improve cardiac tissue regeneration.

For experiments that make use of cell tissues and scaffolds, it is necessary to track cells in 3D space [25, 43, 44], and it is for this purpose that fluorescent dyes are widely used. Confocal fluorescence microscopy makes it possible to determine the location of stained cells in complex scaffolds including structures such as fibres, pores, and uneven surfaces. Unfortunately, most fluorescent dyes are not suitable for live cell imaging or long-term experiments and therefore, in addition to the standard method of cell staining, it is necessary to consider alternative options such as superparamagnetic iron oxide nanoparticles (SPION). In the first studies performed they were used as contrast agents for diagnostic imaging [45, 46] but, currently, they are often used to mark cells to track methods of treatment. Iron oxide nanoparticles including magnetite (Fe_3O_4) and maghemite (γ-Fe_2O_3) are widely used in diagnostics and therapy in biomedical research [47, 48], being suitable for areas such as drug delivery [49], tumour and cancer therapy [50, 51], hyperthermia therapy [52], cardiovascular research [45, 53], and magnetic resonance imaging (MRI) [48, 54]. Their surface can be modified with coatings such as targeting ligands, drugs, biopolymers, proteins, and fluorescent markers [55, 56]. The choice of which nanoparticles to use for a particular application can be made based on their magnetic properties, which differ depending on the composition of the core and size [50]. It is also necessary to pay attention to properties such as biocompatibility, biodegradability, and toxicity [56, 57].

This work studies the properties of rhodamine-derived superparamagnetic maghemite nanoparticles (SAMN-R), which in previous studies have been applied to treat rat bone marrow MSCs and human adipose-derived MSCs. Following the use of microscopic techniques, it was determined that SAMN-R penetrate the intracellular compartment by endocytosis, so are localized in the endosomes or lysosomes surrounding cell nuclei [58–60]. SAMN-R also show long-term fluorescence stability [61]. This work includes a study of the spectral properties and toxicity of SAMN-R, the effect on viability, morphology, and motility of their application to cells, and the suitability of SAMN-R for use in long-term experiments. Further investigation of their properties will help to assess their applicability in biomedical applications.

2 BACKGROUND FOR FLUORESCENT METHODS IN *IN VITRO* STUDIES

2.1 FLUORESCENCE WIDEFIELD AND CONFOCAL MICROSCOPY

Light microscopy gives us a 2D representation of a physical object. In a widefield microscope, we usually observe the projection of a 3D physical structure into a 2D surface. Thus, information from one dimension that significantly limits our perception of the observed object is lost. Generally, current biochemical research focuses on determining the 3D structures from the observed biological samples. Monitoring the 3D organization of cellular structures is essential for the ability to interpret their function. The contrast microscopic techniques, such as phase contrast microscopy (PCM), differential interference contrast (DIC), integrated modulation contrast (IMC), are often used to observe biological samples. These microscopic methods provide more information about the shape and surface of biological objects compared to light microscopy. Nevertheless, the study of 3D structures, such as tissue sections and cells in the scaffolds, is problematic. However, advanced fluorescence microscopy allows us to obtain more information about the structure of biological samples. A wide range of fluorescent dyes is available for imaging various cellular organelles and tissue structures. In addition, it is possible to use several dyes simultaneously when a competent choice is based on their spectrum, chemical structure and method of interaction with biological samples. It is commonly used for study cells morphology, intracellular distribution of filaments, intracellular ion concentrations, cell junctions, cell adhesion, cell viability, cell migration and motility. [62]

Fluorescence microscopy is a microscopy technique that is intended to view samples stained with fluorophores (fluorochromes) or have intrinsic fluorescence. The fluorescence phenomenon is the basis of fluorescence microscopy. Fluorescence is the emission of photons by atoms or molecules whose electrons are transiently stimulated to a higher excitation state by radiant energy from an outside source [62]. A fluorescent molecule absorbs a photon of excitation light. Therefore, the energy level of the electron is raised to an excited state. Then the photon is emitted with reduced energy and brings the electron back to its ground state. This is depicted graphically in the Jablonski diagram shown in Figure 1 (A). Since the energy of photon usually is reduced during absorption and emission, their wavelength is increased (Planck's law). [62–64]

The fluorophores have the specific excitation and emission wavelengths. The distance between the maxima of the excitation and emission spectra (Stokes Shift) and the widths of spectra are important parameters of fluorophores (Figure 1 (B)). When their wavelengths greatly overlap, then the detection of emitted fluorescence can be difficult to distinguish from the excitation light. This is important to consider when using several dyes simultaneously. When the spectra of two fluorochromes are overlap, then it is difficult to excite or detect the emission from those fluorophores separately. [62, 63]

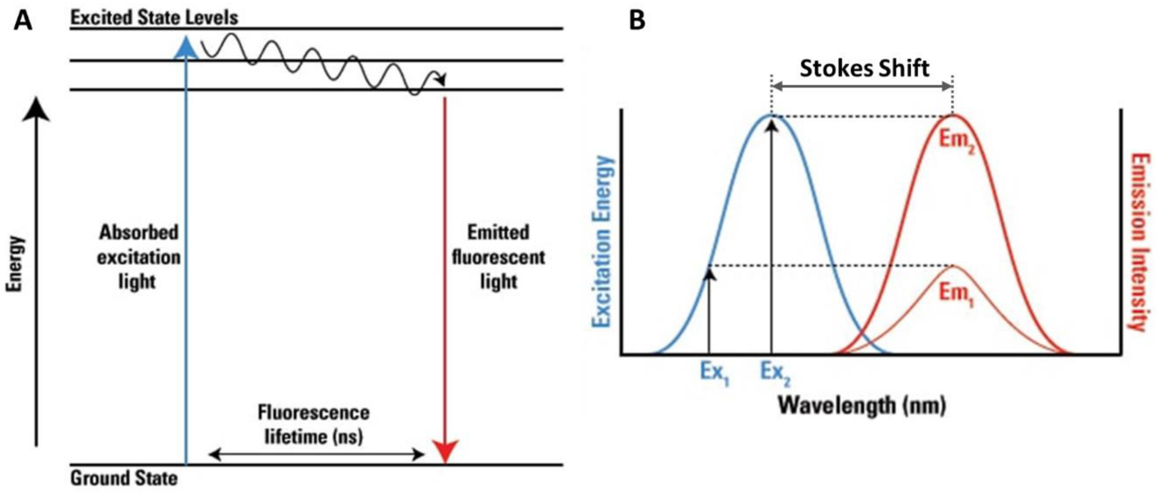

Figure 1. Fluorescence fundamentals. (A) Jablonski energy diagram of fluorescence. (B) The excitation and emission spectra of a fluorophore and the correlation between the excitation amplitude and the emission intensity. The intensity of the emitted light (Em_1 and Em_2) is directly proportional to the energy required to excite a fluorophore at any excitation wavelength (Ex_1 and Ex_2, respectively). [63]

In Figure 2 (A) the optical principle of widefield fluorescence microscopy is shown. Light from the source passes through the excitation filter, thereby further only light of a certain wavelength passes, then it is reflected from dichroic mirror and get to the specimen through the objective. In this case, the entire specimen of study is exposed to the light source. The excitation wavelength is absorbed by the fluorophore and promote to emit at a longer wavelength. The emitted light from the specimen passes through the objective, dichroic mirror and emission filter, and then detected with help of ocular or detector (Figure 2). Unfortunately, in this method the light emitted by the specimen is detected from region in focus as well as in out-of-focus, therefore the image is usually blurred (Figure 3 (A)). For widefield fluorescence microscopy the visualization of thick biological samples, such as tissue sections and cells in the scaffolds, can be complicated because strong fluorescent signals from objects outside the focal plane cause a low-contrast image. This problem is solved in the construction of a confocal microscope by adding a light source pinhole aperture (excitation) and a detector pinhole aperture (emission) (Figure 2 (B)). The excitation light passes through the pinhole and excitation filter, and then limited beam reflected by the dichroic mirror and directed to through objective a specimen region in a focus plane. Emitted light passed through the objective, dichroic mirror, emission filter and then only beams from a focus plane pass through the detector pinhole. Thereby, the out-of-focus plane light reduces. Photomultiplier Tubes (PMT) convert fluctuations in intensity of emitted light into voltage fluctuations. This analogue signal is digitized by an analogue-to-digital converter to display an image of field of view composed of generated pixels on the computer monitor using integrated software. To acquire an image of field of view, the laser beam scans across the specimen by a raster scanning mechanism. This method makes possible to acquire a stack of images from different focal planes in Z-axis separately and after that allows a 3D reconstruction of scanned field of specimen without blur (Figure 3 (B)). This collection of images is called a "z-stack" and can be represented as a 3D matrix. In addition, multidimensional data can be created with the image in multiple channels or at time intervals which create an additional dimension. [62, 65]

Mercury and xenon arc lamps and a monochromatic light from a laser are commonly used as a light source for fluorescence microscopy. The arc lamps also may be used in confocal microscopy, but a great loss of light when passing through pinhole aperture must be considered. Most laser sources that emit only a single wavelength are commonly used as a light source in confocal microscopy. Also, there are some gas lasers which can emit several lines simultaneously, but in a narrow range. Liquid and solid lasers in categories of tunable lasers are also used, but their emission wavelength can be tuned only on single line in a time. Nevertheless, to cover the visible range a complex included several lasers may be constructed. [62, 65]

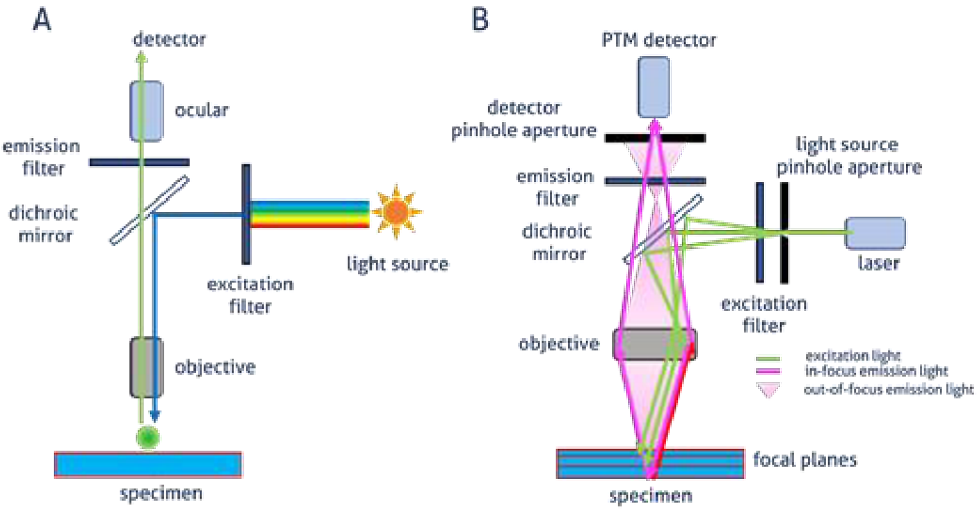

Figure 2. Image generation in (A) widefield epifluorescence and (B) confocal microscopes. [66]

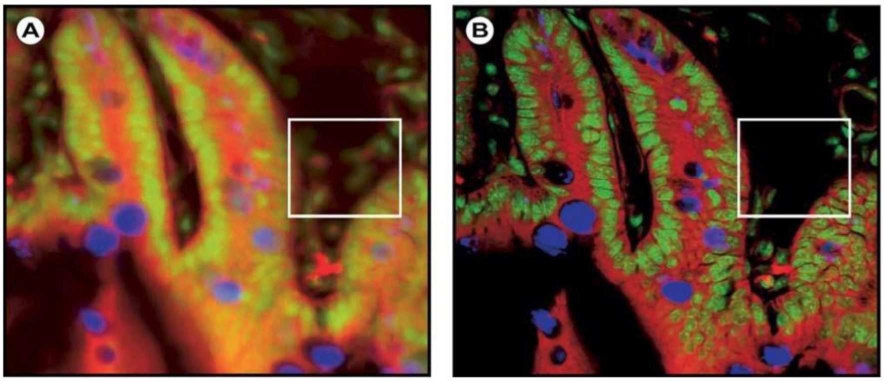

Figure 3. Widefield (A) and confocal (B) image of a triple-labelled cell aggregate (mouse intestine section). Demonstration of the presence of blurred and out-of-focus plane details in the widefield image (white square). [67]

In this work Leica TCS SP8 X confocal microscope was used. This confocal microscope has an advanced technical construction (Figure 4). It is equipped with white light laser (WLL) [68]. This light source consists of fibre IR laser which emits light pulses (80 MHz), that subsequently amplified in a diode-pumped laser amplifier. These high energy pulses (10 W) are finally focused on the entry surface of a photonic crystal fibre (PCF). The PCF is a solid supercontinuum generator. Then the emitted beam enters to an acousto-optical tunable filter (AOTF), which can select a distinct excitation wavelength (a narrow spectral band with bandwidth in the range of 1–3 nm, depending on the wavelength). This is optically transparent crystal which deflect selected wavelength based on a frequency of the acoustic excitation. Hereby, it is possible to set any needed excitation wavelength from 470 to 670 nm. Also, it is possible to use eight excitation wavelengths at a time with a minimum interval of 5 nm. In this case the using of dichroic mirror to separate the excitation and emission signals is difficult. The spectral parameters of the mirror are not modifiable, so it is necessary to include a large number of these beam splitters to construction that is technically insoluble task. The acousto-optical tunable beam-splitter (AOBS) is used to separate the excitation and emission signals. AOBS is made of paratellurite (TeO_2) crystal, which has good optical properties and is transparent from below 350 nm to more than 5 µm. AOTF uses the birefringence property of TeO_2 for the diffraction mechanism. The crystal density is changed when it is affected by applying a mechanical wave at radiofrequencies. The change in density affects the change in refractive index. Thus, AOBS deflects the selected excitation wavelength in the direction of the optical path. [69, 70]

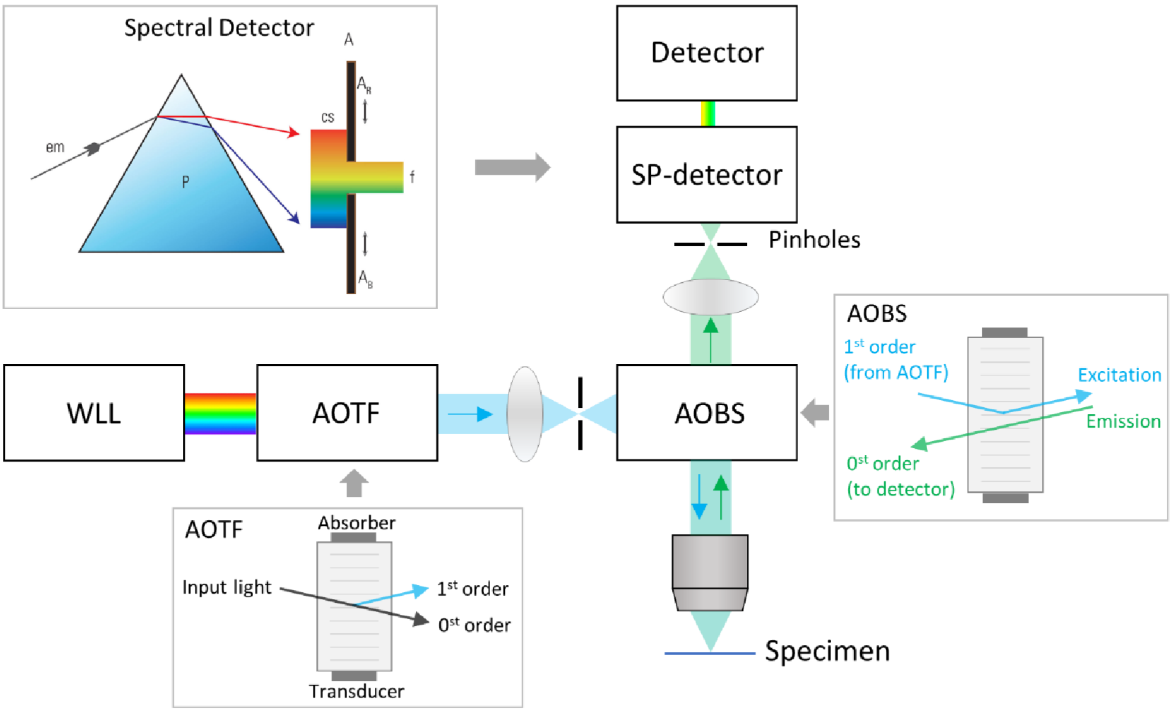

Figure 4. The scheme of an advanced technical construction of the confocal microscope. White laser light is generated by amplified IR pulsed laser light which is fed through a photonic crystal fibre. An acousto-optical tunable filter (AOTF) is employed to extract a series of variously coloured bandlets from the white emission of the supercontinuum source. The acousto-optical beam splitter (AOBS) can steplessly and simultaneously adapt to any given series of excitation colours. Spectral detector (SP-detector) employing a glass prism for high transmission and white performance. [71] The spectrum is separated into bands by means of movable mirror sliders.

The emission light from the focal plane passes through AOBS and pinhole, then passes to the spectral detector (SP-detector). Using the SP-detector allows to control the bandwidth of the detected emission bands. The emitted light passes through a dispersive prism. From the obtained colour spectrum, the desired bandwidth is selected by setting movable barriers. The SP-detector may split emission light into up to five spectral bands. Then the light in each band is detected by a PMT or a Hybrid Detector (HyD). [71, 72]

The widespread use of fluorescence microscopy has given the motivation to improve technologies and to develop new approaches aimed at improving the resolution that is limited by light diffraction. Advanced super-resolution microscopic methods achieve lateral resolution of less than 200 nm and axial resolution of less than 600 nm. For example, stimulated emission depletion microscopy (STED) [73] achieves a lateral resolution of about 30 nm. This method uses an additional high power depletion laser (STED laser) with a higher wavelength than excitation, which has a donut shape in cross-section. The donut-shaped pattern is typically generated by inserting a phase mask into the light path. The resolution is improved due to the quenching of the fluorescence at the edge of the illuminated area, and the generation of fluorescence occurs only in the unquenched area inside the donut-shaped pattern. Reversible saturable optically linear fluorescence transitions (RESOLFT) microscopy is based on a similar principle. Unlike STED microscopy, this method does not require the use of a high-intensity laser, thus has less probability of causing phototoxicity in living biological samples. However, this method focuses on fluorescent probes that can be reversibly photoswitched between fluorescent and non-fluorescent states, which in turn limits the use of this method by the choice of fluorophores. This type of fluorophore is used in stochastic optical reconstruction microscopy (STORM) [74], photoactivated localization microscopy (PALM) [75] and fluorescence photoactivation localization microscopy (FPALM) [76] which are based on the same principles. In these approaches, fluorescent molecules activated and localized at different time points. These techniques improve resolution to 20 nm in the lateral axis and 50 nm in the axial axis. [77]

Another possible way to increase spatial resolution is to use image processing capabilities. For example, deconvolution algorithms are used in both confocal and widefield fluorescence microscopy. In the second case, a blurred image is a standard problem due to the capture of signal in out-of-focus planes. This noise is easily removed using these algorithms. One of the modern solutions combines technical capabilities of CCD camera and methods of image processing. The z-stacks are obtained by alternately sharpening images in several planes. Then 3D reconstruction with a resolution close to confocal microscopy can be formed from the obtained image sequence. [65, 78]

Light-sheet fluorescence microscopy (LSFM) is another interesting technology of widefield microscopy, which allows to obtain 3D images. In this modification widefield fluorescence microscopy is combined with optical sectioning. A thin slice of excitation beam passes perpendicular to observed sample and objective. A thin optical section is obtained from the focal plane. The thickness and size of the field of view depend on the numerical aperture of the objective lens and the depth of focus of the excitation beam.

The z-stack can be acquired by the acquisition of the section from several planes, which can be used in 3D image reconstruction. [79]

The advanced technology and the development of new fluorescent dyes help taking scientific research to the next level. The study of biological samples at the cellular level and at the molecular level has great prospects.

2.2 IRON OXIDE NANOPARTICLES AS FLUORESCENT IMAGING PROBES

Currently, in the modern studies the nanoparticles from various materials are widely used in the field of therapeutics and diagnostics [47, 48, 80]. Nevertheless, the application of developed technologies in medicine is still challenging. Nanoparticles developed from various materials have the different properties. In this work the superparamagnetic iron oxide nanoparticles (SPION) were of interest. Generally, SPION have a magnetite (Fe_3O_4) or maghemite (γ-Fe_2O_3) structure. Their surface can be coated with polymers, carbonic acids, enzymes, proteins, fluorescent probes, etc. (Figure 5). The surface improvement gives a new facility in their application in the biomedical field of research. Also, SPION do not show a toxic effect on life cells. However, their effect may depend on the applied dose. [55, 56, 81]

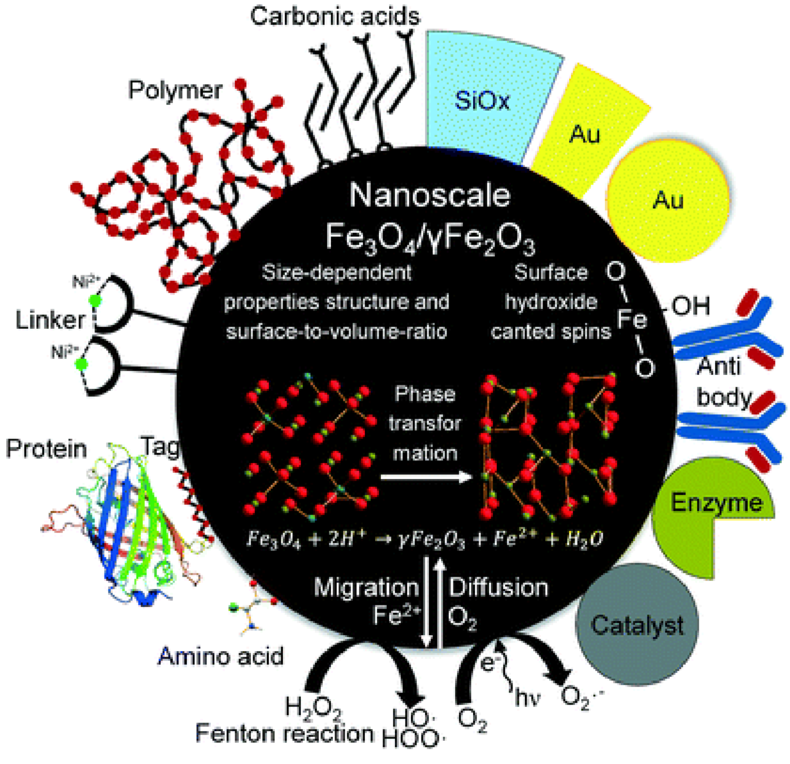

Figure 5. Schematic illustration of different applications, structural transformations and surface interactions of nanoscale iron oxide nanoparticles. [81]

The implementation of SPION on *in vivo* research requires initial *in vitro* studies. One of their widespread use is the marking of cells of tissues for magnetic resonance imaging (MRI) [45, 46, 48, 54, 82, 83]. In this case MRI is non-invasive technique to visualization of SPION localization in 3D structure [84]. Also, due to their magnetic properties it can be possible to manipulate them mechanically by magnetic field. This may have the application in transporting of marked cells or drugs to desired location in *in vivo* research [83, 84].

Also, SPION are often used in gene delivery research [49]. Gene delivery is used to modify cell functions that are helpful in therapeutic, gene therapy, and vaccine applications [85]. For example, cells are genetically modified for ability to express functional ion channels, growth factors, antibodies, and viral vectors. Plasmids can be successfully delivered to intracellular compartment by magnetofection [86, 87]. Usually, the surface of nanoparticles is coated with biocompatible polymers such as Polyethyleneimine (PEI), Poly-l-lysine (PLL), Polyethylene Glycol (PEG), that have improved DNA binding capabilities to their surface [88]. Then, nanoparticles improved with that method can entry to intracellular by endocytosis (Figure 6) or magnetic field generated with an external magnet. The use of this method helps to increase the efficiency of DNA delivery and gene expression [89, 90].

Furthermore, several experimental applications of SPION include tumour and cancer therapy [50, 51], hyperthermia therapy [52], cardiovascular research [45, 53], and other fields. Currently, 3D structures are used in many fields of *in vitro* studies. They include measurements on the tissue and various biocompatible scaffolds and ECM gels, especially in cardiac tissue engineering field [36]. In this case the fluorescence microscopy is widely used for imaging of 3D structures and cell distribution in the 3D models. Stable for a long time, non-toxic and biocompatible fluorescent markers are needed for using this technique. For this purpose, nanoparticles labelled with fluorescent dyes can be suitable [91–95].

There are many factors that can affect a success of cell labelling with nanoparticles: size and shape of nanoparticles, their surface chemistry, charge, type of cells, pH of environment, and other [80, 96–99]. Usually, small nanoparticles with size up to 10 nm (up to 30 nm according to some studies) penetrate passively through cell membrane. Larger nanoparticles interact generally with receptors on the surfaces of cells and are internalized into endosomes by endocytosis (Figure 6). The dose of nanoparticles incorporated into endosomes is random, because number of nanoparticles interacting with the cellular membrane is various [59, 100]. [101–105]

The ability to penetrate to intracellular compartment can be affected by the stability of nanoparticles in the used environment. Usually, iron oxide nanoparticles have colloidal stability in water [92, 96]. However, their properties are changing in the cell growth medium, which contains proteins that affect the surface charge distribution of oxides. This changes zeta-potential to lower values. Thus, nanoparticles are loosely bound and form clusters. This can affect the way of nanoparticles penetration. The cellular uptake of clusters by endocytosis dominates over the uptake of individual nanoparticles by diffusion. [96]

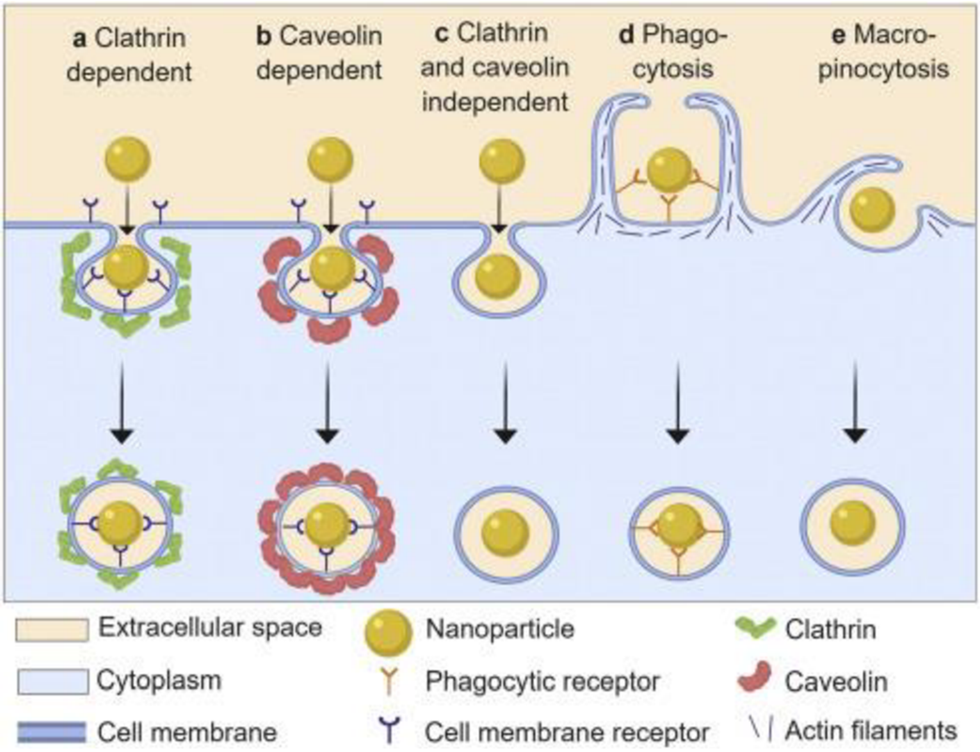

Figure 6. Schematic overview of nanoparticle uptake pathways *via* endocytosis. Multiple different pathways exist for cellular entry of nanoparticles *via* endocytosis mechanisms: (a) clathrin-dependent; (b) caveolin-dependent; (c) clathrin- and caveolin-independent; (d) phagocytosis; and (e) macropinocytosis pathways. These nanoparticle cell uptake pathways are mechanistically distinct and highly regulated at the biomolecular level. The pathway by which nanoparticles enter cells is important, as it determines intracellular nanoparticle transport and corresponding biological response and therapeutic effect. [80]

Furthermore, nanoparticles can have a toxic effect on living cells. Depend on the size, shape, surface coating SPION can promote apoptosis, necrosis, inflammation, etc. SPION can cause cellular toxicity by induction of oxidative stress. The increased production of reactive oxygen species (ROS) can affect the functions of organelles, such as mitochondria and nuclei. [91, 106]

ROS are generated in the endoplasmic reticulum, in the peroxisomes, during mitochondrial oxidative metabolism, in the cellular response to xenobiotics, cytokines, and bacterial invasion. They are chemically reactive particles that contain oxygen, including hydrogen peroxide (H_2O_2), reactive superoxide anion radicals (O^{2-}), and hydroxyl radicals (•OH) [106]. ROS change (increasing or decreasing) leads to oxidative stress, which promotes the damage of nucleic acids, proteins, and lipids. This may explain their role in regulating cellular signalling pathways, cell proliferation and survival. In addition, ROS participates in carcinogenesis, neurodegeneration, atherosclerosis, diabetes, tumour metastasis. [106–108]

The choice of SPION and their dose plays a critical role in cell metabolism and in the occurrence of pathologies and diseases. Therefore, fundamental *in vitro* research is very important for the further use of nanoparticles in the field of regeneration and therapy.

2.3 MESENCHYMAL STEM CELLS AND THEIR MECHANISMS OF MIGRATION

German pathologist Cohnheim in his study has found that in the process of wound repair such inflammatory cells as fibroblast-like morphology cells that associated with thin fibrils take part. On this basis he suggested the possibility that bone marrow may be the source of fibroblasts that produce collagen fibres as part of the normal process of wound repair. Since 1867 he published studies about the source of fibroblasts in the process of wound repair. [109]

Later Friedenstein et al. managed to isolate fibroblast-like adherent cells from bone marrow [110, 111]. Friedenstein's studies about cells presence in bone marrow that can differentiate into fibroblasts, osteoblasts, chondrocytes and adipocytes have been available since 1976 [111, 112]. Currently, cells isolated from bone marrow with Friedenstein's method referred to mesenchymal stem cells (MSCs) [113] or marrow stromal cells [114]. In 2005 Mesenchymal and Tissue Stem Cell Committee recommended a clarification of the nomenclature for these important cells [115]. In 2006 International Society for Cellular Therapy (ISCT) stated that 'multipotent mesenchymal stromal cells' (MSCs) was the currently recommended designation and proposed three criteria to define MSCs: (i) MSCs must be plastic-adherent (tissue culture flasks) in standard culture conditions, (ii) MSCs must express specific surface antigens as CD105, CD73 and CD90 (≥ 95% positive), and must not express CD45, CD34, CD14 or CD11b, CD79α or CD19 and HL-DR (≤ 2% positive), (iii) the cells must be able to differentiate to osteoblasts, adipocytes and chondroblasts under standard *in vitro* differentiating conditions [116]. However, further studies have been shown, that these criteria do not completely characterize MSCs. Based on morphology, cell surface markers, differentiation potential, it can be difficult to distinguish fibroblasts and MSCs [117]. Currently, it was described in many studies that MSCs have the capacity to differentiate into chondrocytes, hepatocytes, myoblasts, epithelial cells, cardiomyocyte-like cells, neuron-like cells and others [2, 4].

At the beginning the characteristics of MSCs isolated from mouse bone marrow were described [111, 112]. Then the adult human bone marrow MSCs became available for research [118]. In addition, with increasing biologic and clinical interest in MSC, some other resources were identified. In recent studies more often use MSC that have been isolated from bone marrow, adipose tissue, amniotic tissue, chorionic tissue, umbilical cord and other foetal or adult tissues. A detailed comparison of MSC isolated from different tissues shows that they are not equal. Differences were found between expression of genes and surface markers and multipotent differentiation potential. [119–121]

Cell viability is strongly depends on the composition of the environment compartment: structure of extracellular matrix (ECM), presence of ions, growth factors, etc. The presence and contact with other nearby and distant cells are also important. Cell-to-cell communication regulates processes such as cell division, tissue growth, cell differentiation, tissue regeneration and other important processes. One of the types of cell communication based on molecular interchanges. The immunomodulatory action of MSCs is based on this property. Generally, tissue damage accompanied with inflammation and appearance of necrotic cells. This process is accompanied by the expression of pro-inflammatory mediators, such as interferon-γ (IFN-γ), tumour necrosis factor-α (TNF-α), interleukin-1 β (IL-1β), various chemokines, leukotrienes, and free radicals [21]. These mediators are the signal for MSCs to migrate towards the agglomeration of necrotic cells and express immunomodulatory factors, growth factors and surface molecules. The most common immunomodulatory factors are prostaglandin E2 (PGE-2), indoleamine 2,3-dioxygenase (IDO), nitric oxide (NO), TNF-inducible gene 6 protein. The growth factors, which MSC producing, are transforming growth factor-β (TGF-β), hepatocyte growth factor (HGF), epidermal growth factor, fibroblast growth factor (FGF), vascular endothelial growth factor, platelet-derived growth factor (PDGF), vascular endothelial growth factor (VEGF), insulin-like growth factor 1 (IGF-1), stromal cell-derived factor 1 (SDF-1), and angiopoietin-1. Surface molecules, such as galectins, intracellular adhesion molecule 1 (ICAM-1), and vascular cell adhesion molecule 1 (VCAM-1) also have an important role in the regeneration process. [122]

The ability of MSCs to migrate towards necrotic cells is an important function in the regeneration process. This process includes transendothelial cell migration and cell migration through the ECM. Chemokines from damaged tissue have a chemotactic effect on MSCs. Chemokines or mediators, such as SDF-1, IL-1β and TNF-α, give a signal to endothelial cells of blood vessels to activate VCAM-1 adhesion molecules and to express ICAM-1 intercellular adhesion molecules. MSCs begin to roll over the surface of endothelial cells and express adhesion molecules and integrins include CD44 and a very late antigen-4 (VLA-4). VLA-4 binds to VCAM-1 that allows to hold MSCs on the endothelial surface and promotes to adhere (Figure 7). MSCs also binds to the endothelial surface through the interaction with P-selectin, basic fibroblast growth factor (bFGF), and other growth factors and different integrins. Then, MSCs migrate through the endothelium. After that, they migrate through ECM toward damaged tissue. Also, MSCs in ECM can actively express matrix metalloproteinase 2 (MMP-2), which are involved in cell migration in ECM. [122–124]

The studies show that different types of MSCs can express different amount of growth factors, cytokines, and adhesion molecules. Therefore, their role and success in the participating of regeneration may be different. For example, adipose-derived MSCs secreted higher levels of VEGF and HGF regenerative factors than bone marrow MSCs [3]. HGF as antifibrotic factor plays an important role in angiogenesis and damage tissue repair [125, 126] Therefore, adipose-derived MSC may be more suitable source for brain tissue regeneration [3] and for repair of the heart postinfarction [127]. In the study [128], has been shown that IGF-1, VEGF-D, and interleukin-8 (IL-8) to be expressed at higher levels in adipose-derived MSCs compared with bone marrow MSCs and MSCs derived from dermal tissue. However, the expression of SDF-1 and NGF is higher in bone marrow MSCs. VEGF-D stimulate angiogenesis, and SDF-1 enhances tissue repair. SDF-1 factor supports viability of cells and attract the MSCs to the damaged area, such as infarcted zone, that is promote tissue regeneration [129]. SDF-1 and other chemokines contribute to the launch of several processes such as the activation of adhesive molecules that are involved in cell migration.

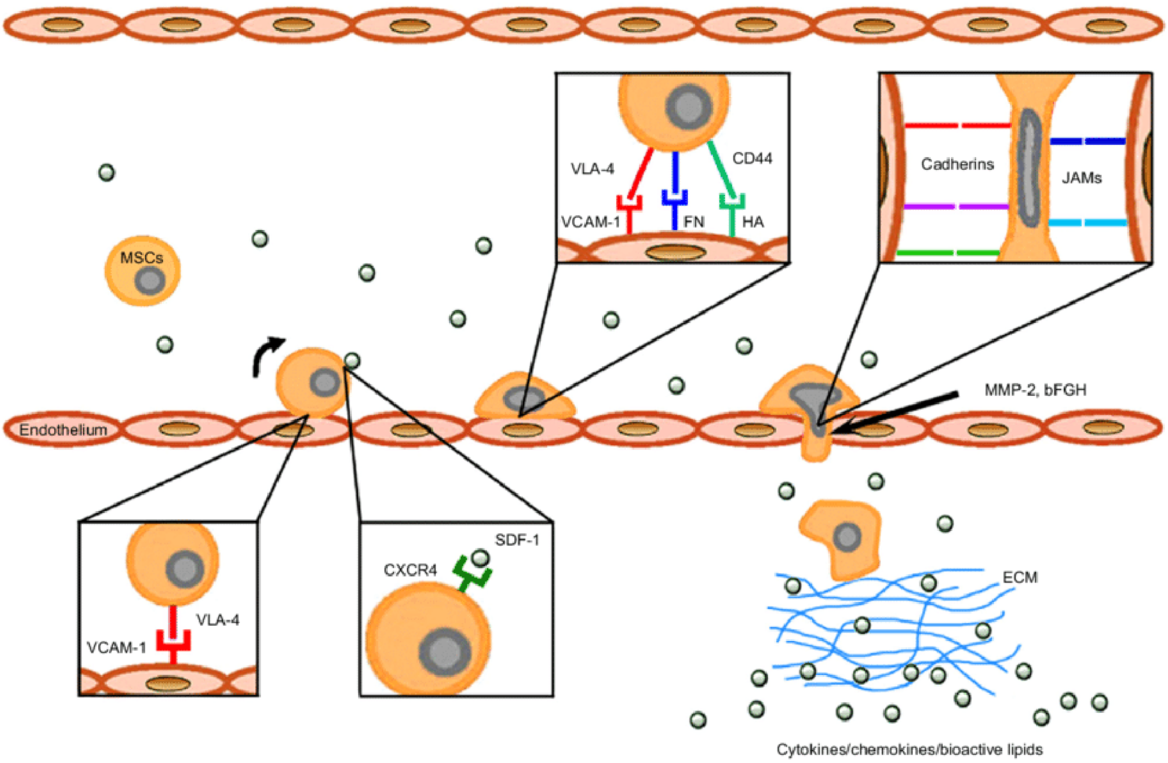

Figure 7. Mechanisms of MSC homing toward damaged tissue. Used abbreviations: Mesenchymal stem cells (MSC), very late antigen-4 (VLA-4), vascular cell adhesion molecule 1 (VCAM-1), fibronectin (FN), hyaluronic acid (HA), junction adhesion molecules (JAMs), matrix metalloproteinase 2 (MMP-2), basic fibroblast growth factor (bFGF), stromal cell-derived factor 1 (SDF-1), extracellular matrix (ECM) [122].

2.4 ADHERENT CELL MIGRATION

Cells can adapt and change their shape to move through tissues or ECM, divide and respond to extracellular conditions. The process of changing the shape occurs due to a change in the structure of the cytoskeleton. Tubulin, actin, and proteins forming intermediate filament are the major types of proteins that forms the cytoskeleton. [130]

Usually, adherent cells are constantly moving. They usually move randomly, but when responding to different signals, they can move directionally. At the beginning of moving the cytoskeletal networks polarize in the direction of migration. The actin cytoskeleton starts to form protrusions as lamellipodia and filopodia (Figure 8). The front part expands due to the formation of lamellipodia, formed by the polymerization of actin in this part. Filopodia is formed by parallel actin bundles. They are mainly taking part in migration through ECM and initiate cell-cell contacts. The new adhesions are formed in the front part and matured into actomyosin-linked focal adhesions. Then cell body contracts due to the contraction of stress fibres. The mature focal adhesions are disconnected then the back part of the cell is detached. Thus, the cell body moves in the desired direction. [130, 131]

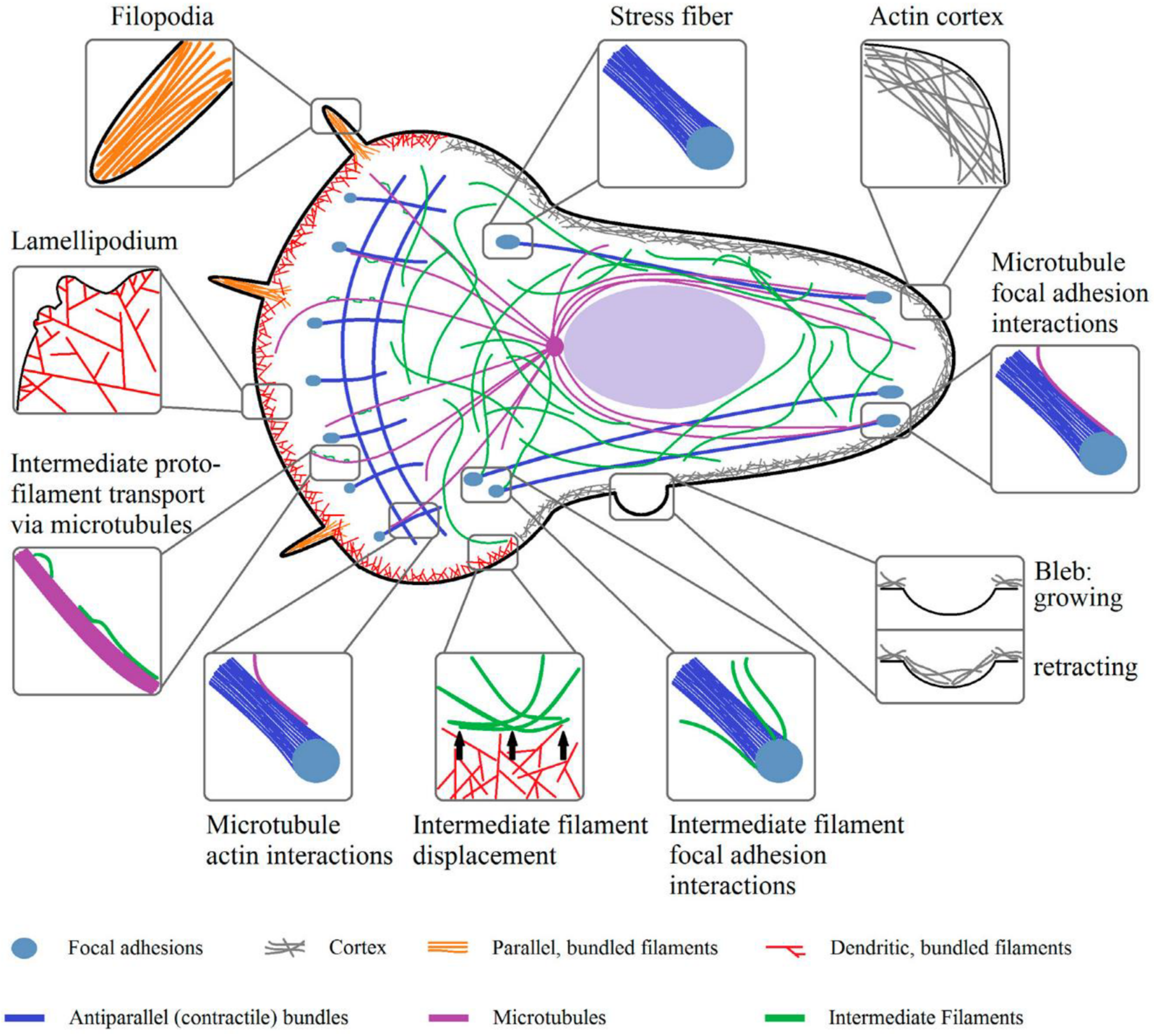

Figure 8. Organizational structures of actin, microtubules, and intermediate filaments inside of a cell and their physical interactions. [130]

Migration speed of cells is depends on external conditions, their type and ability to react on the present signal. Usually, single-cell migration can be observed during several hours or days. The microscopic images are obtained from several time point during selected time. Then obtained image sequence is analysed using available software. Usually, the position of cells is marked on each image from obtained sequence. Then different parameters can be calculated. The main parameters for quantitative analysis of cell migration are Accumulated distance and Euclidean distances (Figure 9). Also, the centre of mass and directionality can be determined to assess coordinated cell migration.

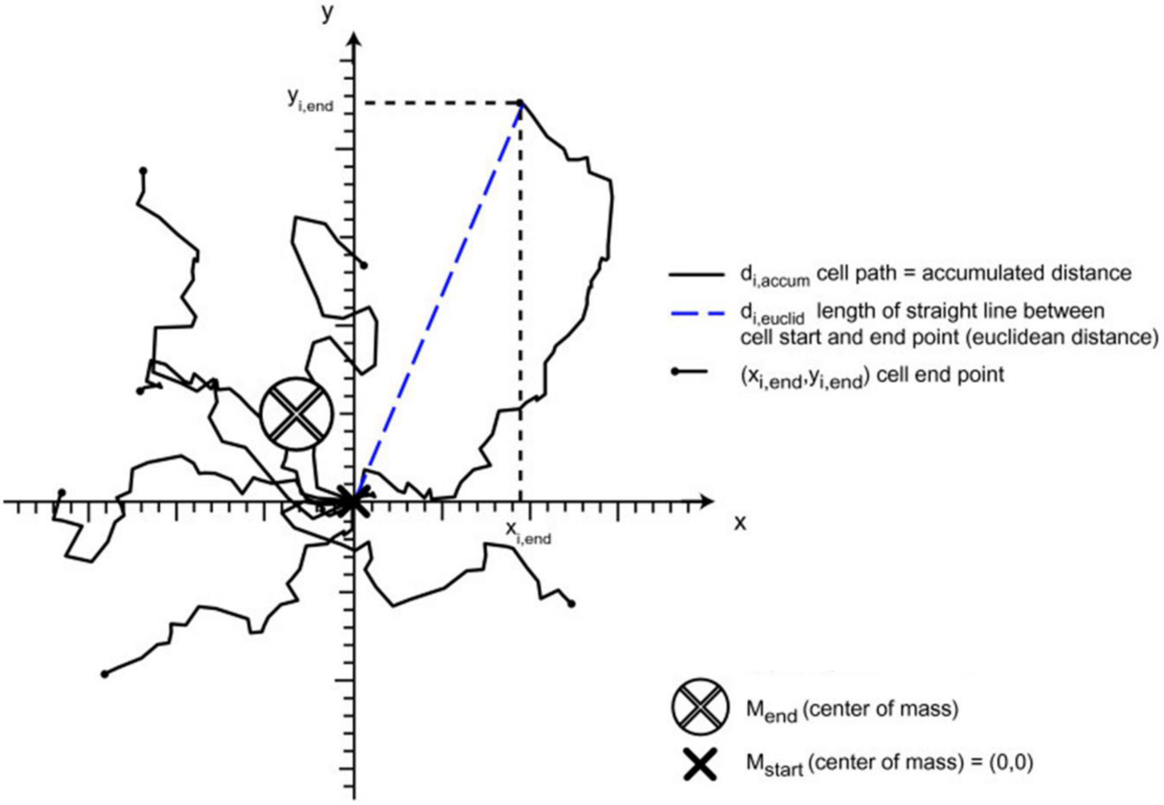

Figure 9. Trajectory plot defining different parameters for analysing cell migration *in vitro* in 2D. All cell trajectories are transformed by setting each starting point to $(x_{i,start}, y_{i,start}) = (0,0)$ at time $t = 0.1 \leq i \leq n$ index of the cells. [132]

The total distance d_{accum} (Accumulated distance) of migrated cell is calculated as:

$$d_{accum} = \sum_{i=1}^{n-1} \sqrt{(x_i - x_{i+1})^2 + (y_i - y_{i+1})^2} \tag{1}$$

Where x_i and y_i are the coordinates of the cell in the *i*-th image, x_{i+1} and y_{i+1} denote the coordinates of the same cell in the (*i*+1)-th image, *n* denotes the total number of images in the sequence.

The Euclidean distance d_{euclid} (from the start to the end position) is calculated as:

$$d_{euclid} = \sum_{i=1}^{n-1} \sqrt{(x_{end} - x_{ini})^2 + (y_{end} - y_{ini})^2} \tag{2}$$

Where x_{ini} and y_{ini} are the coordinates of the cell in the first image (start), x_{end} and y_{end} are the coordinates of the same cell in the last image of image sequence, *n* denotes the total number of images in the sequence.

There are various methods of cell migration study. The scratch assay (or wound healing) is widespread method for collective cell migration study [133]. Usually, control samples without treatment are compared with the tested treatment samples. Thus, cells are seeded at least on two culture dishes (or wells). When cells are reached 100% confluency, then a gap across cell layer is created using pipette tip. After that, cells tend to close the created gap and start to migrate into the gap area. Applied treatment may affect the physiological functions of cells. Using scratch assay test the velocity of gap closure of control and treatment samples is compared. Thus, the effect of applied treatment can be assessed. Usually, the microscopic images from observed samples described in different time points (Figure 10). Then the evaluation of the result can be performed manually or using image processing algorithms [134–136].

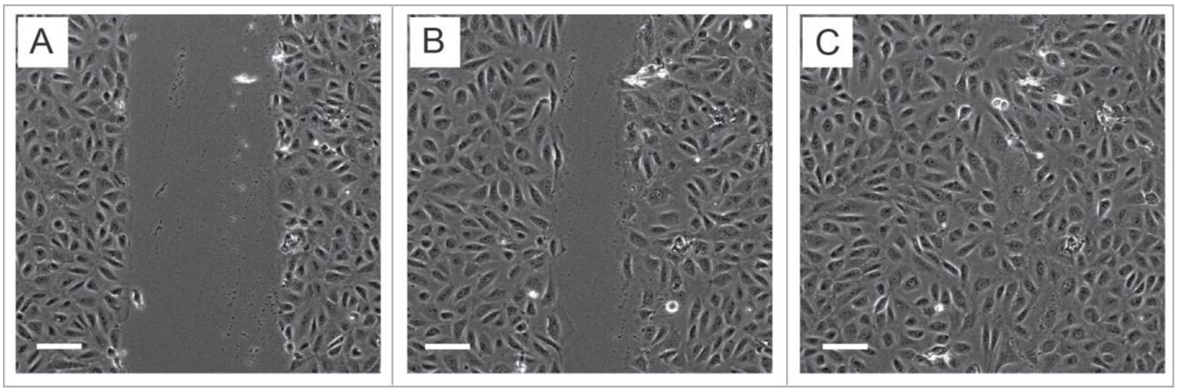

Figure 10. Images from a *scratch assay* experiment at different time points. Human umbilical vein endothelial cells (HUVEC) images obtained by phase contrast microscopy (PCM). Scale bar 120 µm. [133]

This method is applicable for study of two culture lines in co-culture. For this it is necessary to create a temporary border on the culture dish to allow to culture two cell lines separately in the same dish. The temporary border can be created using inserts, which can be removed when the cells reached desired confluency (see Figure 32, Figure 37).

3 AIMS OF THE DOCTORAL THESIS

The main research aim of this dissertation is to assess the properties of fluorescent methods in biological research. This work is focused on the methods and properties of specific cell cultures in *in vitro* studies in the field of regenerative medicine. The modern technologies of tissue engineering in regenerative medicine are based on biocompatible scaffolds. Therefore, there are requirements in 3D imaging and detection of living cells in different types of scaffolds. The appropriate microscopic techniques and fluorescent markers are needed in the basal *in vitro* studies. Furthermore, the applied fluorescent markers should possess biocompatible and non-toxic properties for their effective and safe use in biological research.

The main objectives of this work can be formulated as follows:

1. To review a mechanism of mesenchymal stem cell (MSC) migration and to identify and provide optimal conditions and protocols for the culture of living cells.
2. To study the limitations and advantages of fluorescent widefield and confocal microscopy in long-term cell observation; to select fluorescent probes appropriate for cell detection and useful for long-term monitoring of marked cells; and to show the benefits of fluorescent markers used in cell detection or quantitative analysis of cell migration studies.
3. To study the properties of rhodamine-derived superparamagnetic maghemite nanoparticles (SAMN-R) to determine their size, interaction with living cells, and excitation and emission spectra; to study the possible toxic effect of SAMN-R on living cells; and to identify an effective concentration of SAMN-R for living cells labelling.
4. To study the effect of SAMN-R-based fluorescence labels on cell motility; to apply the appropriate methods for cell migration study using fluorescent microscopy techniques; and to design experimental protocols.
5. To review the possibilities of *in vitro* studies in the field of cardiac tissue regeneration and to design and apply an experimental model to study interactions between MSCs and cardiac cells in co-culture.

Task 1 is considered in Chapters 2.3 and 2.4, where the properties of MSCs and mechanism of adherent cell migration are reviewed. The cell culture protocols are described in Chapter 4.1. To solve task 2, the principle of fluorescence microscopy is reviewed in Chapter 2.1. The necessary conditions and limitations of long-term experiments are described in Chapter 4.2. Then fluorescent dyes are selected based on their properties (Chapter 5). To implement the solution of task 3, the properties of SPION are reviewed (Chapter 2.2). The previous studies about SAMN-R are reviewed and their properties are studied using fluorescence microscopy (Chapter 5.1). The solution of task 3 also includes the study of possible toxic effect of SAMN-R on living cells, which is presented in Chapter 6. The solution of task 4 is presented by performing experiments on the study of collective and single-cell migration (Chapters 7.1 and 7.2). To solve task 5, a review about using MSCs and cardiac cells in co-culture is carried out in Chapter 8, which also contains the experimental model for the study of cell communication.

4 CELL CULTURES AND EXPERIMENTAL PROTOCOLS

Currently, bone marrow and adipose tissue MSCs are commonly used in tissue engineering and regenerative medicine research. Bone marrow and adipose tissue are the largest resources of MSCs. Isolation of these cells takes place with less risk to the patient, that is very important factor. In the initial studies, the use of bone marrow MSCs was popular. Currently, the adipose tissue removed during a liposuction procedure is available for many researchers. Usually, adipose tissue is a liposuction waste product, thus there is no need to subject patients to a special operation to isolate cells. However, MSCs from different tissues have a different ability to differentiate into a variety type of cells. Therefore, the choice of cell type depends on the applications.

MSCs isolated from different tissues express the different amount of growth and regenerative factors. Therefore, the success of their participation in tissue regeneration is different. In this work the area of cardiac tissue regeneration was of interest. This process is based on the ability of MSCs to migrate towards necrotic cells, which are the outcome of MI [21–23]. Also, MSCs have a great potential in cardiac tissue regeneration, due to their paracrine and immunomodulatory properties [3]. Some studies show that adipose-derived MSCs may have more success in this area than bone marrow MSCs [2, 26]. The use of adipose tissue derived MSCs is becoming popular due to their excellent properties, availability, and lower risk to donors during cell isolation. For these reasons adipose tissue derived MSCs were chosen for studies in this work.

Human MSCs isolated from adipose tissue (hMSCs) via protocol [137] were used. Adipose tissue was obtained from eight healthy patients (male, age 40–50, weight 80–110 kg) undergoing abdominal liposuction (collected waste tissue) after gaining a signature of written informed consent in accordance with Czech law 372/2011 and the Declaration of Helsinki. Adipose tissue was washed with phosphate-buffered saline (PBS), mechanical minced, enzymatic digested using collagenase type-1 (treated for 1 hour) and hMSCs were separated after centrifuge. Isolated cells were seeded on the polystyrene surface of the 24-well plate or T25 flack. It is recommended to use aspiration to remove the growth medium and PBS. Then the cells were cultured under standard incubation conditions. Isolation cells had well adherence property on polystyrene non-coated surface. Good adhesion on a plastic surface is one of the characteristics of MSCs [116]. For this work, cells of the second passage were obtained, and then, in the experiments the cells of the passages 3–6 were used. Cells were subcultured according to the protocol, which is given in chapter 4.1.1.

Cell morphology was controlled using light, IMC or PCM microscopy. MSCs are divided into three morphological subpopulations: rapidly self-renewing cells; elongated, fibroblastic-like, spindle-shaped cells and slowly replicating, large, cuboidal or flattened cells [138, 139]. This cell types are marked in Figure 11.

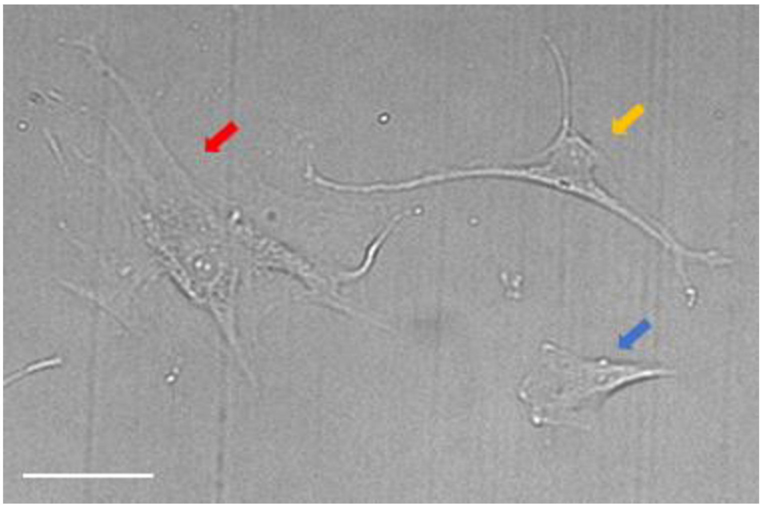

Figure 11. Human adipose-derived mesenchymal stem cells (hMSCs) demonstrated three morphological subpopulations: rapidly self-renewing cells; elongated, fibroblastic-like, spindle-shaped cells and slowly replicating, large, cuboidal or flattened cells. They are marked with blue, yellow and red arrow respectively. Bright-field microscopy, 10× magnification, scale bar 100 µm.

For defining MSCs expression of surface markers [116, 140] was analysed. This analysis was performed on flow-cytometer Cytomics FC500 (Beckman-Coulter Inc., IN, USA) with positive CD73, CD90 (≥95%) and negative CD45 (≤2%) antibodies (Miltenyi Biotec, Germany) [141]. The results from flow-cytometry are not shown. Multipotent differentiation potential, which is one of the criteria to define MSCs, was not studied.

Fibroblast cell line 3T3 (Sigma-Aldrich s.r.o., 93061524) was used in the part of experiments. Unfortunately, hMSCs were not always available, so it was necessary to choose a similar cell line. Fibroblast strains have morphology similar to MSCs. It was show in studies [117, 142], that they comply with the minimum criteria for defining multipotent mesenchymal stromal cells [116]. Also, they are less demanding in culture *in vitro* as MSCs. Therefore, 3T3 fibroblast cell line (Figure 12) was chosen for comparative characterization with MSCs and for replacement in some types of experiments. Cells were subcultured according to the protocol, which is given chapter 4.1.2.

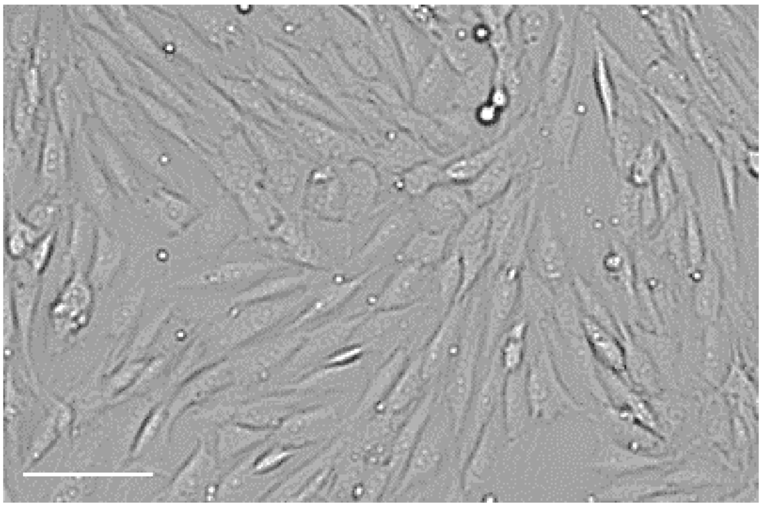

Figure 12. NIH 3T3 cells. Bright-field microscopy, 10× magnification, scale bar 100 µm.

HL-1 cardiac muscle cell line (Sigma-Aldrich s.r.o., SCC065) was used as a cardiac tissue model. This cell line was chosen due to morphological, electrophysiological and gene expression characteristics. HL-1 is the cardiac muscle cell line, derived from the AT-1 mouse atrial cardiomyocyte tumour lineage [143]. It was defined that they express similar genes as the adult atrial cardiomyocytes. Also, confluent cell line has an ability to contract [143, 144]. It was defined that confluent cultures (Figure 13) exhibited synchronous beating [143]. Electroactivity of 90% of confluent culture was confirmed by using microelectrode arrays system (MEA2100-System, Multi Channel Systems MCS GmbH) in [145]. HL-1 cells maintain electrophysiological properties also after several passages. Furthermore, their morphological characteristics are very similar to cardiomyocytes. Their properties confirm the possibility of their successful use in the MSCs and cardiac tissue communication study. Cells were subcultured according to the protocol, which is given in chapter 4.1.3. Cells of the passage 3–6 were used in the experiments.

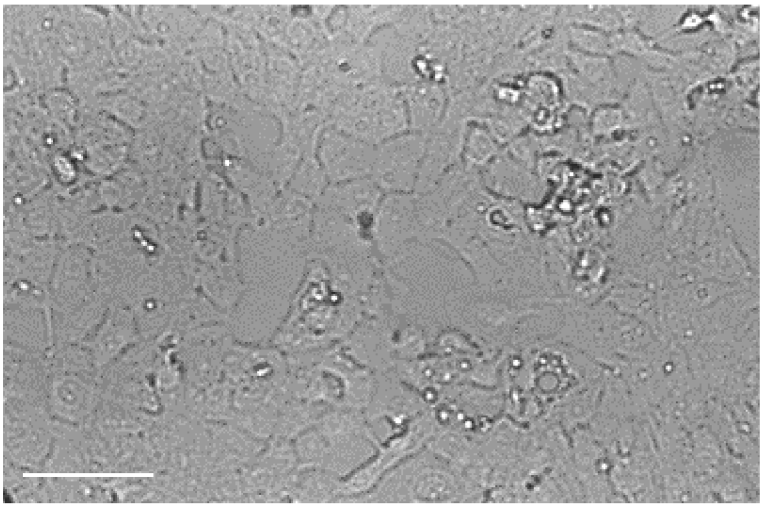

Figure 13. HL-1 cardiac muscle cell line. Bright-field microscopy, 10× magnification, scale bar 100 µm.

4.1 CELL SUBCULTURING PROTOCOLS

The cells were cultured in clean room in biosafety conditions [146]. Cells were incubated at 37°C in a humidified atmosphere containing 5% CO_2. Procedure of subculturing and feed of cells were performed in laminar-flow hood following protocols. The work surface was cleaned with 70% ethanol before and after work. The outside of containers, flasks, plates, dishes, pipettes boxes, pipettors and other used items were disinfected with 70% ethanol before placing them in the laminar-flow hood. Also work surface were sterilized after work with ultraviolet light. Media, reagents, and chemicals were stored according to manufacturer's instructions. Cell culture flasks (T25, Sigma-Aldrich s.r.o.), Petri dishes (TPP Techno Plastic Products AG, BIO-PORT Europe s.r.o.), multi-well plates (Sigma-Aldrich s.r.o.), and 8-well chambered cover glasses (Celvis) were used for cell culture. The laboratory (Department of Biomedical Engineering, Faculty of Electrical Engineering and Communication, Brno University of Technology) was equipped with a standard equipment: Laminar-flow hood (Alpina BIO 100), Humidified CO_2 incubator (MEMMERT INCOmed), Refrigerator (LIEBHERR Thermostatic cabinet), Freezer

(–20°C and –80°C, Hyundai, National lab), Water bath (Julabo ED), Centrifuge (Hettich EBA 20, Biosan LMC-3000), Pipettes (PZ HTL S.A.), Macroman (Eppendorf, Gilson), Aspiration pump (FTA-1, Biosan), Cell counter (LUNA-II, Logos Biosystems, Inc.), pH meter (S2K712, ISFETCOM), Vortex mixer (MS 3 basic, IKA), Inverted light, phase contrast and fluorescence microscope (ZEISS Axio Observer 5), Autoclave (Nova-3, Tuttnauer), Ultrasonic homogenisers (SONOPULS HD 3200, Bandelin electronic).

4.1.1 PROTOCOL OF SUBCULTURING OF HUMAN ADIPOSE-DERIVED MESENCHYMAL STEM CELLS

Phosphate buffered saline (Sigma-Aldrich s.r.o., P4417-100TAB), Accutase (PAA Laboratories GmbH, L11-007), low glucose Dulbecco's Modified Eagle Medium (DMEM; Sigma-Aldrich s.r.o., D6046), foetal bovine serum (FBS; Sigma-Aldrich s.r.o., F0804), Penicillin-streptomycin (Sigma-Aldrich s.r.o., P4333) were used for cell culturing.

Complete low glucose DMEM contains (100 mL): 94 ml of low glucose DMEM, 5 mL of FBS, 1 mL of Penicillin-streptomycin ($100\ \mathrm{U{\cdot}mL^{-1}}$:$100\ \mu\mathrm{g{\cdot}mL^{-1}}$). Supplemented medium was stored at 5.2°C. Medium was changed two or three times in a week. Cells were subcultured when they reached a confluency of 80–100%. Cells were subcultured according to the protocol based on [147], which is given below:

1. Warm any reagents to 37°C,
2. Remove the medium from well of 24-well plate by aspiration,
3. Wash the monolayer of cells with 500 mL of PBS and remove the solution by aspiration,
4. Pipette 300 μL of Accutase into the well of 24-well plate. Move 24-well plate to incubator (37°C, 5% CO_2) for about three minutes,
5. After three minutes, control the cells under an inverted microscope. It is recommended to use a PCM. If the cells are not detached, then remove the Accutase from the well and wash the cells twice. If it is necessary, hold the Accutase within additional time (15 minutes maximum),
6. Pipette 900 μL of complete low glucose DMEM to the well to inhibit further tryptic activity,
7. Resuspend the cell suspension and transfer an equal volume to a two 1.5 mL sterile microtube,
8. Centrifuge the microtubes at 1000 rpm for 5 minutes to pellet the cells,
9. Meanwhile, prepare 24-well plate for cell seeding: add 800 μL of low glucose DMEM to well or several wells, if it necessary,
10. After centrifugation, aspirate the supernatant from the microtubes without disturbing the cell pellet,
11. Resuspend the cells in 200 μL of complete low glucose DMEM, by gently pipetting the cells,
12. Count the cells with a cell counter,

13. Place the necessary number of cells into the new wells of 24-well plate (generally 30% by cell suspension) and use required number of cells for the experiments,
14. Incubate at 37°C, 5% CO_2 atmosphere.

4.1.2 PROTOCOL OF SUBCULTURING OF NIH 3T3 CELL LINE

PBS (Sigma-Aldrich s.r.o., 79382), 0.25% Trypsin-EDTA solution (Sigma-Aldrich s.r.o., T4049), high glucose DMEM (Sigma-Aldrich s.r.o., D6429), FBS (Sigma-Aldrich s.r.o., F0804), Penicillin-streptomycin (Sigma-Aldrich s.r.o., P4333) were used for cell culturing.

Complete high glucose DMEM contains (100 mL): 89 mL of high glucose DMEM, 10 mL of FBS, 1 mL of Penicillin-streptomycin (100 $U \cdot mL^{-1}$:100 $\mu g \cdot mL^{-1}$). Supplemented medium was stored at 5.2°C. Medium was changed two or three times in a week. Cells were subcultured when they reached a confluency of 80–100%. Cells of the passage 10–25 were used in the experiments.

Cells were subcultured according to the protocol based on [148], which is given below:

1. Warm any reagents to 37°C,
2. Remove the medium from T25 culture flask by aspiration,
3. Wash the monolayer of cells with 3 mL of PBS and remove the solution by aspiration,
4. Pipette 1 mL of 0.25% Trypsin-EDTA solution into the T25 flask. Make sure that solution covers all the cells. Move T25 flask to incubator (37°C, 5% CO_2) for about three minutes,
5. After three minutes, do control the T25 flask under an inverted microscope. Release the rounded cells from the culture surface by hitting the side of the flask against your palm until most of the cells are detached,
6. Pipette 3 mL of complete high glucose DMEM to the flask to inhibit further tryptic activity,
7. Resuspend the cell suspension and transfer to a 15 mL sterile conical centrifuge tube,
8. Centrifuge the conical tube at 1000 rpm for five minutes to pellet the cells,
9. Meanwhile, add 5 mL of high glucose DMEM to sterile T25 flask,
10. After centrifugation, aspirate the supernatant from the tube without disturbing the cell pellet,
11. Resuspend the cells in 1 mL of complete high glucose DMEM, by gently pipetting the cells,
12. Count the cells with a cell counter,
13. Place the necessary number of cells (generally 20% by cell suspension) into T25 flask filled with 5 mL of the complete high glucose DMEM and use required number of cells by the experiments,
14. Incubate at 37°C, 5% CO_2 atmosphere.

4.1.3 PROTOCOL OF SUBCULTURING OF HL-1 CARDIAC MUSCLE CELL LINE

Calcium and magnesium free PBS (Sigma-Aldrich s.r.o., D8537), 0.05% Trypsin-EDTA solution (Sigma-Aldrich s.r.o., T3924), soybean trypsin inhibitor (Sigma-Aldrich s.r.o., T6522), Claycomb medium (Sigma-Aldrich s.r.o., 51800C), FBS (Sigma-Aldrich s.r.o., TMS-016), Penicillin-Streptomycin (Sigma-Aldrich s.r.o., P4333), L-Glutamine (Sigma-Aldrich s.r.o., G7513), Norepinephrine (Sigma-Aldrich s.r.o., A0937), L-Ascorbic acid (Sigma-Aldrich s.r.o., A7506), Distilled water (Sigma-Aldrich s.r.o., W3500), Fibronectin (Sigma-Aldrich s.r.o., F1141), Gelatine from bovine skin (Sigma-Aldrich s.r.o., G9391) were used for cell culturing.

Complete Claycomb medium is contains (100 mL): 87 mL of Claycomb medium, 10 mL of FBS, 1 mL of Penicillin-Streptomycin ($100\ \mathrm{U{\cdot}mL^{-1}}:100\ \mathrm{\mu g{\cdot}mL^{-1}}$), Norepinephrine (0.1 mM), L-Glutamine (2 mM). Supplemented Claycomb Medium were mixed every two weeks and were store at 5.2°C protected from light. Medium was changed three times of a week. Cells were subcultured when they reached a confluency of 80–100%. Cells of the passage 3–6 were used in the experiments.

Cells were subcultured according to the protocol based on [149], which is given below:

1. About 30 minutes before culturing cells, prepare gelatine/fibronectin solution: dilute 1 mL of fibronectin ($1\ \mathrm{mg{\cdot}mL^{-1}}$) in 199 mL of 0.02% gelatine from bovine skin,

2. Coat a culture T25 flask with 2 mL of gelatine/fibronectin solution. Make sure that solution covers entire surface. Move T25 flask to incubator (37°C, 5% CO_2) about 40–60 minutes,

3. Warm any reagents to 37°C,
4. Remove the medium from culture flasks by aspiration,
5. Rinse gently the monolayer of cells with PBS and remove the solution by aspiration,
6. Pipette 1 mL of 0.05% Trypsin-EDTA solution into the T25 flask. Make sure that solution covers all the cells. Incubate at room temperature for one minute. Then remove and add 1 mL of fresh 0.05% trypsin-EDTA. Incubate at room temperature for two minutes,
7. After that, do control the T25 flask under an inverted microscope. If the cells are still adhered, rap the flask on the benchtop or hitting the side of the flask against your palm,
8. When the cells are detached, pipette 1 mL of soybean trypsin inhibitor to the flask,
9. Resuspend the cell suspension and transfer to the two 15 mL sterile conical centrifuge tube (evenly 1 mL to each tube). Then add 2 mL of complete Claycomb medium to each tube and resuspend the cell suspension again,
10. Centrifuge the conical tubes at 600 rpm for five minutes to pellet the cells,
11. Meanwhile, remove the gelatine/fibronectin solution from T25 flask, and add 8 mL of complete Claycomb Medium,

12. Arter centrifugation, aspirate the supernatant from the tubes without disturbing the cell pellet,
13. Resuspend the cells in 1 mL of complete Claycomb medium, by gently pipetting the cells,
14. Count the cells with a cell counter,
15. Place the necessary number of cells (generally 30% by cell suspension) into gelatine/fibronectin coated T25 flask filled with 8 mL of the complete Claycomb medium, and use required number of cells by the experiments,
16. Incubate at 37°C, 5% CO_2 atmosphere.

4.2 PREPARING FOR LONG TERM LIVE-CELL IMAGING USING CONFOCAL MICROSCOPY

Planning is the foundation of the experiment. It includes such fundamental points as setting goals, preparation of the necessary equipment including a microscope, study of the hardware and software capabilities of the equipment used, providing incubation conditions, choosing cells, culture media, culture vessels, fluorophores or fluorescent markers.

Generally, an inverted microscope is used for cell imaging applications. In the design of an inverted microscope, the objectives are located under the stage. When focusing, the objective approaches the bottom of the culture dish or other culture vessel from the outside. This allows to minimize the distance between the front lens and the observed specimen. Therefore, it is possible to use objectives with a short working distance, which is defined by the distance between the front lens element and the surface of the culture vessel bottom, when the specimen is in sharp focus. This distance depends on magnification and numerical aperture (NA) of objective, which are marked on the objective. Light waves pass through the specimen, and they are refracted, diffracted, or reflected on the specimen's structure. The objective lens collects these waves and creates an intermediate image. The resolving power of the objective is determined by NA, which determines the amount of light collected. Higher NA means that the objective can collect more light at a wider angle and therefore gives higher resolution. Thus, it is an important parameter of an objective lens that affects the resolution and brightness of images, as well as the intensity of images in the case of fluorescence microscopy. The NA is defined us:

$$NA = n \sin\theta \tag{3}$$

where n is the refractive index of the medium between the front lens of the objective and the specimen cover glass (air, water, glycerol, oil or other immersion media), and θ is half of the angle of the cone of light which can be collected by the front lens of the objective (angular aperture). [62, 150]

Usually, objectives with low magnification up to 40× do not touch the bottom of culture vessel when the specimen is in the focus plane. Thus, there is an air space between the objective lens and the bottom of the culture vessel, therefore these objectives are called "dry". The maximum value of the angle θ is 90° and the refraction index of air is ~1.00 (generally used n=1.00), therefore according to the formula 3 the numerical aperture of "dry" microscope objectives cannot exceed 1. To exceed this value and achieve high aperture values, it is necessary to achieve a high refractive index of the medium between the objective lens and the specimen. For this purpose, it is necessary that light passed through the medium with the equivalent refractive index value. Therefore, higher magnification objectives (from 60×) are usually designed for use with an immersion medium. In this case, the oil (n=1.51), glycerol (n=1.41) or water (n=1.33) are used as immersion medium for filling the space between the objective lens and the bottom of the specimen dish. The type of that media is determined by the characteristic of the objective. For imaging of fixed samples, for example in glycerol mounting medium (n=1.45) and covered with cover glass (n=1.52) it is better to use oil immersion objectives. In the case of visualization of live cells cultured on borosilicate glass (n=1.47) in cell culture medium (n=1.31-1.33), it is better to use the water immersion objectives. Nevertheless, the choice of objective magnification and numerical aperture depends on the purpose of the study. [151]

Usually, high magnification immersion objectives have a very short working distance (~60 μm) [62]. Front lens and the bottom of the culture vessel nearly touch each other when the specimen is in focus. This requires the use of confocal dishes and chamber slides with a thin glass (borosilicate) bottom. Usually their thickness range is 0.16–0.19 mm (#1.5H grade number). In addition, glass-bottom chambered coverslips are widely used in experiments when it is necessary to observe and compare different samples cultured under the same conditions. Also, the use of dishes and chambered slides with a thin glass bottom helps to minimize spherical aberration [62, 150].

Unfortunately, many types of cells have a poor ability to adhere on the glass surface. Different coatings are used to increase the adhesive strength. For example, ECM such as fibronectin and collagen can adsorb on the glass surface. They involve as attachment proteins that create bindings with transmembrane integrins [152]. Also, gelatine, collagen, PLL and Poly-d-lysine (PDL) are commonly used for promoting cell adhesion [152, 153]. In some types of experiments in this work, fibronectin and gelatine/fibronectin coating were chosen. The coating creates an additional layer between the glass and cells. Thus, the distance between the objective front lens and the cells in a focal plane increases. Therefore, it may be necessary to use dishes or chambered cover glass with a glass bottom of thickness 0.13–0.16 mm (#1H) or 0.083–0.13 mm (#0H). In this work objective with 10× magnification, 0.3 NA and 11 mm working distance (HC PL FLUOTAR10x/0.30 Dry) and oil immersion objective with 63× magnification, 1.4 NA and 140 μm working distance (HC PL APO CS2 63x/1.4 Oil) according to the specification were mainly used. For the immersion objective, the glass thickness of #1.5H was optimal, including the used coating.

Cells usually incubated at 37°C in a humidified atmosphere containing 5% CO_2. Cell growth medium condition is important for cell survival *in vitro*. Maintaining an atmospheric CO_2 of 5% in cell culture incubators is necessary for maintaining acidity level of growth medium on pH 7.4. This level also changes depending on the amount of metabolic products of the cells. Usually, cell growth medium includes phenol red for monitoring the pH level. By the colour range from yellow to red, the pH of solutions from acidic to alkaline can be visually controlled. It is recommended to use growth medium without phenol red, saline-based solutions or transparent buffers for live-cell imaging using fluorescence microscopy, because the less transparent liquids can contribute to background noise [154]. However, buffers and saline-based solutions do not include a major constituent of the growth cell media, which are necessary for cell growth, therefore they are not suitable for long-term experiments. Nevertheless, in this work the growth medium with phenol red was used. Since the confocal microscopy was mainly used, it was possible to compensate the noise level using the settings of microscope software.

For long-term observation of cells, the incubation conditions must be observed. Microscope incubators are available for this purpose. They usually include a temperature, gas, and humidity control. One of the types is a cage incubator with a large space around the microscope. This type has the advantage that the whole sample with cells is inside in constant conditions. The study sample can be of a nonspecific size or include several parts of equipment that can be located inside the incubator space. For example, fluidic systems, microelectrode array and other types of electrical stimulators, etc. The other type is a stage top incubator with a small chamber that installed on the stage of the microscope. The chamber constructed for culture dishes, slides, and multi-well plates. Typically, construction includes a transparent lid and a heated frame. In this case, the conditions in the vicinity of the sample in a small space are more accurately controlled. In this work, the stage top incubator was used (The Stage Top Chamber, OKOLAB).

After transferring the cells from the laboratory incubator to the microscope stage incubator, it is necessary to wait some time before setting up the experiment. During the installation of the sample on the heated microscope stage, the incubator is open, therefore, the set parameters of the oxide level and atmospheric humidity are disturbed for some time. During the movement, the culture dish with adherent cells and growth medium cools down by several degrees, therefore condensation may form on the dish lid. Condensation is an obstacle on the optical path when imaging a sample. The image will be blurry, and the Z plane will be selected incorrectly. For these reasons, the experiment settings were started 30 minutes after the sample was placed in the microscope incubator. Also, it is very important to fix the object well on the microscope stage. Unstable position of the sample on the stage may affect the displacement of it on the focus plane. Thus, the correct focusing or the X, Y positions can be negatively affected. The position of the microscope construction on the anti-vibration table helps to eliminate the influence of mechanical vibrations of the floor on the displacement of the specimen.

In planning long-term experiments not only the technical equipment of the microscope is important, but also the possibilities of software settings. Developments in software functions improve the conditions for long-term experimentation. The ability to acquire images from several fields of view one after another automatically and sequentially has expanded the possibilities for research. It can be a selected area consisting of adjacent fields of view (tile scan function, Las X software) or several fields of view located at a distance from each other (mark and find function, Las X software). The cells in various types of experiments can be seeded on uneven surfaces and different shapes, especially in the case of using 3D scaffolds. Therefore, it may be necessary to adjust the individual focus in each selected field of view. Modern versions of the microscope software have an option to select an individual focus in each field of view. In addition, because of cell motility, focus can change over time. To solve these problems, autofocus systems based on image processing techniques are being improved. In addition, Las X confocal microscope software includes the sequence scan function. With this option, it is possible to obtain the 3D image sequences from several selected fields of view. This option is especially important for creating long-term experiments. This function allows to configure acquiring of image sequences from one or several fields of view, including 3D, with a selected time interval and duration. In addition, when acquiring images from several fields of view, it is necessary to consider the error of microscope stage movement. For example, according to the specification, the reproducibility of the automatic stage movement of the used confocal microscope is equal to 1 μm. In the case of the fast phenomena study or when using a lens objective with high magnification, this can create unwanted errors.

The choice of image resolution, scanning speed, time interval between acquisitions, dimensions size, and the number of fields of view are interrelated. A compromise needs to be found considering important factors. In some cases, the quality of images is neglected in order to reduce the time interval or to increase the number of fields of view. When planning a long-term experiment, the phototoxicity effect must also be considered, because it negatively influences on live cells [155]. Fluorophores react with oxygen and degrade during the excited state. This process leads to the formation of excess ROS, that can cause phototoxicity [154]. It is necessary to reduce the number of images of one field of view, as much as possible. Also, it is important to adjust the excitation laser intensity to the lowest effective value. High intensity of the excitation can cause fluorophore degradation and subsequent loss of fluorescence (photobleaching effect). The number of images of one field of view is regulated by the choice of the z-stacks number (2D or 3D), time interval and duration of the experiment. In this work, in the long-term experiments the images were obtained with a resolution of 1024 × 1024 pixels with a 100 Hz scan speed (number of scanned lines per second). This parameter was set to the optimal considering subsequent image processing. The proposed time interval and duration was chosen according to the needs of the planned experiment and was confirmed experimentally.

If the sample was stained with several fluorophores, then it was possible to obtain images from several fluorescence emission channels using sequential image acquisition method. In this case the images from each channel were acquired separately in sequence one after another. Accordingly, the image acquisition time of one field of view is directly proportional to the number of channels. The using of sequence mode can help if the used confocal microscope is equipped with only one HyD detector. For simultaneous use, fluorophores should be selected with different wavelengths of excitation and emission maximum, and with the smallest overlap of its spectra. In some cases, this choice is very difficult. For example, when it is necessary to stain the cell nuclei, DAPI (4′,6-Diamidino-2-phenylindole dihydrochloride) or Hoechst 33342 (bisBenzimide H 33342 trihydrochloride) are often chosen. Both of them have almost identical spectra. The DAPI and Hoechst 33342 spectra have a wide stokes shift. Their emission spectrum overlaps with emission spectrum of fluorescein (FITC) and have an efficiency of about 50% at the maximum of emission FITC (Figure 14 (A)). Therefore, if DAPI (or Hoechst 33342) and FITC fluorophores excited at the same time, then the first fluorescence emission channel contains DAPI stained nuclei and the second channel contains DAPI stained nuclei and FITC stained organelles. This example is shown in Figure 14 (B). This effect can be avoided by exciting both fluorophores separately (Figure 14 (C, E)). Figure 14 (D) shows an example of settings for image acquisition from sample stained with three fluorophores [156]. The acquisition of images from the channels was performed one after another in a sequence. This method significantly improves the quality of images when using several fluorophores with overlapping spectra. Nevertheless, when fast moving cells or organelles are observed, this method may not be suitable.

In some cases, it is necessary to sacrifice the image quality by decreasing the resolution and increasing the scanning speed.

Therefore, when choosing fluorophores, it is necessary to consider the following factors: cell and organelle motility, spectral characteristics, number of fluorophores, whether the fluorophore is suitable for living cells, how long it is retained in the cells.

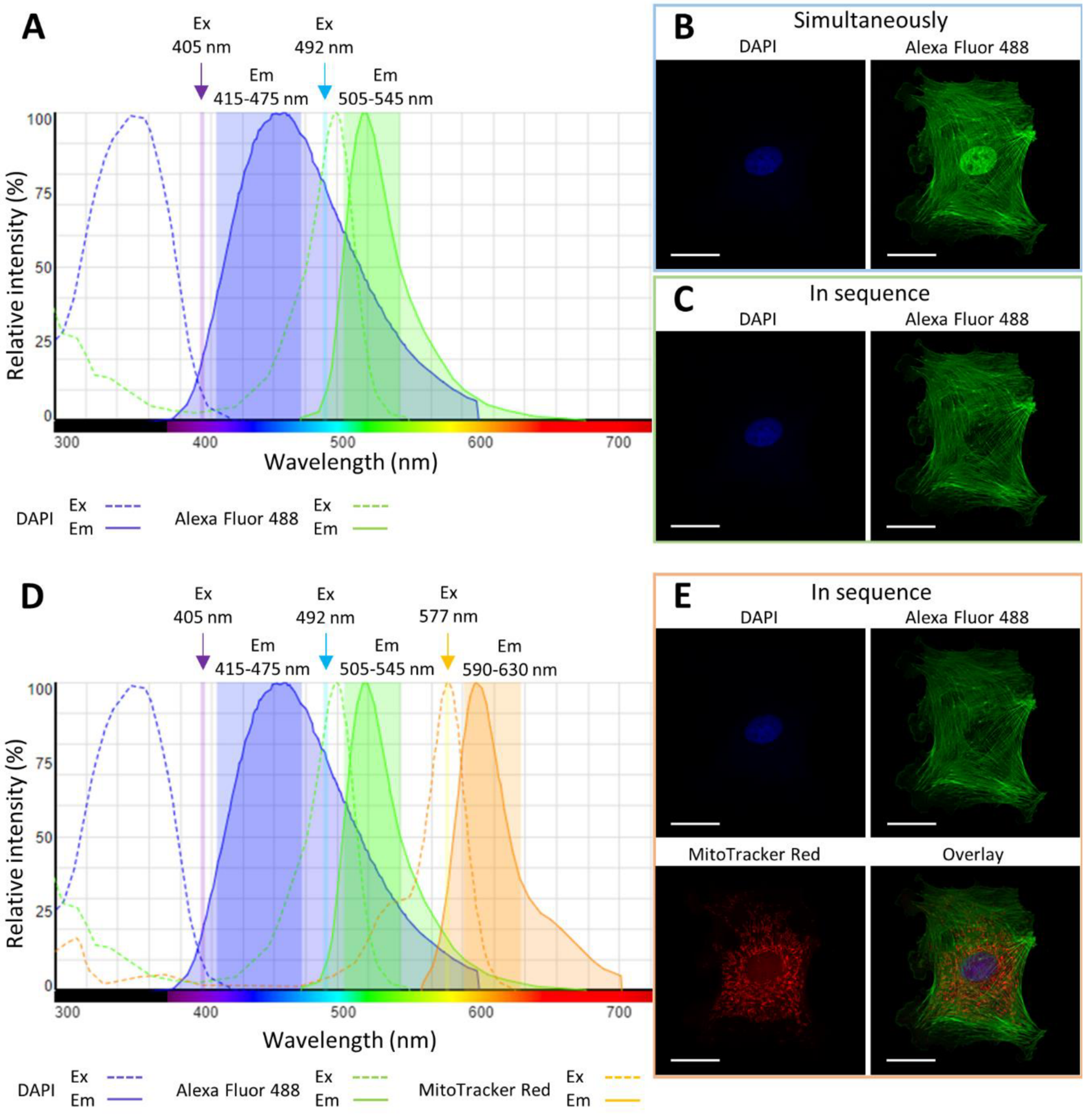

Figure 14. Bovine pulmonary artery endothelial cells, stained with DAPI (nuclei), Alexa Fluor® 488 phalloidin (F-actin) and MitoTracker® Red CMXRos (mitochondria) [156]: (A) Excitation and emission spectra of DAPI, Alexa Fluor® 488 phalloidin and (D) MitoTracker® Red CMXRos with marked excitation (Ex) and emission (Em) wavelength settings (created with Spectra Viewer tool [157]); (B) Fluorescent images from several channels with simultaneous and (C, E) sequential excitation of fluorophores; Confocal microscopy, 63× magnification, scale bar 25 μm.

5 FLUORESCENT MARKERS FOR LONG-TERM EXPERIMENTS

There are a large number of fluorophores, which are intended for fixed cells only. Some of them are designed for immunofluorescence staining when the fluorophore is conjugated to specific antibodies used for the target antigen. In this work it was necessary to focus on the choice of fluorophores to imaging the living cells. The implementation of long-term experiments such as observation of cell migration was planned. Therefore, long-term stability and non-toxicity of dyes were important factors in the selection of fluorophores. Also, the ability to apply semi/fully automatic algorithms for cell segmentation or detection was important to speed up the further analysis of the results.

The study of cell proliferation, motility and migration is based on cell detection. A widely used method is cell detection based on cell nuclei segmentation. DAPI and Hoechst 33342 are the most common dyes for cell nuclei staining used in fluorescence microscopy. Manufacturers generally recommend using DAPI to stain fixed cells. Some manufacturers allow its use even for living cells, but at high concentrations of the dye for better penetration into the cell nuclei. However, this creates a risk of toxic effects of the dye on cells. Hoechst 33342 binds to DNA (A-T regions) and is designed to stain the nuclei of living cells; thus, it is appropriate for live cell imaging and was chosen for this work (Figure 15 (A)). It is, at its optimal concentration which can vary for different cell types, non-toxic and non-mutagenic to cells [158]. Nevertheless, for each cell type, it is necessary to find a suitable concentration. Hoechst 33342 is suitable for staining adherent cells and cells in suspension.

Hoechst 33342 has a blue fluorescent spectrum with excitation and emission wavelengths of 346 and 460 nm respectively [159]. When cells stained with Hoechst 33342 were observed using confocal microscope, the excitation wavelength was set to 405 nm and the detection range was set between 415 and 475 nm. The available confocal microscope was not equipped with a UV laser of a suitable wavelength for this dye excitation, so the closest short wavelength 405 nm laser was used. According to the Hoechst 33342 spectrum (Figure 15 (C)), the excitation efficiency at this wavelength is less than 10%. Therefore, it is impossible to use the lowest concentration and the shortest staining time recommended by the manufacturer. In addition, it is the reason that high laser power is used during image acquisition. These conditions can cause photobleaching effect that can be detrimental to living cells. In this work, an optimal concentration of 50 µM and a treatment time of 15 minutes was determined and used. The nuclei of the studied cell cultures under these staining conditions remained visible and detectable for four hours (data not shown). The toxicity and mutagenicity of the dye have not been tested. In time-lapse experiments, it is necessary to reduce the number and resolution of images from one field of view in order to reduce the negative impact on the vital activity of cells [160, 161]. These limitations can affect the quality of images, which may be insufficient for the application of segmentation algorithms and large time intervals, which will be insufficient for the cell migration tracking. Therefore, in this work, this dye was used only in short-term experiments as a marker for cell counting.

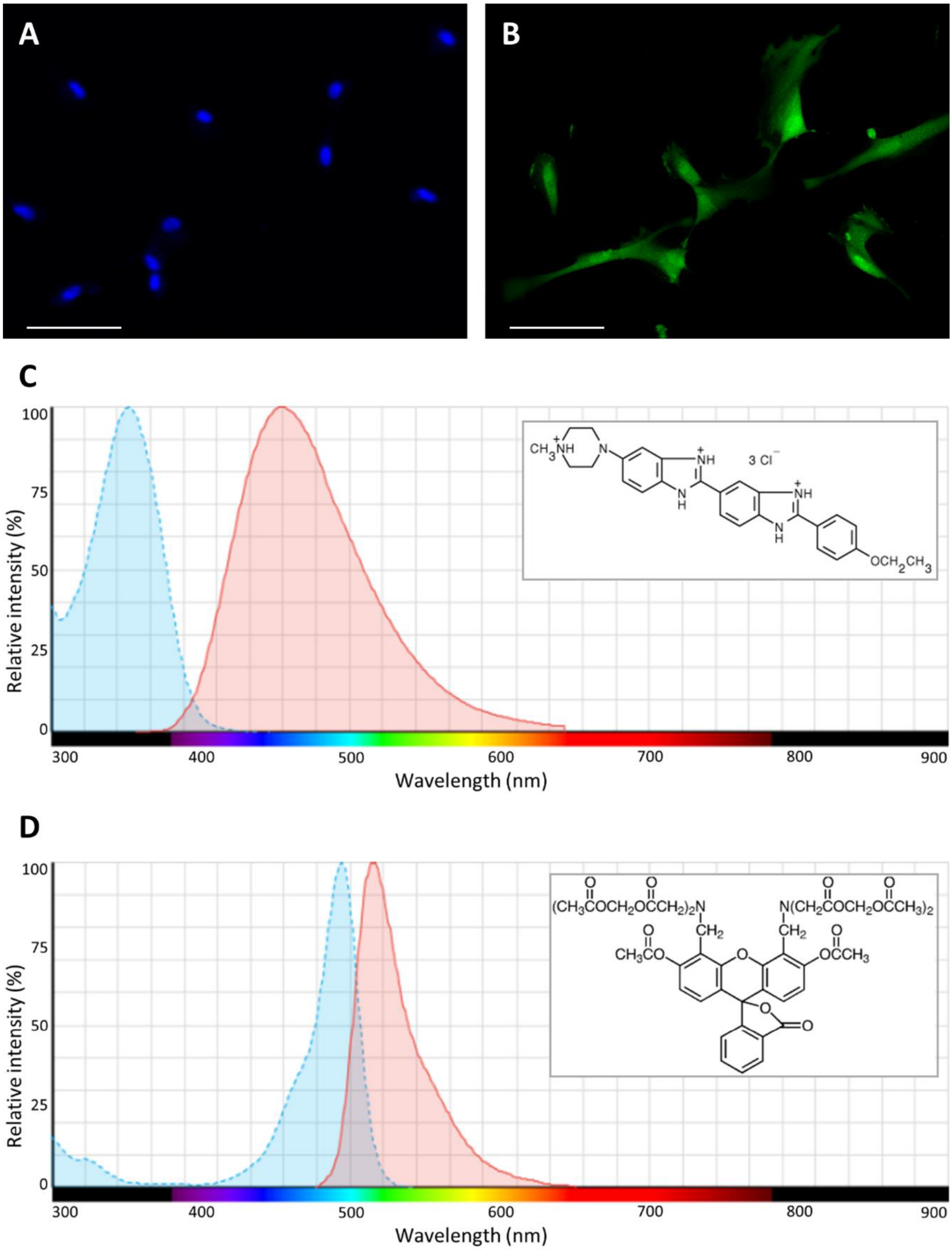

Figure 15. Human adipose-derived mesenchymal stem cells (hMSCs): (A) stained with Hoechst 33342; (B) stained with Calcein-AM. Confocal microscopy, 10× magnification, scale bar 100 µm. The excitation (blue) and emission (red) spectra of (C) Hoechst 33342 [162] and (D) Calcein-AM [163].

Another method suitable for cell detection is the staining of the entire intracellular compartment. With this method of staining, the morphology of the cells is clearly visible, therefore, changes in the shape of the cells and their adhesion can be observed. It can be used to study the single-cell migration, collective cell migration in scratch assay, cell confluency changes during proliferation or when they are under the influence of any factor, cells in microfluidic systems or scaffolds for modelling ECM, etc.

One of the suitable fluorescent dyes is Calcein acetoxymethyl ester (Calcein-AM) which was used in this work. This dye is widely known as suitable for determining cell viability and cytotoxicity assay. Nonfluorescent Calcein-AM penetrates to intracellular compartment, where it converts into green fluorescent Calcein after acetoxymethyl ester hydrolysis by intracellular esterases. Thus, the intracellular compartment is stained and the entire cell is detectable. It is worth considering the fact, that this dye is stable only within four hours, then the rate of dye spontaneous leakage increases [164]. Therefore, Calcein-AM is not recommended for long-term cell research, if the duration of the experiment is longer than four hours. This duration may differ depending on the type of cells and on their metabolism. In some cases, this dye can be detectable even after 24 hours. Usually, in this case the fluorescence is very weak, and the staining is uneven. Depending on the application, this dye can be used for experiments up to 24 hours, but with the given restrictions. Calcein-AM can be used to stain cells in suspension. This has the advantage that the cells can be stained before seeding. This staining method is applicable for seeding cells into an ECM, scaffolds, microfluidic systems, etc. [164, 165]

Calcein-AM was used for study cell proliferation and cell viability. Calcein-AM has a green fluorescent spectrum with excitation and emission wavelengths of 496 and 516 nm, respectively (Figure 15 (D)) [165]. When cells stained with Calcein-AM were observed using confocal microscope, the excitation wavelength was set to 496 nm and the detection range was set between 510 and 550 nm. Based on its spectrum, Calcein-AM is compatible with the aforementioned DAPI and Hoechst 33342 dyes. The excitation and emission wavelength settings for the confocal microscope are shown in Figure 14.

From fluorescent CellTracker™ reagents, the green-fluorescent CellTracker™ Green CMFDA Dye (CMFDA) and the red-fluorescent CellTracker™ Red CMTPX Dye (CMTPX) dyes were chosen for long-term experiments. These probes have the ability to freely pass through cell membranes, where they conjugate with glutathione (glutathione S-transferase-mediated reaction). Glutathione is synthesized in the cytoplasm where it is present at millimolar concentrations (up to 10 mM). In contrast to CMTPX, CMFDA requires enzymatic cleavage. After conjugation with glutathione, non-fluorescent CMFDA is hydrolysed to the fluorescent 5-chloromethylfluorescein by cellular esterases, that cleave off the acetates [166]. Both fluorescent probes evenly stain the cytoplasm (Figure 16 (A, B)). Additionally, CMFDA stains a nucleus compartment, which allows visualization of the entire cell. Also, since they display good fluorescence for a long time (for at least 72 hours), and transferred to daughter cells, these probes are a good choice for cell tracking. [167, 168]

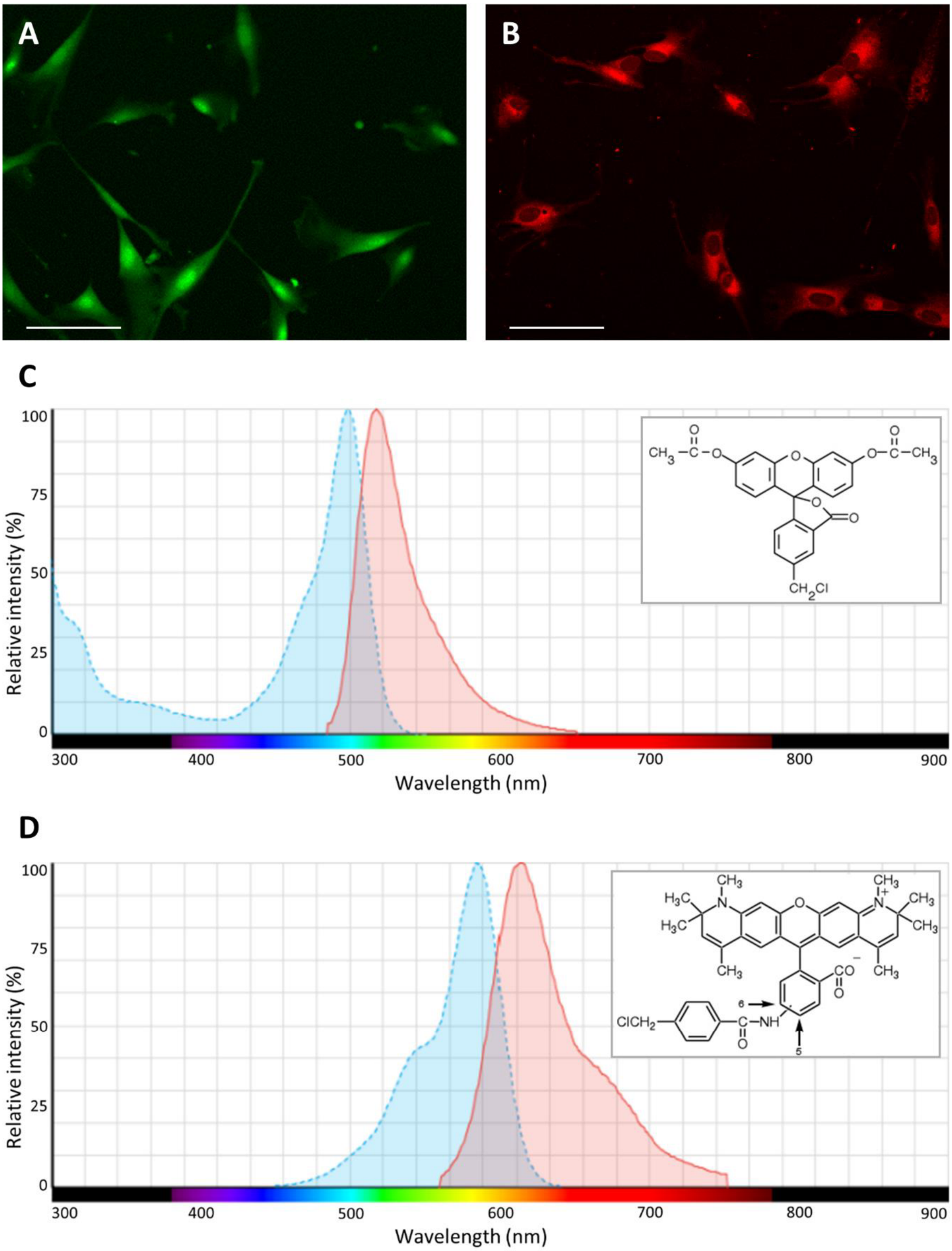

Figure 16. Human adipose-derived mesenchymal stem cells (hMSCs): (A) stained with CellTracker™ Green CMFDA Dye (CMFDA); (B) stained with CellTracker™ Red CMTPX Dye (CMTPX). Confocal microscopy, 10× magnification, scale bar 100 µm. The excitation (blue) and emission (red) spectra of (C) CellTracker™ Green CMFDA Dye [167] and (D) CellTracker™ Red CMTPX Dye [168].

CMFDA has a green fluorescent spectrum with maximum of excitation in 492 nm and emission in 517 nm (Figure 16 (C)) [167]. When cells stained with CMFDA were observed using confocal microscope, the excitation wavelength was set to 492 nm and the detection range was set between 505 and 545 nm. CMTPX has a red fluorescent spectrum with maximum of excitation in 577 nm and emission in 602 nm (Figure 16 (D)) [168]. When cells stained with CMTPX were observed using confocal microscope, the excitation wavelength was set to 577 nm and the detection range was set between 590 and 630 nm. CMFDA and CMTPX were used to monitor cell migration in the long-term experiments, location and proliferation. Based on their spectrum (Figure 16), these fluorescent dyes can be used together. For example, when it is necessary to separate two types of cells on a sample. CMFDA and CMTPX can be used to stain cells in suspension. Furthermore, adherent cells can be stained before subculturing (passage), after which a stained suspension is obtained. Therefore, cells can be stained before seeding. There are some other dyes for whole cell staining, such as ViaFluor® SE Cell Proliferation Kits, but they have not been tested in our laboratory.

Cell membrane staining is another way to mark cells that suitable for subsequent cell detection. It is useful and convenient manner to define cell borders. There are some plasma membrane fluorescent dyes that are suitable for living cells staining. However, most of them are lipophilic dyes, so they are quickly absorbed (by endocytosis). Thus, the staining becomes primarily intracellular. For example, CellMask™ plasma membrane stains and Wheat germ agglutinin conjugates are recommended to use for imaging of living cell membrane for only 30–90 minutes after staining [169, 170]. This is a very short period of time and is usually insufficient for cell motility studies. CellBrite™ Steady Membrane Labeling Kits are the modern alternative cell membrane fluorescent probes [171]. They allow visualization of cell surface membranes of living cells within several days. Their principle is based on the presence of the second component (enhancer), which reduces or eliminates intracellular staining. However, these dyes cannot be used for staining cells in suspension. Also, they are not suitable for co-culture experiments because they are transferred between cells. Therefore, this type of dyes was not chosen for long-term experiments in this work.

The staining of organelles such as mitochondria, vesicles, and others, can also be used to detect cells. In the case where the stained organelles present in large numbers and tend to be evenly distributed in the cytoplasm, the basic algorithms of image segmentation are applicable. Various organelles can be stained with available fluorescent dyes or with fluorescent proteins, such as green fluorescent protein (GFP). Proteins can be successfully introduced into cells using transfection methods [85]. Transfected cells can express fluorescent proteins in different organelles or cell membrane within several days or weeks. The chemical reagents diethylaminoethyl (DEAE)-dextran, calcium phosphate and PEI are commonly used for *in vitro* cell transfection. Proteins form a complex with these chemical reagents, that uptake to cells by endocytosis. Currently, using synthetic cationic lipids and nanoparticles, as SPION, is very popular. These methods have relatively high efficiency of transfected complex transfer, the possibility of using in long-time experiments, in *in vitro* and *in vivo* experiments [86, 90, 172].

5.1 PROPERTIES OF RHODAMINE-DERIVED SUPERPARAMAGNETIC MAGHEMITE NANOPARTICLES

Rhodamine-derived superparamagnetic maghemite nanoparticles (SAMN-R) were available in our laboratory. These nanoparticles have been of great interest. It was necessary to test their compatibility with cell cultures and the possibility of using them in long-term experiments. SAMN-R are iron oxide nanoparticles, which have a spherical shape. Maghemite structure (γ-Fe_2O_3) of prepared iron oxide nanoparticles was determined on the first day after preparation and confirmed in one year using Mössbauer spectroscopy [60, 61, 92]. Preparation protocol was previously published in several studies [60, 61, 91, 92, 141]. SAMN-R colloidal suspension dissolved in water showed that it can maintain their colloidal stability at least six months [92]. Distribution of nanoparticle diameter and polydisperse index was quantified using dynamic light scattering (DLS, Zetasizer Nano ZS, Malvern Instruments). Value of polydisperse index was 0.22 ± 0.03 in dH_2O and 0.47 ± 0.03 in culture growth medium [141]. These nanoparticles size varied mainly from 20 to 50 nm (Figure 17), that was confirmed in several previous studies [58, 60, 88, 92] with use of scanning electron microscope (SEM) and transmission electron microscope (TEM). SAMN-R are functionalized with Rhodamine B isothiocyanate fluorescent dye (Figure 17 (C)). The rhodamine shells on the maghemite surface are shown in Figure 17 (A, B) [92].

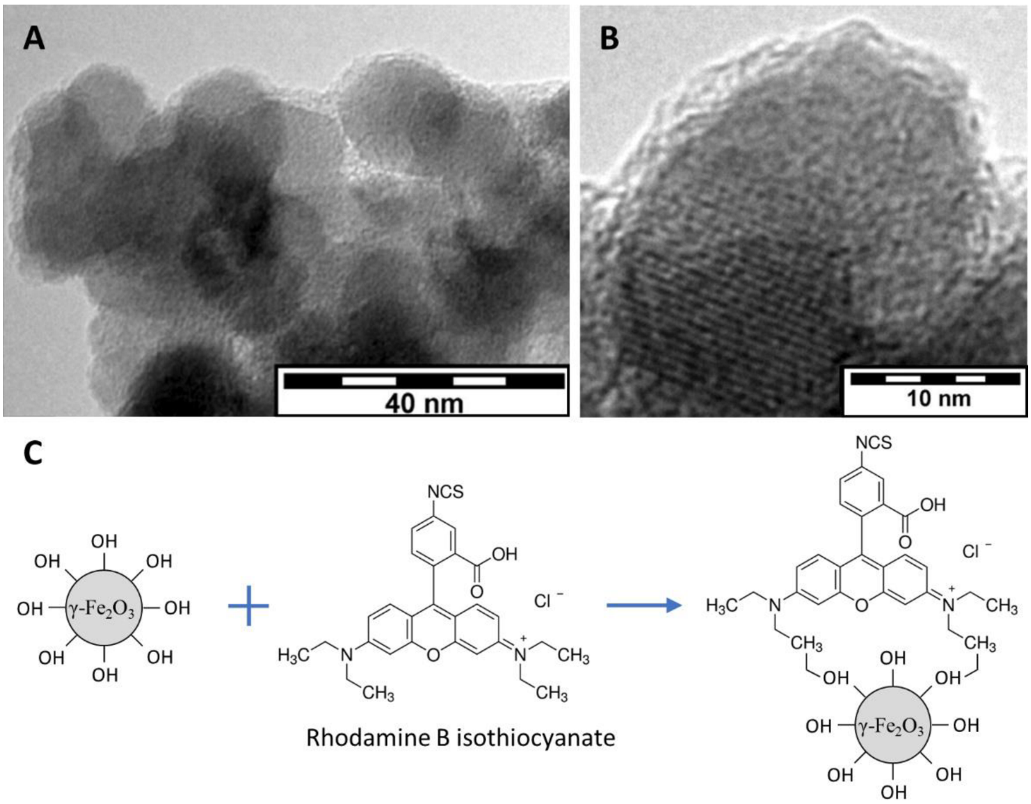

Figure 17. Microscopic image of Rhodamine-derived superparamagnetic maghemite nanoparticles (SAMN-R) demonstrating the rhodamine shell on the maghemite surface. TEM, (A) scale bar 40 nm, (B) 10 nm [92]. (C) Schematic formation of rhodamine bound magnetic nanoparticles.

Since there was an interest in using iron oxide nanoparticles in *in vitro* research, SAMN-R were applied in cells treating study. In the initial study it was confirmed that iron oxide nanoparticles penetrate intracellular compartment and are located in the cell cytoplasm [58, 60, 91]. Cells were treated with nanoparticles about 24 hours [58, 60, 61, 141] or 48 hours [58, 60]. In the study [60], MSC cells were treated with iron oxide nanoparticles for 48 hours and then stained with Prussian blue to confirm the nanoparticles penetration into the cell cytoplasm. Then in continuation of the study [58, 59], it was shown that iron oxide nanoparticles are localized in endosomes or lysosomes surrounding cell nuclei (Figure 18 (A, B)). It was confirmed mainly by SEM and TEM.

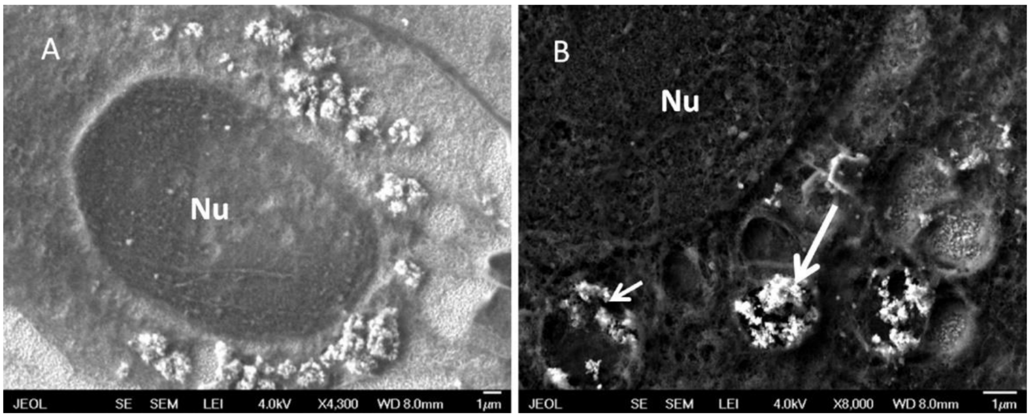

Figure 18. Microscopic image of human mesenchymal stem cells (hMSCs) treated with superparamagnetic iron oxide nanoparticles (SPION): (A) Distribution of vesicles around the nucleus (Nu – labelled cell nucleus); (B) Detail of the nucleus surrounded by a clear region of endosomes containing nanoparticles (white arrows). Field emission SEM, magnification (A) 4300×, (B) 8000× (JEOL 7401F), scale bar = 1 µm. [58]

Additional analysis using confocal microscopy technique was performed in the studies [61, 141]. In the study [61], hMSCs were treated with SAMN-R and then LysoBrite fluorescent marker (Cell Navigator™ Lysosome Staining Kit-green, AAT Bioquest) was applied for lysosomes staining. Since excitation and emission spectrum of SAMN-R and fluorescent marker used do not overlap, it was possible to detect SAMN-R and lysosome localization separately. In Figure 19 (A) hMSC cells stained with SAMN-R and LysoBrite dye are shown. The fluorescence intensity profiles of SAMN-R (red channel) and LysoBrite (green channel) overlap shows that nanoparticles are mainly localized in lysosomes (Figure 19 (C)). In Figure 19 (E) hMSC cells stained with SAMN-R and Hoechst 33342 nuclei dye are shown. The fluorescence intensity profiles of SAMN-R (red channel) and Hoechst 33342 (blue channel) overlap shows that they are located in different areas of the cell (Figure 19 (G)). The intensity of noise in the background and in the area inside nuclei shows that SAMN-R are located mainly in cytosol or in intracellular organelles. It is important to mention that SAMN-R nanoparticles were not present in the cell nuclei [58, 60, 141] (Figure 18, Figure 19 (E, G)). It was observed on 3T3 cells, hMSCs and HL-1 cells.

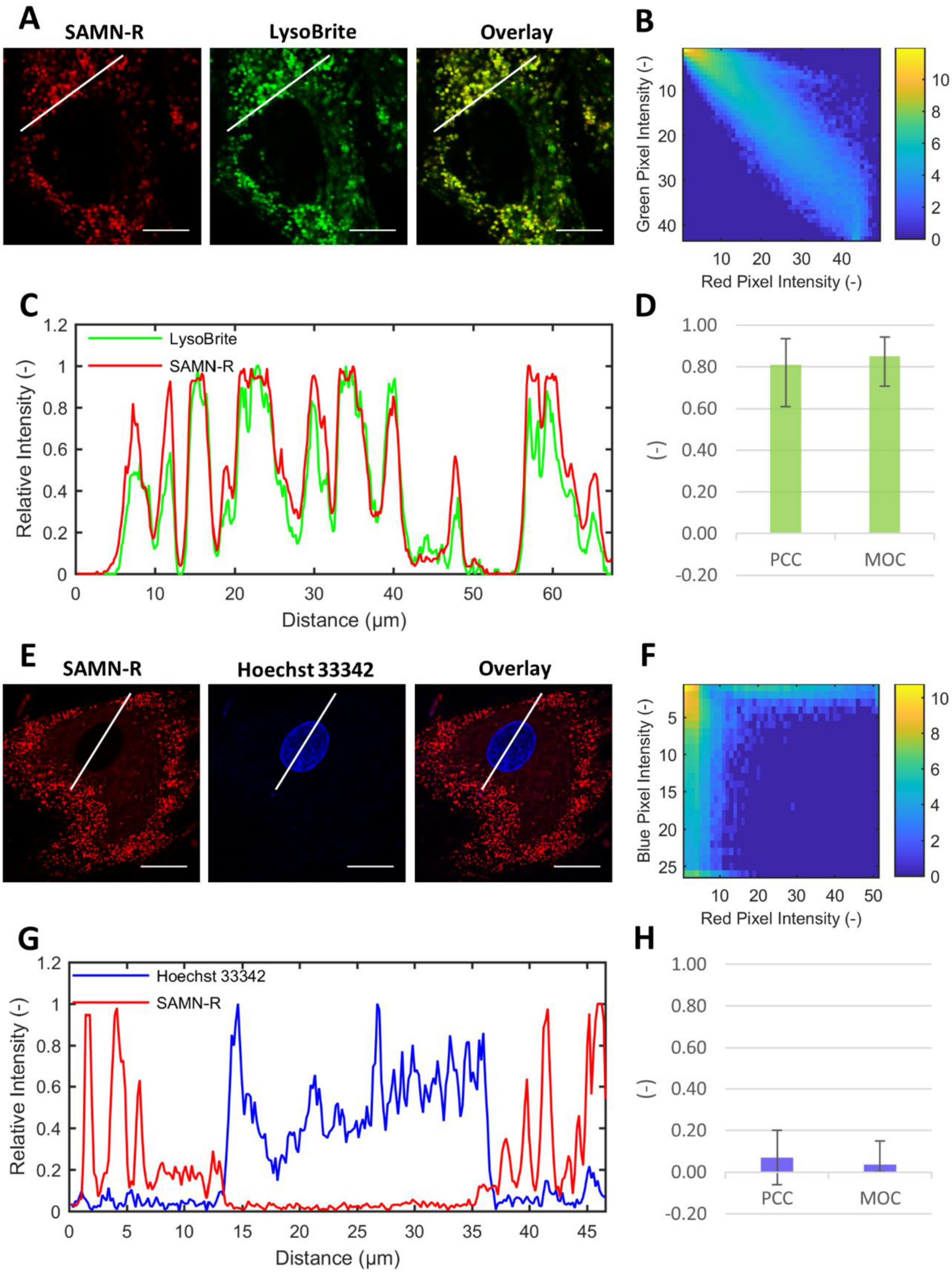

Figure 19. Colocalization analysis of rhodamine-derived superparamagnetic maghemite nanoparticles (SAMN-R): (A) Human mesenchymal stem cells (hMSCs) marked with SAMN-R and LysoBrite dye (Cell Navigator™ Lysosome Staining Kit-green) and (E) hMSCs marked with SAMN-R and Hoechst 33342 dye (scale bar 25 μm); (C, G) relative intensity profile of the pixel values under the white line; (B, F) Scatterplot of red and green pixel intensities of the images shown in (A) and scatterplot of red and blue pixel intensities of the images shown in (E); (D, H) Pearson's correlation coefficients (PCC) and Manders overlap coefficient (MOC) of 20 images of internalized SAMN-R and LysoBrite in hMSC and 20 images of internalized SAMN-R and Hoechst 33342 in hMSC.

Colocalization analysis is also presented graphically using scatterplots. Figure 19 (B) shows 2D histogram between the intensities of red pixels from the SAMN-R channel versus the intensity of the green pixels from the LysoBrite channel. Based on the shape of the 2D histogram that shows the clustered values around the diagonal, the high correlation between the colour channels can be observed. It means that images from these channels are colocalized. Figure 19 (F) shows the comparison of the image from the red (SAMN-R) channel with the image from the blue (Hoechst 33342) channel. In this graph the points are distributed into two groups. High-intensity pixels from one channel overlap with low-intensity pixels or pixels without signal in the second channel. Images from these channels are not colocalized.

In addition, a quantitative analysis of colocalization of images from two channels was performed using Pearson's correlation coefficient (PCC). The PCC for images acquired from two channels is calculated as [173]:

$$PCC = \frac{\sum_i (X_i - \bar{X}) \times (Y_i - \bar{Y})}{\sqrt{\sum_i (X_i - \bar{X})^2 \times \sum_i (Y_i - \bar{Y})^2}} \tag{4}$$

where X_i and Y_i refer to the intensity values of the first and second channels, respectively, of pixel i, and $\bar{X}$ and $\bar{Y}$ refer to the mean intensities of the first and second channels, respectively, across the entire image. When two images are perfectly colocalized then PCC value is near 1. PCC is near zero when images from two channels are not colocalized. Inverted images have a coefficient of -1. Usually, fluorescent images have a noise on the background. This can distort the results, because the pixels with positive intensity from the noise on both channels can be coincident. Based on [173], it was decided to use also Manders overlap coefficient (MOC), that is sensitive to detect coincident pixels in both channels at all signal levels. MOC value is sensitive for background. Therefore, it is recommended to use thresholded (binary) images. MOC is described by the equation:

$$MOC = \frac{\sum_i (X_i \times Y_i)}{\sqrt{\sum_i X_i^2 \times \sum_i Y_i^2}} \tag{5}$$

where X_i and Y_i refer to the intensity values of the first and second channels, respectively, of pixel i. When this value is near 1, then images from two channels are colocalized. And when this value is near zero, then images are not colocalized [173].

Graphs in Figure 19 (D) shows PCC and MOC values obtained from 20 microscopic images of hMSCs treated with SAMN-R and stained with LysoBrite lysosomal dye. The number of nanoparticles penetrated into cells, quality of lysosome staining, and the level of background noise affect the values of these coefficients. Nevertheless, these values indicate that SAMN-R nanoparticles are located mainly in lysosomes. Figure 19 (H) shows PCC and MOC values obtained from 20 microscopic images of hMSCs treated with SAMN-R and stained with Hoechst 33342 nuclei dye. Hoechst 33342 can stain mitochondria. Usually, a signal from the mitochondria area is very low and can be easily removed by applying a threshold for image segmentation.

The intensity level of noise in the background and in the area inside nuclei is similar. Thus, it can be perfectly removed by applying threshold too. The performed quantitative colocalization analysis confirmed that SAMN-R nanoparticles are not localized in cell nuclei.

Leica TCS SP8 X confocal microscope is equipped with white light source [68]. WLL in conjunction with AOTF allows to select specific excitation wavelengths from 470 to 670 nm. Emission detection range is detected by sensitive HyD. This technical solution enables explore the spectral properties of the fluorescence dyes. For this purpose, LasX Leica confocal software is equipped with Lambda square (λ^2) fluorescence mapping function [174]. The optimal SAMN-R spectrum was determined with this function. In the previous study [92], the spectrum of SAMN-R suspension in water was controlled using fluorescence spectroscopy. The excitation wavelength was determined at 554 nm and the emission wavelength at 580 nm. In this work, it was necessary to determine a spectrum of SAMN-R within cells.

Microscopic images were acquired using Leica TCS SP8 X confocal microscope with 10× magnification. Excitation wavelength interval was set from 470 to 670 nm with a step of 10 nm. Emission interval range was set from 480 to 700 nm with bandwidth of 20 nm. Images were obtained with a resolution of 512 × 512 pixels and a scan speed of 100 Hz. In this experiment, hMSCs treated with SAMN-R were observed. In each obtained sequence 3–5 ROIs were selected (fluorescent marked area of cells), the total number was 70. To be able to compare the spectrum of 70 ROIs their values were normalized. The averaged spectrum is demonstrated in Figure 20. Maximum of excitation and emission is on 560 nm and 581 nm, respectively. These wavelengths were defined as optimal for image acquisition. Accordingly, when stained with SAMN-R nanoparticles cells observed by confocal microscope, then excitation wavelength was set at 560 nm and the detection range was set between 570 and 610 nm.

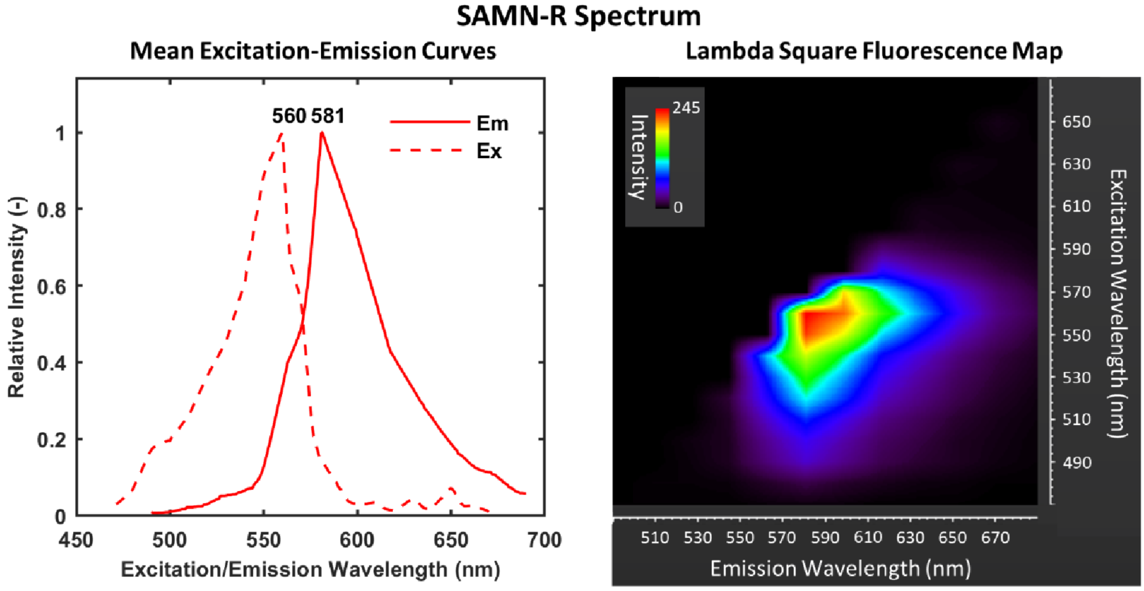

Figure 20. Excitation and emission spectra (left) for rhodamine-derived superparamagnetic maghemite nanoparticles (SAMN-R) obtained by mean lambda square fluorescence maps. Example of lambda square fluorescence map (right).

5.2 IMAGE PROCESSING

5.2.1 ALGORITHM FOR MEASUREMENT OF CELL CONFLUENCY

Cell morphology and proliferation rate can be used to assess the health of the cells. Confluency is one of the indicators of cell proliferation. It is defined as the percentage of the surface of a culture vessel that is covered with adherent cells. Confluency and cell count are directly proportional [175, 176]. By the area of coverage of the adherent cells, it is possible to determine whether they are in normal conditions. Fluorescence microscopy can be useful when cells are cultured in various 3D scaffolds because in some cases it is impossible to focus on cells inside construction, especially if the cultivation surface is not flat. Also, based on the measurement of confluency, the transfection efficiency of the fluorescent protein can be assessed. The analysis of confluency has wide application. This prompted the development of programs for the image-based analysis of biological samples to include this application [134–136]. These programs include analysis of microscopic images obtained with PCM, light and fluorescence microscopy.

In this work, MATLAB (The MathWorks, Inc.) computing environment was used to implement the developed method for the image processing and segmentation of the fluorescence images. This algorithm (Figure 21) is designed to detect cells marked with a fluorescent dye, that stains whole cells. In this work Calcein-AM and CMFDA cell tracker dyes were used. When images are acquired using a fluorescent confocal microscope, then the focal plane should be set very close to the surface of the culture vessel. Also, the surface plane of the culture vessel may be slightly tilted. In this case the images from the several focal planes can be acquired. Then, this z-stack can be averaged to avoid errors due to the possible tilt of the sample. Analysis of cell confluency provided by suggested algorithm [176] (Figure 21):

1. Noise is reduced by linear image filtering with Gaussian low pass filter,
2. Binary image of segmented cells is obtained by thresholding of the parametric image (threshold value was set experimentally),
3. Individual false positive pixels are removed by median filtering,
4. Confluency is determined as an area ratio of white to black pixels.

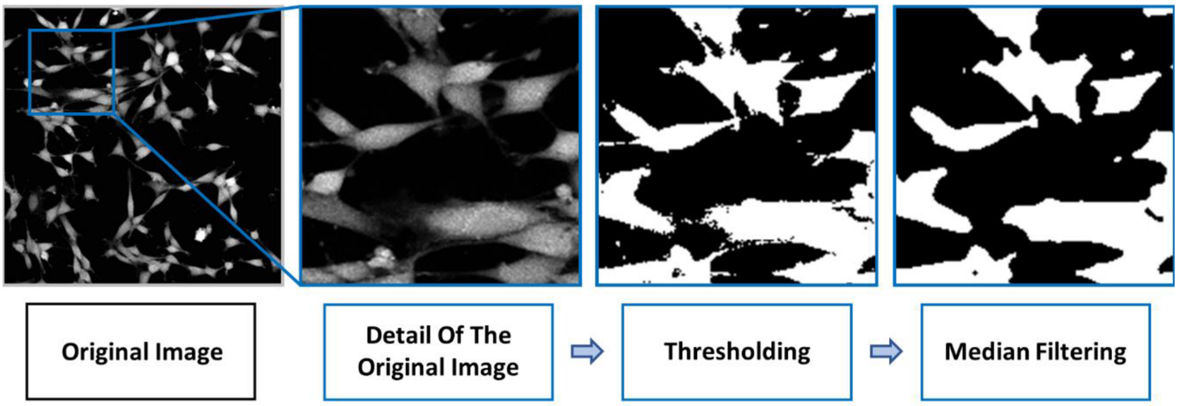

Figure 21. Image processing pipeline for evaluating of cell confluency. From left to right: original grey-scale image processed by a Gaussian low pass filter; thresholded binary image; Individual false positive pixels are removed by median filtering.

5.2.2 ALGORITHM FOR QUANTITATIVE ANALYSIS OF SCRATCH ASSAY

Gap closure or healing/scratch assay is a widespread use method for investigating collective cell migration. A gap is made at confluent cell monolayer. The cells then tend to migrate into free area and close the gap. A quantitative method is based on calculating the open area present at the scratch area in the middle of the microscopic image. Usually, the images are obtained at several time intervals up to close the gap. Then from the images obtained at different times the width or area of the scratch are determined and compared. Commonly used algorithms are based on scratch borders detection. Usually, the borders of the scratch are uneven (Figure 22), so the open area unevenly closes. In some part, the scratch closes faster. Therefore, quantification analysis based on open area calculation is preferable. It may be expressed using metric scales or as the percentage change in normalized measurement area to the initial open area [133, 177, 178]. In this work, the images acquired for each sample were analysed quantitatively by a custom algorithm using MATLAB software. This algorithm is designed for bright-field and fluorescence images, where cells are marked with a fluorescent dye, that stains whole cells. In this work, CMFDA cell tracker dye was used to stain the intracellular compartment. When the z-stack was obtained in a fluorescent channel, then it was summed at the beginning of an algorithm. The scratch measurement is provided by following algorithm (Figure 22) [141]:

1. Thresholding of fluorescent image with manually selected threshold,
2. Morphological filtering by closing and filling holes,
3. Determination of scratch borders by morphological filtering,
4. Computation of mean scratch width over all rows and scratch area.

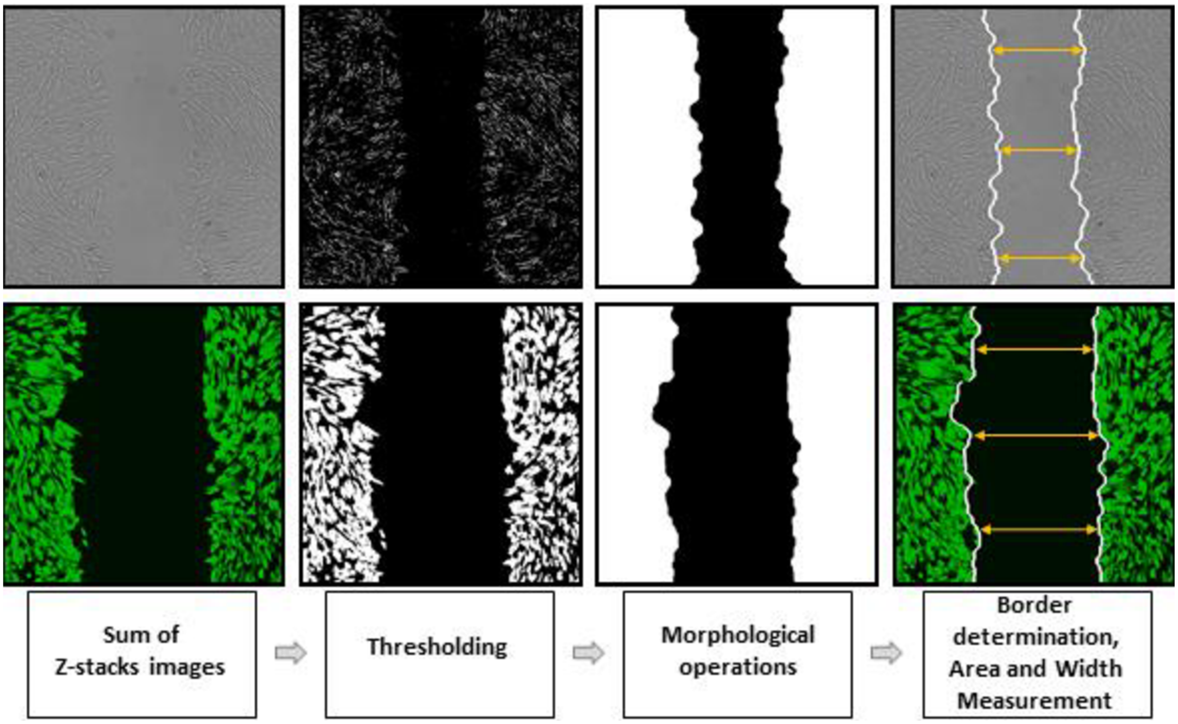

Figure 22. Basic pipeline of image processing approach for automatic scratch assay analysis. From left to right: original grey-scale image with pseudo-coloured cells; thresholded binary image; segmented image after application of morphological operations with detected scratch border; original image merged with detected scratch border, schematic of scratch width measurement.

5.2.3 CELL NUCLEI DETECTION

In this work, an algorithm for detecting nuclei stained with a fluorescent dye was designed. The use of this algorithm helps to replace most of the routine manual cell marking. The automatically detected false positive and false negative cell nuclei were manually corrected. Usually, the images were acquired in parallel in fluorescence channel and bright field. In the bright field channel, we can see the cell morphology, that helps to control the false detections. The MATLAB computing environment was used to implement the image processing algorithm.

The cell counting was performed by semi-automatic determination of the number of cell nuclei (Figure 23), which were stained with Hoechst 33342. Proposed algorithm [141] can be briefly described in a few steps:

1. Noise is reduced by linear image filtering with Gaussian low pass filter,
2. Nuclei edges are enhanced by a computation of a local standard deviation,
3. Binary image of segmented nuclei is obtained by thresholding of the parametric image (threshold value was set experimentally),
4. Individual false positive pixels are removed by median filtering,
5. Mutually adherent cells in binary image are divided by computation of a distance transform and subsequent application of watershed segmentation algorithm,
6. False positive groups of the smaller number of pixels than experimentally selected threshold value are excluded,
7. Centroids of the remaining binary objects are counted – number of cells,
8. Result can be eventually manually modified – correction of possible false positive/negative detections.

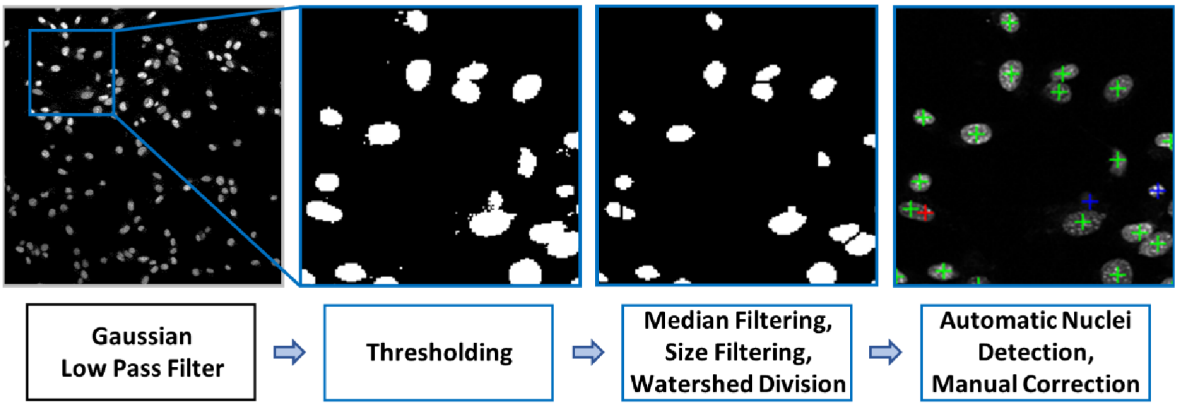

Figure 23. Image processing pipeline for semi-automatic cell counting. From left to right: original grey-scale image processed by a Gaussian low pass filter; resized thresholded binary image; resized image with nuclei divided by a watershed algorithm; resized image with nuclei with marked centroids; the resulting image of centroids after manual corrections mapped to the resized original grey-scale image: positive detections are marked with green plus sign, false positive with red plus sign, false negative with blue plus sign.

There are several factors that affect the success of nuclei segmentation. The shape of the nuclei is not perfectly round and the size of some of them can differ significantly in the microscopic image. Dividing cells change their size and shape during the phases of mitosis. Particularly noticeable the large nuclei size in the metaphase, ellipsoidal nuclei shape in the anaphase, and small nuclei size in the telophase. In cells that are in contact, the nuclei can be at a very small distance from each other. Those nuclei can be connected in the binary image after threshold operation. Then the watershed segmentation algorithm can help to separate connected nuclei. Unfortunately, this algorithm can also split the ellipsoidal nuclei. Consequently, false-positive detection can occur (see red plus sign in Figure 23). Also, the nuclei of some cells can be less stained due to different degrees of dye absorption, therefore, they are less intense. Also, it is necessary to pay attention to the staining principle. For example, molecules of Hoechst 33342 bind to DNA, thus nuclei are stained unevenly, and weak fluorescence can be observed in mitochondria. At the threshold phase of the segmentation algorithm, unevenly and less stained nuclei can be detected as noise or several small objects. Therefore, false-negative or false-positive detections may occur. In this case, noise level and image resolution are important factors.

The surface plane of the culture vessel, which is on the microscope stage, may be slightly tilted. This can be facilitated by inaccuracies in the manufacture of culture vessels or in their placement on the microscope stage. A change in the temperature of the culture vessels material may also cause slight deformations. Using confocal scanning microscope, we get an image of an object slice from the focal plane. When the culture vessel is slightly tilted, then the focal plane is in the different height of cells, which are on opposite sides of the field of view. The differences in the transparency, intensity, and size of the objects in different parts of the microscopic image can appear. Thus, the number of false-negative detections may increase. When the images from the several focal planes can be acquired, these z-stacks can be averaged at the beginning of the algorithm to avoid errors due to the possible tilt of the sample. However, in some cases, it is impossible to increase the number of z-stacks, for example, in time-lapse experiments due to the time limit.

Usually, when there are a small number of cells in the image, there are only a few false detections. Threshold value is set manually, and its value is chosen experimentally. With a small number of objects, it is easier to select the optimal threshold value to minimize false detections. With a large number of nuclei in the image, there is a high probability of finding adjacent, small, large, low-intensity and/or ellipsoidal nuclei. Therefore, the amount of false-positive and false-negative detections increases. The sensitivity of the algorithm is stable, even with a large number of nuclei in the microscopic image. The values of calculated sensitivity (true positive rate (TPR)), positive predictive value (PPV) and F1-score are shown in Figure 24. These values were statistically analysed using MATLAB software. Firstly, it was controlled whether the values in each group are normally distributed using the Shapiro-Wilk test (Table 1) [179]. The null hypothesis states that the values of compared groups are normally distributed. When p-value is greater than 0.05, then the data are normally distributed (marked in bold in the Table 1). When the p-value is less than 0.05, then the tested data significantly deviate from a normal distribution.

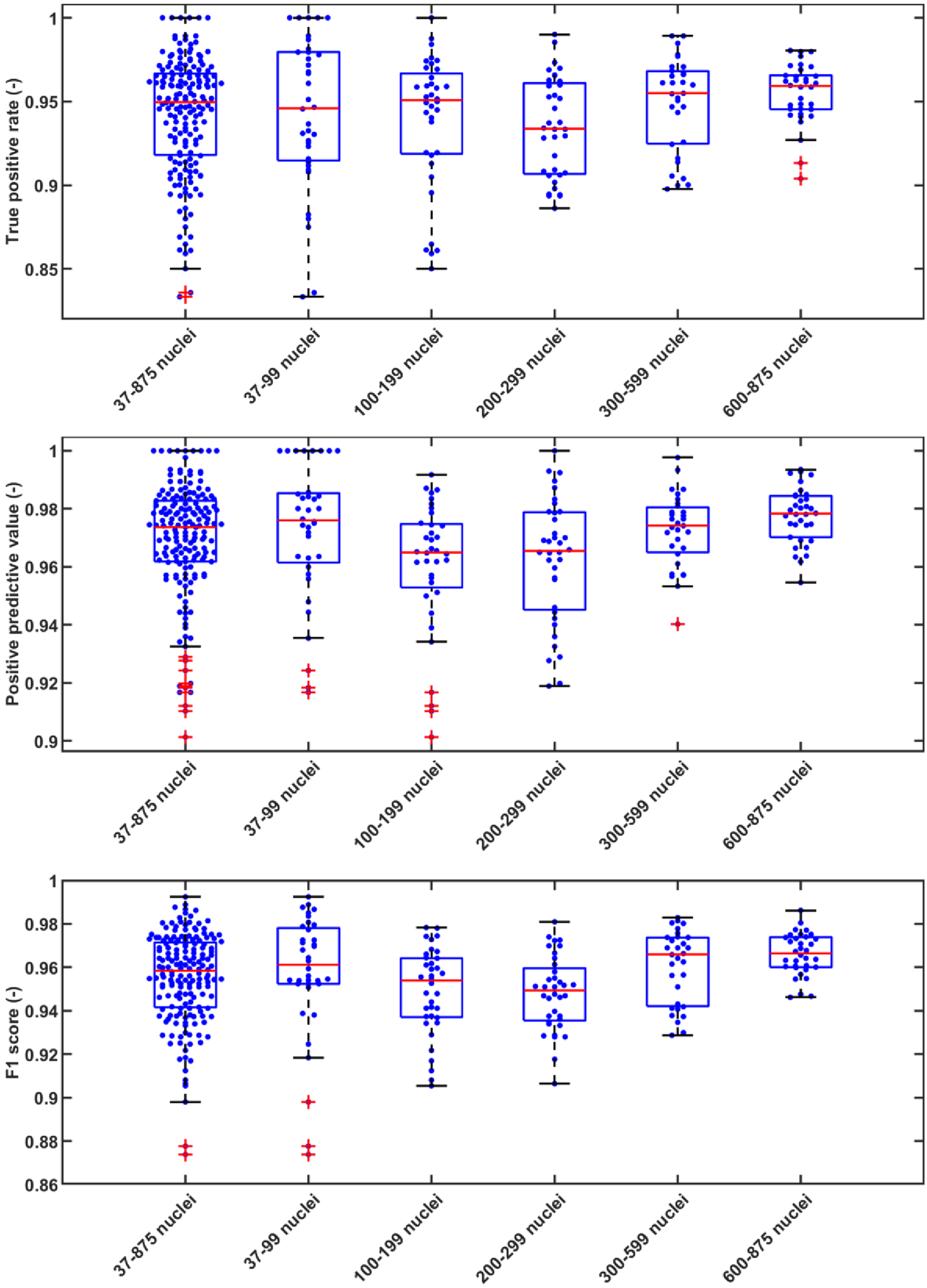

Figure 24. The values of sensitivity (true positive rate (TPR)), positive predictive value (PPV) and F1-score of presented semi-automatic nuclei detection algorithm. The first boxplots display values from all microscopic images. Then boxplots from the groups, divided by the number of nuclei in the image, are presented separately.

The results of this test show that the data in some groups are not normally distributed. Therefore, the Kruskal-Wallis nonparametric test [180] was used to determine whether any of the differences between the medians of compared groups are statistically significant (Table 1). The null hypothesis states that the medians of compared groups are equal. When the p-value exceed 0.05 (marked in bold in the Table 1), then the differences between the medians are not statistically significant. When the p-value is lower (or equal) than 0.05, then the differences between some of the medians are statistically significant. [180]

Table 1. Statistical test applied on values of sensitivity (true positive rate (TPR)), positive predictive value (PPV) and F1-score of presented semi-automatic nuclei detection algorithm. Table of p-values from Shapiro-Wilk and Kruskal-Wallis statistical tests. P-values greater than 0.05 marked in bold (null hypothesis is accepted). A first group includes all the studied microscopic images. The following groups are divided by the number of cells in the image.

	Statistical test					
	Shapiro-Wilk (p-value)			Kruskal-Wallis (p-value)		
Group	TPR	PPV	F1-score	TPR	PPV	F1-score
37-99 nuclei	0.0274	0.0449	**0.1560**	**0.1010**	0.0015	0.0000
100-199 nuclei	0.0019	**0.7337**	**0.1211**			
200-299 nuclei	**0.0834**	**0.1976**	**0.7740**			
300-599 nuclei	0.0148	**0.6656**	0.0132			
600-875 nuclei	**0.3335**	**0.6048**	**0.5644**			

It was confirmed that the differences between the medians of TPR are not statistically significant. Therefore, it can be assumed that the medians of the sensitivity do not depend on the density of cells in the images. However, the PPV and F1-score in images with different cell densities are statistically significant.

The difference between each group was calculated separately using Tukey-Kramer post hoc test (Table 2) [181]. This test compares all possible pairs of means of groups, whether they are equal. The null hypothesis states that the means of two groups are equal. When the p-value is less than 0.05, then we can reject the null hypothesis.

The results of this test show that the differences between the sensitivities of nuclei detection algorithm applied on images with different cell number in the image are not statistically significant. The significance of correctly true positive detected nuclei in images with different cell number are randomly distributed. The dependence of the p-value when comparing groups with a larger and smaller number of cells was not revealed. PPV values are irregular. Therefore, values of F1-score are randomly distributed when comparing groups with each other.

Table 2. Statistical test applied on values of sensitivity (true positive rate (TPR)), positive predictive value (PPV) and F1-score of presented semi-automatic nuclei detection algorithm. Table of p-values from Tukey-Kramer statistical test. P-values greater than 0.05 marked in bold (null hypothesis is accepted).

		Statistical test		
		Turkey-Kramer (p-value)		
Compared groups		TPR	PPV	F1-score
37-99 nuclei	100-199 nuclei	**0.9915**	**0.0586**	0.0324
37-99 nuclei	200-299 nuclei	**0.5312**	0.0193	0.0044
37-99 nuclei	300-599 nuclei	**0.9998**	**0.8974**	**0.9905**
37-99 nuclei	600-875 nuclei	**0.8240**	**1.0000**	**0.9924**
100-199 nuclei	200-299 nuclei	**0.8789**	**0.9997**	**0.9902**
100-199 nuclei	300-599 nuclei	**0.9608**	**0.5485**	**0.1823**
100-199 nuclei	600-875 nuclei	**0.4637**	0.0340	0.0041
200-299 nuclei	300-599 nuclei	**0.4015**	**0.3395**	0.0412
200-299 nuclei	600-875 nuclei	0.0463	0.0100	0.0004
300-599 nuclei	600-875 nuclei	**0.9402**	**0.8206**	**0.8451**

The values of TPR, PPV and F1-score are the highest in the images with cell number lower than 100. On these images the number of false detections is lower in comparison with the images with a larger cell number. In the used microscopic images, the cell confluency reaches 100% when the number of cells is more than 300. On these images there are more false detections. Cell nuclei detection in such images requires a large number of corrections of false detections. Nevertheless, the number of false detections relative to the total number of cells is low. This explains the high values of the TPR, PPV and F1-score on the groups with large number of cells in the image.

5.2.4 CELL TRACKING ALGORITHM

Cell detection provided by suggested algorithm (Figure 25):

1. Noise is reduced by non-linear image filtering with median filter,
2. Binary image of segmented cells is obtained by thresholding of the parametric image (threshold value was set experimentally),
3. The connection of cell filopodia, that have a low intensity at the original image, with cell body and separation of potentially touch cells is performed using morphological operations (fill holes, open),
4. Objects located on the border of images are excluded,
5. Elimination of the false positive objects with small area size, in comparison with the size of cells,
6. Detection of centres of mass on the remaining objects.

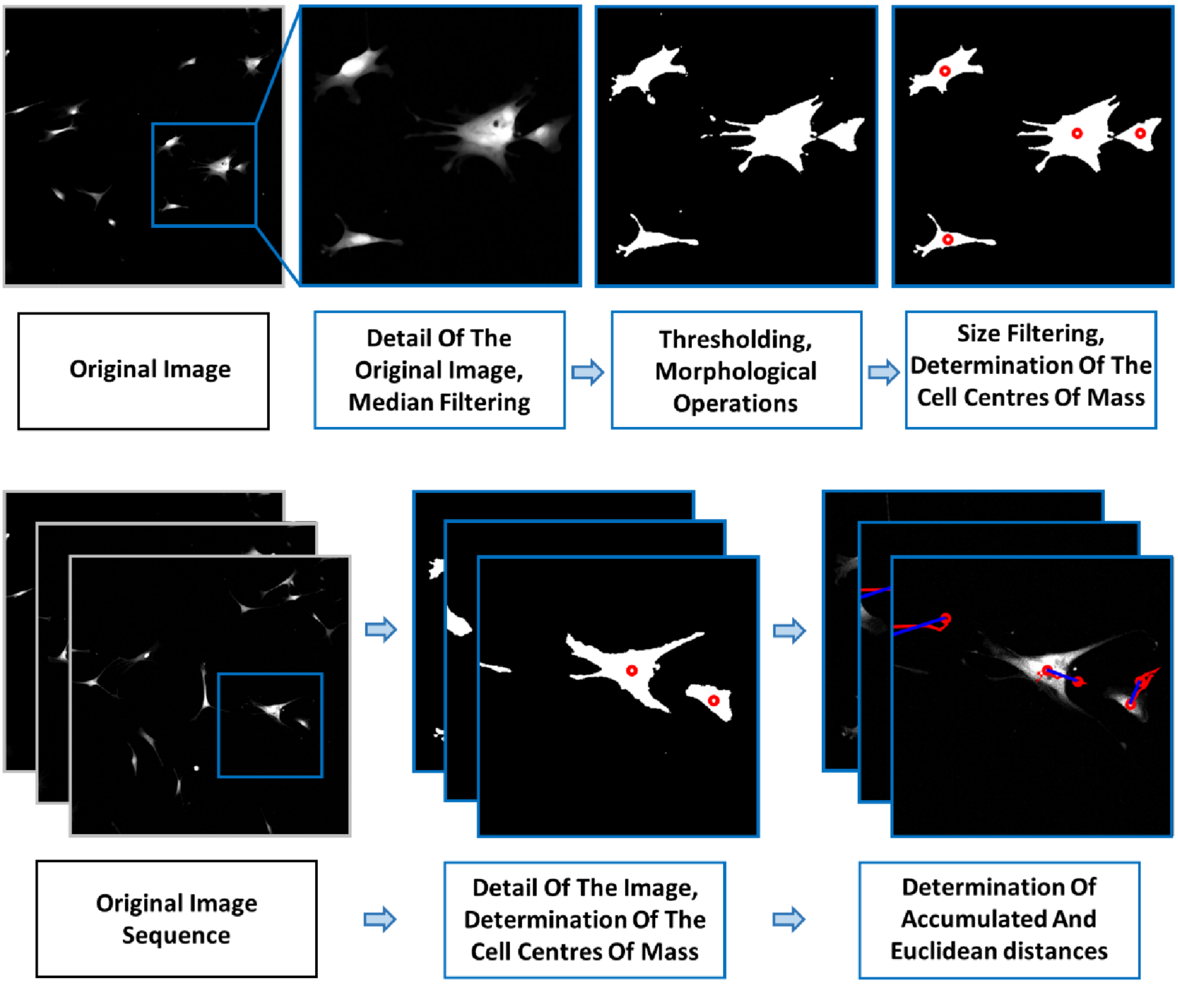

Figure 25. Image processing pipeline of cell detection and cell tracking. On the top images from left to right: original grey-scale image; detail of the original image processed by median filter; thresholded binary image followed by application of morphological operations; small false positive objects removed and centres of mass of the cells determined, marked with red circle. At the bottom images from left to right: acquired image sequence from time-laps experiment with a marked area in a blue square; detection of the cell centres of mass at the image sequence (algorithm is on the top) showed on the marked area; determination of the accumulated (red) and Euclidean (blue) distances.

This algorithm was introduced in [24]. It is designed to detect cells marked with a fluorescent dye, that stain whole cells, such as CMFDA cell tracker dye and Calcein-AM, that were used in this work. This algorithm for cell detection can be applied for image sequences. Thereby, it is possible to determine the position of the cells in each time interval. Then migration tracks can be calculated from subsequent coordinates. For example, see accumulated and Euclidean distances visualised on the original microscope image on the Figure 25. Unfortunately, cells can extend beyond the edges of the field of view with time. In addition, high cell density, connected cells and cells in the phases of mitosis may cause complications in cell segmentation. In this algorithm that objects were manually removed. Also, it is not suitable for images with high cell density.

The method of cell identification in the different frames can be improved by applying other successful methods. For example, in [182] segmentation of whole cells was performed in each image in described stacks from the one field of view. Then segmented cells in two adjacent images were compared. Cell in two frames was determined as the same, when their segmented area in the first frame overlaps the most with the location of segmented cell in the next frame. This method is acceptable, when observed cell type do not move quickly and when frame rate is selected appropriately.

Presented algorithm was used during the first experiments where only stained cells were used together with a short frame rate (2.5 min). The experimental protocol was subsequently changed. It was decided to observe several cell groups simultaneously. Therefore, the number of fields of view and frame rate were increased. Also, it was necessary to change time interval due to photobleaching effect. The frame rate from five to ten minutes was defined as optimal. Then it was decided to include control cell group without any treatment. Presented algorithm is not applicable to non-labelled cell groups. It was the main reason to use the manual tracking only in the part of single-cell migration study.

Currently, cell segmentation, detection and tracking are very important fields in biological research. Different microscopic techniques are used to the cell motility. The most popular are PCM, digital holographic microscopy (DHM), fluorescence microscopy and fluorescent confocal microscopy. Using of PCM and DHM has an advantage in possibility to study non-labelling cells. However, it is primary 2D and pseudo-3D research. Currently, cell tracking is still a great challenge [183]. There are many of new solutions including methods for division cells tracking [184, 185]. Furthermore, to improve the detection of nuclei in microscopic images, in addition to the basic segmentation methods, deep learning algorithms became the state-of-the-art approach for the complete automatic detection of nuclei. Furthermore, in [186], nuclei detection was realized on label-free microscopic images using Convolution Neural Network (CNN).

5.3 CEL LABELLING PROTOCOLS

5.3.1 HOECHST 33342

To prepare a stock solution, dissolve 5 mg of Hoechst 33342 (14533, Sigma-Aldrich) powder in 177 µL of sterile dH_2O to prepare dye in concentration of 50 mM. For cell nuclei staining use the work solution in concentration of 50 µM. For example, dilute 1 µL stock solution dye in 1 mL growth medium. To stain cell nuclei of adherent cells, remove growth medium. Then gently wash cells by PBS and add 50 µM work solution. Move cells to humidified incubator at 37°C for about 15 minutes. After that, remove dye solution and gently wash cells by PBS twice. Then cultivate cells in growth medium. [159]

5.3.2 CALCEIN AM

To prepare a stock solution, dissolve 1 mg of Calcein-AM (17783, Sigma-Aldrich) powder in 100 µL of DMSO to prepare dye in concentration of 10 mM. Before staining, prepare work solution in final concentration of 10 µM. For example, dilute 1 µL stock solution dye in 1 mL growth medium. To stain adherent cells, remove growth medium and gently wash cells by PBS. Then add 10 µM dye solution and incubate it for 15 minutes in humidified incubator at 37°C. Then remove dye solution, gently wash cells by PBS and cultivate it in growth medium. [165]

5.3.3 CELLTRACKER™ GREEN CMFDA DYE AND CELLTRACKER™ RED CMTPX DYE

CMFDA (C7025, Invitrogen) and CMTPX (C34552, Invitrogen) have the same protocol of work solution preparation and cell stain. The dye vial, which contains 50 µg of powder, warm to room temperature and centrifuge at 1000 rpm for 5 minutes. Then dissolve it in 100 µL of Dimethyl sulfoxide (DMSO; PENTA s.r.o.) to make a 1 mM stock solution. Before staining, warm 1 mM stock solution to 37°C and then dilute it to a final concentration of 1 µM in serum free medium. For example, dilute 1 µL dye in 1 mL serum free medium. To stain adherent cells, remove growth medium and gently wash cells by PBS. Then add pre-warmed 1 µM dye solution and incubate for 15 minutes in humidified incubator at 37°C. Then remove dye solution, gently wash cells by PBS and cultivate in growth medium. [167, 168]

5.3.4 RHODAMINE-DERIVED SUPERPARAMAGNETIC MAGHEMITE NANOPARTICLES

SAMN-R (Regional Centre of Advanced Technologies and Materials, Palacký University, Olomouc) suspension was homogenised during 20 minutes using ultrasonic homogeniser (30W, 0.5s/3s pulse) before use. To prepare stained solution, mix SAMN-R in warm growth medium (37°C) at a dose value of 20 $\mu g \cdot cm^{-2}$ [141]. To stain adherent cells, remove growth medium and gently wash cells by PBS. Add the prepared solution to the culture vessel with adherent cells. After 24 hours, remove medium with nanoparticles, wash cells with PBS twice and add fresh growth medium. Method of synthesis and SAMN-R preparation was introduced in [92].

6 STUDY OF RHODAMINE-DERIVED SUPERPARAMAGNETIC MAGHEMITE NANOPARTICLES TOXICITY IN CELL CULTURES

When nanoparticles used to live cells labelling it is necessary to control their dose or concentration to avoid toxic effects on the cells. SAMN-R diluted in the water demonstrate colloidal behaviour within several days [92]. For cell staining it is necessary to dilute this concentrated colloidal solution of nanoparticles in cell culture medium. As seen in Figure 26 nanoparticles form a precipitate (black flecks in bright-field images) in the interaction with cell growth medium. Nevertheless, nanoparticles successfully penetrate into the intracellular environment of cells. In the previous studies [60, 61, 92] SAMN-R were used in concentration of 50 $\mu g \cdot mL^{-1}$. Since the suspension of nanoparticles does not retain a colloidal state in culture medium it was decided to study the dose parameter of nanoparticles in terms of mass per unit area surface of the culture dish ($\mu g \cdot cm^{-2}$). Also, this choice was influenced by the fact that the cell culture flasks, dishes and different scaffolds have a different growth area and required volume of medium.

Human MSCs and 3T3 cells were treated with different concentrations of SAMN-R to study the dose parameter. The analysis was based on an assessment of visible changes in cell morphology. Eight-well chambered cover glasses (Cellvis) were chosen for SAMN-R toxicity test. Suspension of nanoparticles was homogenised during 20 minutes using ultrasonic homogeniser (30W, 0.5s/3s pulse) before use. The glass surface was coated with fibronectin solution (FN; Sigma-Aldrich) in concentration of 1 $\mu g \cdot cm^{-2}$. After subculturing, cells were seeded at a density of $4 \cdot 10^3$ $cells \cdot cm^{-2}$ in each well. When the cell confluence reached 70–80%, then growth medium was removed and fresh growth medium with SAMN-R were added for 24 hours. To find the optimal dose of particles, the following values were selected: 5 $\mu g \cdot cm^{-2}$, 10 $\mu g \cdot cm^{-2}$, 15 $\mu g \cdot cm^{-2}$, 20 $\mu g \cdot cm^{-2}$, 25 $\mu g \cdot cm^{-2}$, 30 $\mu g \cdot cm^{-2}$ and 35 $\mu g \cdot cm^{-2}$. One of the wells was without nanoparticles treating for control. On the next day, medium with nanoparticles was removed, cells were washed with PBS and fresh growth medium were added. Then cell morphology was controlled using a confocal microscope. Representative results are shown in Figure 26.

A dose of nanoparticles in value of 30 $\mu g \cdot cm^{-2}$ were identified to be toxic because of the appearance of a large number of necrotic cells (Figure 26). When using nanoparticles at a dose level of 25 $\mu g \cdot cm^{-2}$ the visible changes in cell morphology were observed – there were areas where cell adhesion was impaired. This effect was observed only in 3T3 cell samples. There were no visible changes in hMSCs samples, but a large amount of precipitate was observed. The use of this dose is not recommended, since the structure of some cells is not visible and it is difficult to determine the result of the nanoparticle influence. A dose of 20 $\mu g \cdot cm^{-2}$ was determined to be safe and was used in following studies. In this work cells were treated with SAMN-R during 24 hours. Thereafter, they were washed with PBS before adding the fresh growth medium. This step in the cell stain protocol helps to remove a significant part of the nanoparticle clusters.

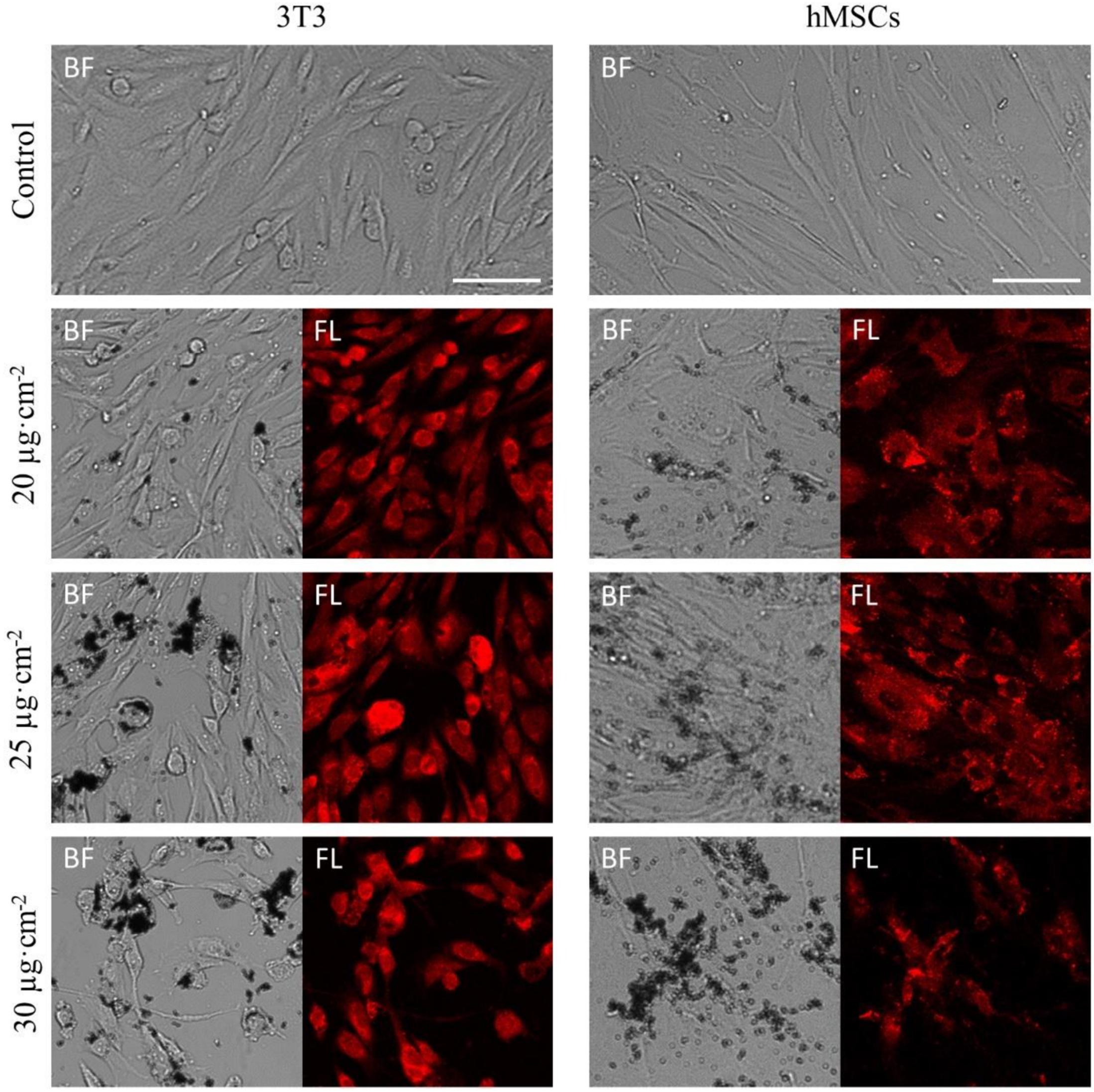

Figure 26. Influence of rhodamine-derived superparamagnetic maghemite nanoparticles (SAMN-R) at a dose level of 20 μg·cm^{-2}, 25 μg·cm^{-2} and 30 μg·cm^{-2} on 3T3 (left) and hMSCs (right) cell morphology. The images on top represent the samples without nanoparticle treatment (control). Confocal microscopy, bright-field channel (BF), fluorescence channel (FL) 10× magnification, scale bar 100 μm.

The dose value has been determined by non-quantitative measurement using bright-field and fluorescence microscopy. This method was used to determine the approximate dose of nanoparticles that can be suitable for labelling living cells.

6.1 REACTIVE OXYGEN SPECIES

Nanoparticles influence the generation of ROS, that is the main factor of their toxic effect. ROS is an important factor connected with the beginning of cell stress and the developing of pathological cell changes. ROS production by hMSCs and 3T3 cells treated with SAMN-R was determined by fluorescent ROS probe CM-H2DCFDA (C6827, Invitrogen). Human MSCs and 3T3 cells were seeded on 96-well plate in density of $5 \cdot 10^3$ cells·cm^{-2}. At the next day growth medium was removed and fresh growth medium with SAMN-R were added for 24 hours on some wells. There were control wells without treatment and tested wells treated with 10 μg·mL^{-1}, 50 μg·mL^{-1} and 100 μg·mL^{-1} of SAMN-R. Then, cells were stained during 45 min with CM-H2DCFDA in final concentration of 10 μM·L^{-1} in Hank's balanced salt solution (HBSS). After that, the fluorescent signal from each well was measured using an Infinite PRO M200 microplate reader (Tecan, Austria). The excitation wavelength was set on 505 nm and emission wavelength was set on 529 nm. The intensity of treated cells with SAMN-R was compared with intensity of cells without treatment (control samples). This experiment was performed three times. In Figure 27 graphical overview of measured ROS values is shown.

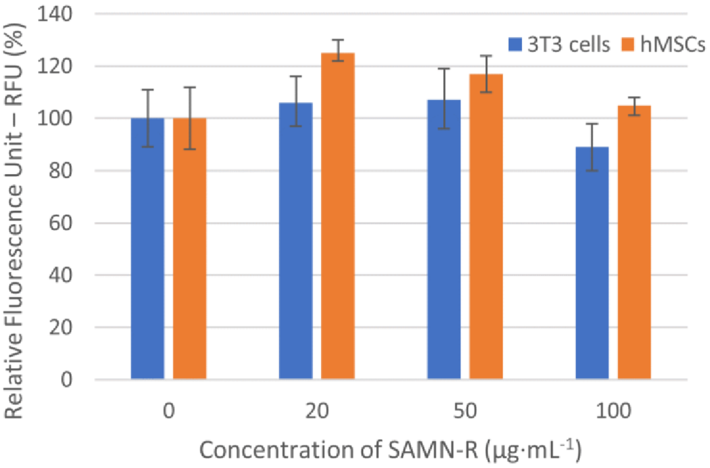

Figure 27. Measurement of reactive oxygen species (ROS) using CM-H2DCFDA fluorescent probe. The intensity of CM-H2DCFDA from samples of hMSCs and 3T3 cells treated with SAMN-R in a concentration of 20 μg·mL^{-1}, 50 μg·mL^{-1} and 100 μg·mL^{-1} in compare with control samples without treatment. The horizontal segment (whiskers) marks the standard deviation of fluorescence intensity.

In order to determine if SAMN-R treatment affects ROS changes, statistical analysis was performed (using the MATLAB software). Using Shapiro-Wilk test [179] it was determined whether the values in the groups are normally distributed. The null hypothesis states that the values of compared groups are normally distributed. P-value in all groups is greater than 0.05 (marked in bold in the Table 3), therefore it was confirmed that the values in all groups are normally distributed. Then, the Bartlett's test for homogeneity of variances was used to test whether variances are equal [187]. The null hypothesis states that the variances of all compared groups are equal. Calculated p-values are greater than 0.05 (marked in bold in the Table 3), therefore a null hypothesis was not rejected. Thus, the conditions for the ANOVA test were confirmed [180]. ANOVA test was used to compare the means of ROS values from cells treated with SAMN-R in different concentrations. The null hypothesis states that the means of ROS values in all groups are equal. The values from treated 3T3 cells were compared, p-value was greater than 0.05 (marked in bold in the Table 3), therefore a null hypothesis was accepted. Thus, the distinction between compared data sets is considered as not statistically significant. It can be assumed that SAMN-R in studied concentrations do not have a significant effect on ROS in 3T3 cells. However, the result of this test applied on the ROS values from hMSCs is not the same. P-value from this data set is less than 0.05 significance level (see values in regular type in the Table 3). It means, that the mean value of ROS for at least one concentration is different. It can be assumed that at least one concentration of SAMN-R can have a significant effect on ROS in hMSC cells. Therefore, it was decided to use post-hoc Tukey HSD (Honestly Significant Difference) statistical test to compare values from all groups separately [180]. The null hypothesis states that the means of two compared groups are equal. It was confirmed that there is difference between means of ROS values from control group and hMSCs treated with SAMN-R in a concentration 20 $\mu g \cdot mL^{-1}$. P-value from this data set is less than 0.05 significance level (see values in regular type in the Table 4). The results show that some concentrations of SAMN-R can affect ROS production. Nevertheless, more test experiments are needed to study the toxic effect of nanoparticles on living cells. According to the working volume (200 µL) of growth medium and growth area of 96-well plate (0.32 cm^2), concentration of tested SAMN-R in this experiment of 20 $\mu g \cdot mL^{-1}$ corresponds to 12.5 $\mu g \cdot cm^{-2}$, 50 $\mu g \cdot mL^{-1}$ corresponds to 31.25 $\mu g \cdot cm^{-2}$ and 100 $\mu g \cdot mL^{-1}$ corresponds to 62.5 $\mu g \cdot cm^{-2}$. In the following experiments in this work the dose value of 20 $\mu g \cdot cm^{-2}$ was used. This value is the intermediate value among the tested values.

Table 3. Statistical tests applied on values of ROS production by hMSCs and 3T3 cells treated with SAMN-R in different concentrations. Table of p-values from Shapiro-Wilk test, Bartlett's test and ANOVA. P-values greater than 0.05 marked in bold (null hypothesis is accepted).

Cell line	Group with different concentration of SAMN-R	Statistical test		
		Shapiro-Wilk (p-value)	Bartlett's test (p-value)	ANOVA (p-value)
3T3 cells	Control	**0.9082**	**0.9782**	**0.2059**
	20 $\mu g \cdot mL^{-1}$	**0.9420**		
	50 $\mu g \cdot mL^{-1}$	**0.9521**		
	100 $\mu g \cdot mL^{-1}$	**1.0000**		
hMSCs	Control	**0.9559**	**0.3401**	0.0163
	20 $\mu g \cdot mL^{-1}$	**0.7262**		
	50 $\mu g \cdot mL^{-1}$	**1.0000**		
	100 $\mu g \cdot mL^{-1}$	**0.8428**		

Table 4. Statistical tests applied on values of ROS production by hMSCs cells treated with SAMN-R in different concentrations. Table of p-values from post-hoc Tukey HSD test. P-values greater than 0.05 marked in bold (null hypothesis is accepted).

Compared groups with different concentration of SAMN-R	Control / 20 $\mu g \cdot mL^{-1}$	Control / 50 $\mu g \cdot mL^{-1}$	Control / 100 $\mu g \cdot mL^{-1}$	20 $\mu g \cdot mL^{-1}$/ 50 $\mu g \cdot mL^{-1}$	20 $\mu g \cdot mL^{-1}$/ 100 $\mu g \cdot mL^{-1}$	50 $\mu g \cdot mL^{-1}$/ 100 $\mu g \cdot mL^{-1}$
Tukey HSD statistical test (p-value)	0.0178	**0.0913**	**0.7835**	**0.6470**	**0.0627**	**0.3124**

6.2 STUDY OF THE CELL PROLIFERATION

The toxicity analysis is often based on the detection of live/dead cells. It can be performed using cell dyes as Trypan blue, Propidium iodide, Calcein-AM, Ethidium homodimer-1, etc. A decrease in the number of living cells changes a cell growth curve. Thus, the toxic effect of the different chemicals can be studied using the cell growth curve. In this work the study of the possible influence of SAMN-R on the cell proliferation was carried out using a cell growth curve. This study was performed on the 3T3 cells. Two types of nanoparticle application have been tested: treating with nanoparticles before (Figure 28 (B)) or after subculturing (Figure 28 (A)).

At first the method of treating cells with nanoparticles after cell subculturing was studied. To test this type of nanoparticle application the 3T3 cells were seeded on two 8-well chambered FN-coated cover glasses (Celvis) at a density of $4 \cdot 10^3$ cells$\cdot$cm^{-2}. After 18 hours cell were controlled and three wells on each cover glasses were treated with SAMN-R in a dose of 20 μg$\cdot$cm^{-2}. Then nuclei of the cells in two nontreated wells were stained by Hoechst 33342 and Calcein-AM. Then fluorescent images were acquired by confocal microscope. After six hours cells treated with nanoparticles were washed with PBS (24 hours after cell seeding) and then culture medium was added. Then cell nuclei on two nontreated wells and two wells treated with nanoparticles were staining after 24, 48, 72 hours after seeding. After image acquisition ten staggered fields of view in the middle of the wells were selected. On these images the cell count was determined by counting the nuclei stained with Hoechst 33342. For cell nuclei segmentation and semi-automatic determination of number of cells a custom-made algorithm in MATLAB software was used (chapter 5.2.3). The obtained cell growth curve is shown in Figure 28 (A). For cell viability and confluency control (data not shown) [176], cells on the wells prepared to image acquisition were stained with Calcein-AM. Experiments were repeated three times.

In the first method the cells were treated with nanoparticles during six hours. In the study [91], treated cells were controlled after two, seven and 24 hours. After seven hours a good fluorescence signal was detected. During this time, a lot of particles penetrated intracellular compartment of the cells [96, 188], which also was confirmed by many observations (data not shown). Nevertheless, the effect of long-term nanoparticle treating (24–48 hours) was of interest in many types of experiments [58–61, 91]. It was decided to treat cells with nanoparticles during 24 hours in the second type of the experiment and in all subsequent experiments to comply with the same conditions. In turn, the use of fluorescent markers has a widespread use for automatically cell segmentation [189–191]. For this reason, the CellTracker™ Green CMFDA was tested for comparison with SAMN-R. This choice was made because this dye is a low toxic and suitable for long-term experiments.

To test the effect of fluorescent markers application before cell seeding the 3T3 cells were seeded on three wells of 24-well plate (growth area per well: 1.9 cm^2; Sigma-Aldrich s.r.o.). When cell confluency reached 80–90%, then cells on the first well were treated with SAMN-R, on the second well were stained with CMFDA. The third well was the control sample without influence. After 24 hours cells were washed with PBS and subcultured. Then each cell type were seeded in eight wells on three 8-well chambered FN-coated cover glasses (Celvis) at a density of $4\cdot10^3$ cells·cm^{-2}. After 24, 48, and 72 hours, two wells from each type were stained with Hoechst 33342 and then fluorescent images were acquired by confocal microscope. The same algorithm as in the first type of experiments was used for cell count. Experiments were repeated three times. The obtained cell growth curve is shown in Figure 28 (B).

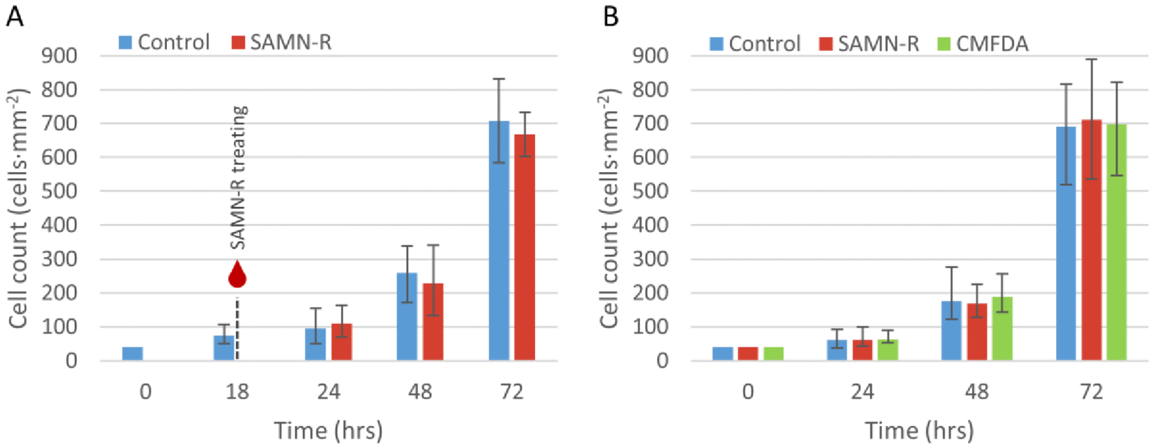

Figure 28. Cell growth curve of 3T3 cells. Each column represents the number of cells in an area of 1 mm^2 from ten field of view by three groups of samples: control cells without treatment (blue), treated with rhodamine-derived superparamagnetic maghemite nanoparticles (red), stained with CellTracker™ Green CMFDA Dye (green).

Statistical analysis was performed to identify the effect of SANM-R and CMFDA labelling on cell proliferation. Initially, it was determined whether the values in the groups are normally distributed. It was evaluated using Shapiro-Wilk test [179]. The null hypothesis states that the values of compared groups are normally distributed. P-value in all groups is greater than 0.05. Thus, it was confirmed that the values in all groups are normally distributed (marked in bold in the Table 5, Table 6). Then, the F-test [180] was used to compare the variances of two data sets from the first graph (Figure 28 (A)) and to compare three data sets with each other from the second graph (Figure 28 (B)). The null hypothesis states that the variances of compared groups are equal. All p-values are greater than 0.05 (marked in bold in the Table 5, Table 7), therefore a null hypothesis was accepted. The variances of compared data sets in the first (non-labelled cells and SAMN-R-treated cells) and second graph (non-labelled cells, SAMN-R-treated cells and cells stained with CMFDA) are equal. Also, T-test was used to compare the means of data sets from the first graph (Figure 28 (A)) and ANOVA test was used to compare the means of data sets from the second graph (Figure 28 (B)) [180]. The null hypothesis states that the means of two groups are equal. All p-values are greater than 0.05 (marked in bold in the Table 5, Table 6), therefore a null hypothesis was accepted. The results of this test show that the distinction between compared data sets is considered as not statistically significant. It can be assumed that SAMN-R and CMFDA do not have a significant effect on cell proliferation. The MATLAB software was used to perform statistical analysis.

Table 5. Statistical tests applied on values of cell nuclei count in different time from cell growth curve of 3T3 cells (first method). Table of p-values from Shapiro-Wilk test, F-test, and T-test. P-values greater than 0.05 marked in bold (null hypothesis is accepted).

Time (hours)	Group	Statistical test		
		Shapiro-Wilk (p-value)	F-test (p-value)	T-test (p-value)
24	Control	**0.2525**	**0.4050**	**0.1324**
	SAMN-R	**0.7444**		
48	Control	**0.8299**	**0.5709**	**0.0657**
	SAMN-R	**0.4136**		
72	Control	**0.4288**	**0.8710**	**0.8281**
	SAMN-R	**0.6116**		

Table 6. Statistical tests applied on values of cell nuclei count in different time from cell growth curve of 3T3 cells (second method). Table of p-values from Shapiro-Wilk test and ANOVA statistical tests. P-values greater than 0.05 marked in bold (null hypothesis is accepted).

Time (hours)	Group	Statistical test	
		Shapiro-Wilk (p-value)	ANOVA (p-value)
24	Control	**0.7270**	**0.8692**
	SAMN-R	**0.6063**	
	CMFDA	**0.3699**	
48	Control	**0.0532**	**0.6003**
	SAMN-R	**0.0738**	
	CMFDA	**0.9685**	
72	Control	**0.3564**	**0.9173**
	SAMN-R	**0.6275**	
	CMFDA	**0.7840**	

Table 7. Statistical tests applied on values of cell nuclei count in different time from cell growth curve of 3T3 cells (second method). Table of p-values from F-test. P-values greater than 0.05 marked in bold (null hypothesis is accepted).

		F-test (p-value)		
		Time (hours)		
Compared groups		24	48	72
Control	SAMN-R	**0.4773**	**0.1146**	**0.3351**
Control	CMFDA	**0.1411**	**0.0834**	**0.4547**
SAMN-R	CMFDA	**0.1292**	**0.4251**	**0.2950**

6.3 DISCUSSION

Nanoparticles are of great interest in biological research because they can be used for cell marking and drug delivery. Their widespread use is due to unique properties such as their biocompatibility, biodegradability, and ability to penetrate cells [56, 57, 192]. Nanoparticles are a promising material that is suitable for *in vitro* research in the field of regenerative medicine and therapy, but many studies have shown that they exert a toxic effect on living cells. The interactions between nanoparticles and cell membranes are affected by their material, size, surface compound, and charge [96, 101, 105]. SPION are currently very popular and have yielded successful results in many fields of research. In the first studies they have mainly been used for MRI [45, 46, 82, 83], but the discovery of new characteristics has expanded their application to tumour and cancer therapy, hyperthermia therapy, and cardiovascular research, among other fields [45, 47–53].

In recent research, different organic and inorganic coatings have been used for the functionalization of nanoparticles including polymers, lipids, peptides, proteins, drugs, silica, carbon, metals, and oxides [55, 56, 192]. SAMN-R are functionalized with Rhodamine B isothiocyanate fluorescent dye and therefore SAMN-R-treated cells can be detected by means of fluorescence microscopy. For this reason, they are used for cell marking in, for example, tissue engineering [36, 42], but coatings can lead to surface charges and influence interactions with the cell membrane [96, 105], which can also affect their toxicity.

Recent studies have revealed that nanoparticles such as SPION affect ROS production [106–108]. ROS are normally generated during metabolic reactions, but their production can also be influenced by physical or chemical exposure. Changing ROS production (either by increasing or decreasing it) can lead to the damage of macromolecules such as DNA, proteins, and lipids, and therefore cell treatment with nanoparticles can promote a toxic effect. It is very important to measure changes in ROS production at the beginning of *in vitro* studies to exclude concentrations that have a damaging effect on living cells. In this work, three concentrations of SAMN-R ($20\ \mu g\cdot mL^{-1}$, $50\ \mu g\cdot mL^{-1}$, and $100\ \mu g\cdot mL^{-1}$) are tested, after which a statistical analysis confirmed that significant changes in ROS production occur in hMSCs treated with SAMN-R in a concentration of $20\ \mu g\cdot mL^{-1}$. It should be noted that due to limited access to the necessary equipment, only three measurements were performed for this study.

Iron oxide nanoparticles form clusters in the cell growth medium because of the zeta-potential changes [96]; they do not retain their colloidal stability in this environment, thus form sediment in culture vessels. A large number of sizeable clusters can exert a damaging effect on cell membranes [105, 193] and, for cell treatment in *in vitro* experiments, it is usually necessary to mix nanoparticles in the cell growth medium. It was decided that for this study, it was more appropriate to research the concentration of nanoparticles in a per-surface-area unit in order to determine what dose of SAMN-R would not have a toxic effect on living cells. The first test was performed based on observations of changes in cell morphology (Chapter 6), which helped to define a tentative dose suitable for marking living cells. A dose of 20 $\mu g \cdot cm^{-2}$ was determined to be safe, but it was first necessary to test for possible toxic effects *via* quantitative methods.

There are several methods of testing the toxic effects of chemicals on living cells [108], but some of the most common methods of testing the effects of nanoparticle treatment are inappropriate or difficult to follow. For example, for lactate dehydrogenase assay and flow cytometry, cells are prepared in suspension, so must be used after passage, but when cells are marked with SAMN-R nanoparticles, they are treated within 24 hours, indicating that control and treated samples may be affected by differences in passage conditions. The MTT (3-[4,5-dimethylthiazol-2-yl]-2,5 diphenyl tetrazolium bromide) assay is another widely used assay employed to determine cell viability by examining mitochondrial activity. Here, adherent cells are stained with special dyes and measurements are performed by quantifying the amount of light absorbance at a specific wavelength. The number and functional viability of cells can be measured by their absorbance value, but the SAMN-R nanoparticles form a sediment at the bottom of the culture vessel or the cells' surface, which distorts the absorption value. Because it is difficult to prepare a control sample for this assay, in this work, cell growth curves were described by counting cells at different time points. The number of cells was determined using a custom-made algorithm based on counting the number of nuclei stained with fluorescent dye (Chapter 5.2.3). In one part of the experiment, the cells were also stained with Calcein-AM to control cell viability. In the other part the effect of SAMN-R treatment and CMFDA staining on cells was studied. The subsequent statistical analysis did not confirm the assumed significant difference between the proliferation of the treated and the control cells.

Previous studies have used TEM and SEM microscopy to confirm that SAMN-R are mainly found in lysosomes [58, 59]. In study [61], a team from our department confirmed the absence of SAMN-R in mitochondria using confocal fluorescence microscopy, and this work has also observed their absence in cell nuclei following a colocalization analysis (chapter 5.1). Despite this, there is a risk of a cytotoxic effect when the cellular uptake of nanoparticles takes place at high concentrations, which can lead to damage to the lysosomal membrane [105]. This contributes to the leakage of metal ions and nanoparticles to the cytoplasm, can cause changes in ROS production, and promotes the penetration of nanoparticles from the cytoplasm into the nucleus during mitosis.

In the first studies conducted, the toxicity of SAMN-R was tested using the available methods and, based on the results, a dose value of 20 $\mu g \cdot cm^{-2}$ can be said to have no damaging effect on living cells or on cell proliferation.

7 STUDY OF MIGRATION OF CELLS TREATED WITH RHODAMINE-DERIVED SUPERPARAMAGNETIC MAGHEMITE NANOPARTICLES

7.1 COLLECTIVE CELL MIGRATION STUDY USING SCRATCH ASSAY METHOD

The scratch assay (or wound healing assay) is a simple widespread method for the analysis of 2D cell migration [133]. This method is often used to study the effect of treatment on cell migration [194–196]. In this work, CMFDA fluorescent dye and SAMN-R nanoparticles cytotoxicity was studied by scratch assay. This analysis was performed on the 3T3 cells. Fibroblasts play a crucial role in the processes of tissue repair and regeneration. The desire of cells to heal an artificial wound in this case is a natural process. Collective migration research can help determine the effect of the treatments on the vital functions of the cell.

Typically, cells form cellular protrusions, as filopodia, lamellipodia and blebs, for the ability to move and migrate [197]. Filopodia and lamellipodia (Figure 8), which is driven by actin polymerization, have an important role in this process. Lamellipodia and blebs provide a displacement of the cytoplasm in the direction of migration, thereby moving the cells forward. They attach to the surface on which they move using adhesion plaques – mainly transmembrane integrins. Usually, growth cell medium is supplemented with FBS includes vitronectin (VN), which mediates cell adhesion to glass and polystyrene surfaces of culture vessels. VN can simply adsorb onto these types of surfaces. Then transmembrane integrins bind to VN. Often, different coatings are used to increase adhesive strength. For example, ECMs such as FN and collagen that can adsorb on the surfaces of culture vessels. They are involved as attachment proteins that create bindings with transmembrane integrins. Usually, coating is used to improve cell adhesion and to bring *in vitro* experiments closer to *in vivo* conditions. The coating enhances cell adhesion so that the confluent cell monolayer is not disturbed at the scratch boundaries. [152]

In long-term experiments, it is important to observe the same area at different time intervals. One solution is to use culture dishes with a grid on the bottom. This modification is suitable for scratch assay experiments where the observed area is controlled in several long-time intervals. This method was used in this work. The grid was marked with a marker on the outside of the dish bottom. Commercial culture dishes with a scribbled grid are an alternative. A disadvantage of this option is the non-smoothness of the surface because of the engraved grid cavities, which is an excessive factor affecting cell adhesion. Depending on the microscopic technique used, these options may not be suitable. For example, with the use of bright field microscopy or contrast methods as PCM, IMC, DIC, because the grid may be visible in the field of view and thus prevent further processing of the obtained images. When using fluorescence microscopy, the grid is less visible.

The collective 3T3 cells migration was studied by a scratch assay. For each experiment the three groups of cells were prepared: control group without staining, treated with SAMN-R, staining with CMFDA dye. Samples were prepared according to the protocol provided below.

Cell were seeded on three FN-coated culture dishes (TPP Techno Plastic Products AG) with a growth area of 9.2 cm^2. Before seeding a grid were marked on the outer bottom of the dish. This was necessary to obtain the same field of view during the image acquisition. When cell confluency reached 75–80% then one of the dishes was treated with SAMN-R within 24 hours and the second dish was stained with CMFDA. At the next day cell confluency reached 100%. Cells were washed with PBS and growth culture medium were exchanged. Then scratches (gaps) were made with p200 pipette tip at the dishes bottom. Medium with detached cells were removed. Cells were gently washed with PBS and dishes were filled by 3 ml of fresh growth medium. Then the images of the scratch areas were acquired by confocal microscope. After 24 and 48 hours the images from the same areas were obtained. These areas have been found since the grid was marked at the bottom. The experiment was repeated ten times and images from 60 field of view of each group were obtained. Areas with a narrow and with a wide scratch were considered separately (Figure 29). These results were introduced in [141].

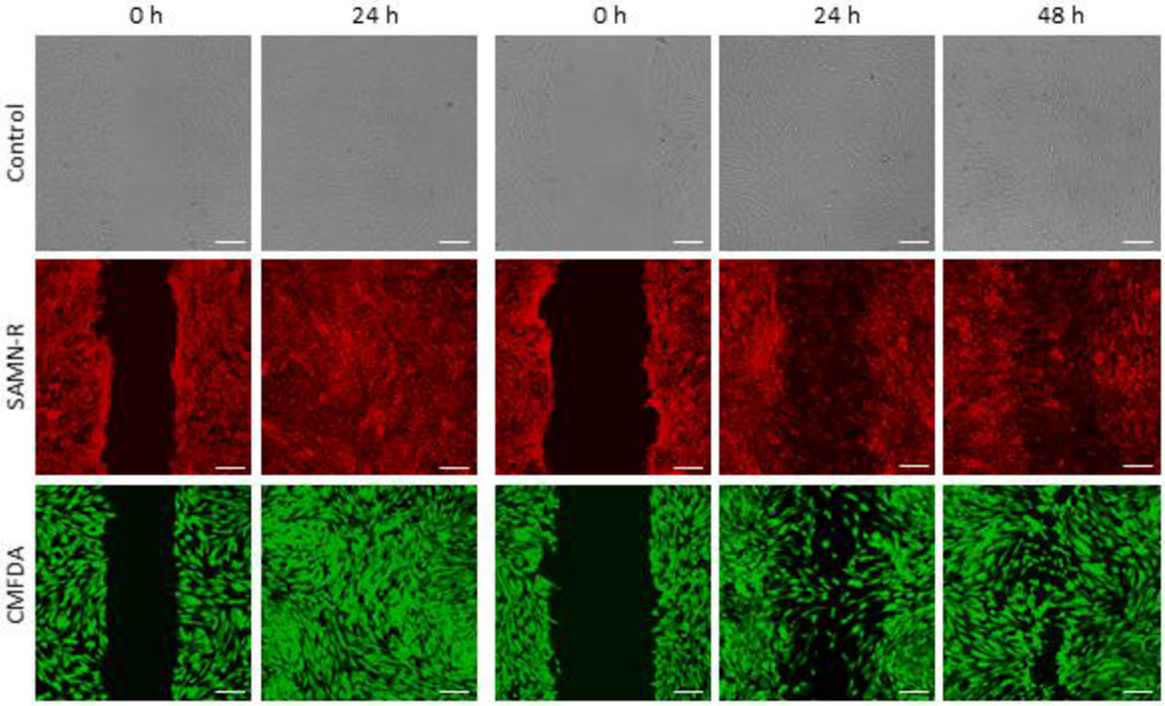

Figure 29. Scratch assay applied to 3T3 cells: non-labelled (control), treated with rhodamine-derived superparamagnetic maghemite nanoparticles (SAMN-R), and stained with CellTracker™ Green CMFDA Dye (CMFDA). Images were detected at the beginning and after 24 and 48 hours. The white line marks the initial scratch border. Confocal microscopy, 10× magnification, scale bar 150 µm.

The scratch assay analysis was based on calculating the open area present at the scratch area. The acquired images from bright-field and fluorescence channel were analysed by a custom algorithm using MATLAB software (Chapter 5.2.2). The scratch width and area from each obtained image were determined.

As can be seen from the data in Table 8 and Table 9, the areas with a narrow scratch were overgrown within approximately 24 hours, and the areas with a wide scratch were overgrown within 48 hours.

Table 8. Size values of the open area of narrow scratch in the scratch assay experiment.

Item	Time (hours)	Control			SAMN-R			CMFDA		
		Min	Max	Mean	Min	Max	Mean	Min	Max	Mean
Scratch width (µm)	0	311.54	493.62	408.01	325.04	477.73	416.44	329.51	491.50	427.76
Scratch area (mm^2)	0	0.36	0.58	0.48	0.38	0.56	0.49	0.38	0.57	0.50
	24	0.00	0.02	0.00	0.00	0.02	0.00	0.00	0.02	0.00

Table 9. Size values of the open area of wide scratch in the scratch assay experiment.

Item	Time (hours)	Control			SAMN-R			CMFDA		
		Min	Max	Mean	Min	Max	Mean	Min	Max	Mean
Scratch width (µm)	0	502.18	689.57	554.24	438.18	711.15	548.73	447.23	621.20	541.37
Scratch area (mm^2)	0	0.59	0.80	0.65	0.51	0.83	0.64	0.52	0.73	0.63
	24	0.17	0.53	0.31	0.14	0.57	0.32	0.16	0.56	0.36
	48	0.00	0.09	0.03	0.00	0.05	0.02	0.00	0.23	0.03

Time-dependent changes in the open area due to 3T3 cell migration are shown in Figure 30 (A, B). The effect of SANM-R and CMFDA labelling on collective cell migration in scratch assay was studied by statistical analysis performed in MATLAB software. Using the Shapiro-Wilk test [179], the normal data distribution was not confirmed in the majority of groups (see values in regular type in the Table 10. Therefore, the Kruskal-Wallis nonparametric test [180] was used to determine whether any of the differences between the medians of non-labelled, SAMN-R treated and CMFDA stained groups are statistically significant (Table 10).

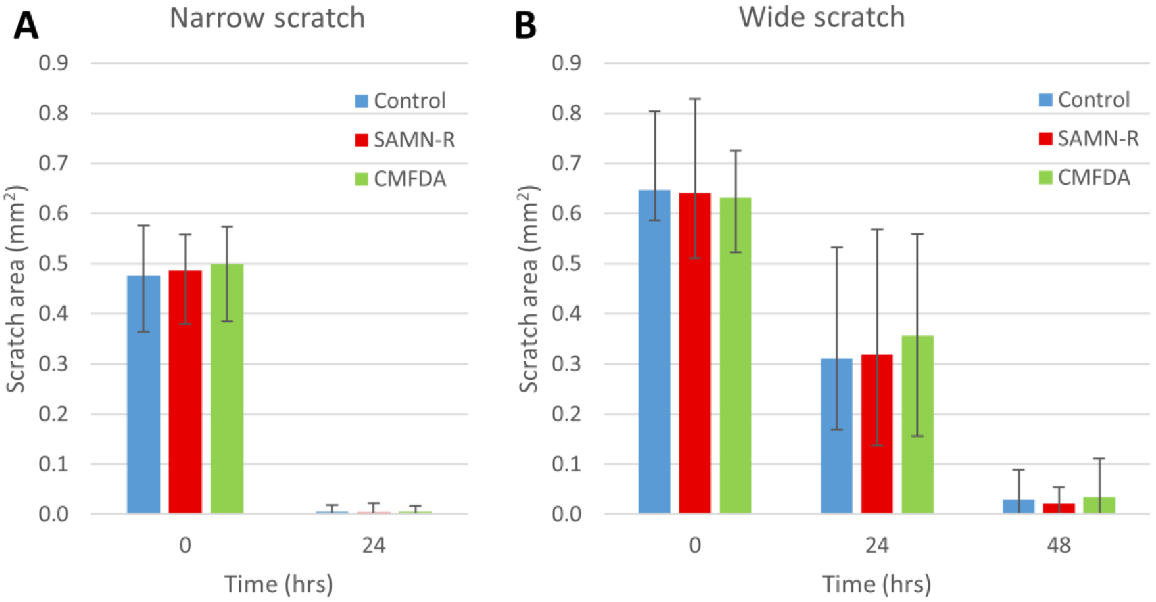

Figure 30. Time-dependent changes in the size of the open area due to 3T3 cell migration in (A) narrow scratch and in (B) wide scratch. Each column represents scratch areas in 30 images in each group of samples: control cells without treatment (blue), treatment with rhodamine-derived superparamagnetic maghemite nanoparticles (red), stained with CellTracker™ Green CMFDA Dye (green).

Table 10. Statistical tests applied on values of the open area in different time from narrow and wide scratch. Table of p-values from Shapiro-Wilk and Kruskal-Wallis statistical tests. P-values greater than 0.05 marked in bold (null hypothesis is accepted).

Scratch	Time (hours)	Group	Statistical test	
			Shapiro-Wilk (p-value)	Kruskal-Wallis (p value)
Narrow	0	Control	**0.2288**	**0.2609**
		SAMN-R	0.0431	
		CMFDA	**0.0546**	
	24	Control	0.0110	**0.5274**
		SAMN-R	0.0004	
		CMFDA	0.0010	
Wide	0	Control	0.0106	**0.5887**
		SAMN-R	**0.9569**	
		CMFDA	**0.2920**	
	24	Control	**0.1862**	**0.2642**
		SAMN-R	**0.2089**	
		CMFDA	**0.1583**	
	48	Control	**0.2518**	**0.3579**
		SAMN-R	0.0029	
		CMFDA	0.0049	

The null hypothesis states that the medians of compared groups are equal. When the p-value exceed 0.05 (marked in bold in the Table 10), then the differences between the medians are not statistically significant. This test was applied on data sets in different time intervals. The null hypothesis was accepted in all tested groups.

Then the difference between each group in different time intervals was calculated separately using Tukey-Kramer post hoc test (Table 11) [181]. This test compares the means of tested groups, whether they are equal. The null hypothesis states that the means of two groups are equal. When the p-value is greater than 0.05 (marked in bold in the Table 11), then we can accept the null hypothesis.

Table 11. Statistical tests applied on values of the open area in different time from narrow and wide scratch. Table of p-values from Tukey-Kramer statistical tests. P-values greater than 0.05 marked in bold (null hypothesis is accepted).

		Turkey-Kramer (p-value)				
		Narrow scratch		Wide scratch		
		Time (hours)		Time (hours)		
Compared groups		0	24	0	24	48
Control	SAMN-R	**0.8923**	**0.5052**	**0.5615**	**0.9464**	**0.4923**
Control	CMFDA	**0.2494**	**0.7453**	**0.8196**	**0.2703**	**0.3826**
SAMN-R	CMFDA	**0.4915**	**0.9245**	**0.9000**	**0.4366**	**0.9740**

The significant differences between medians of non-labelled, SAMN-R treated and CMFDA stained groups were not found. The statistical Kruskal-Wallis test and Tukey-Kramer test showed that SAMN-R and CMFDA did not have a significant effect on collective cell migration.

7.2 SINGLE-CELL MIGRATION STUDY

Single-cell migration of hMSCs was studied to determine the effect of SAMN-R treatment on cell motility. One set of experiments consist of three groups of samples: control cells without treatment, treated with SAMN-R, stained with CMFDA fluorescent dye.

After passage cells were seeded on three 35 mm glass-bottom dishes (14 mm well size, Cellvis) at a density of $3 \cdot 10^3$ cells·cm^{-2}. At the next day cells on the one of the dishes were stained with CMFDA dye and cells on the second dish were treated with SAMN-R during 24 hours. A third dish was used as control sample. Cells were gently washed with PBS and fresh growth medium was added one hour before the image acquisition. An experiment with control sample was performed first. When this experiment was finished, an experiment with a CMFDA-stained sample was performed. A third sample was tested after 24 hours of nanoparticle treatment.

Cells were observed by confocal microscope (Leica TCS SP8 X) in long-term mode. The atmosphere of 5% CO_2 and 37°C temperature was maintained during the entire time of experiment using a microscope incubator (The Stage Top Chamber, OKOLAB). The objective with magnification of 10× was used. Experiment was setting for six hours. During this time the image of field of view (1.16 × 1.16 mm) was acquired with intervals of five minutes. Images were obtained with a resolution of 1024 × 1024 pixels and a 100 Hz scan speed and bidirectional scanning (double the speed). In the first experiment (Patient 1) only one field of view was observed. In the next experiments (Patients 2–4) several fields of view (Table 21) were selected with help of multi-view mode (mark and find function). Images from the selected fields of view were obtained one after another with the specified intervals.

In the obtained image sequences, it was necessary to select cells for migration tracking. The cells that do not remain in the field of view or divided during observed time were not chosen. Number of the cells in each study groups was the same (18, 20, 50, 50 cells from four patients respectively). For cell detection in image sequences manual tracking plugin by ImageJ [198, 199] was used. Then data of cell distribution were analysed by a custom algorithm using MATLAB software. Obtained coordinates were used for calculating value of velocity, accumulated distance and Euclidean distance of migrated cells. The data were normalized by converting pixels to micrometres (pxl size = 1.13 µm). The calculated values are listed in Table 12–Table 15. Rose plots of cell migration tracks from Patient 1–4 are in Figure 31. Tracks shown are from non-labelled, SAMN-R treated and CMFDA stained hMSCs. The starting points of each cell were set to origin of coordinates. These results were introduced in [141].

Table 12. Migration of hMSCs in Patient 1 from 18 cells of control, CellTracker™ Green CMFDA (CMFDA) labelled, and rhodamine-derived superparamagnetic maghemite nanoparticles (SAMN-R) treatment groups. The velocity, accumulated, and Euclidean distance values for a six-hour period are shown. [141]

	Control			SAMN-R			CMFDA		
Item	Min	Max	Mean	Min	Max	Mean	Min	Max	Mean
Accumulated distance (µm)	62.76	271.85	153.99	86.36	241.65	148.85	73.92	200.72	136.97
Euclidean distance (µm)	10.23	217.19	81.90	8.83	123.17	55.36	7.91	97.74	41.92
Velocity (µm/min)	0.17	0.76	0.43	0.24	0.67	0.41	0.21	0.56	0.38

Table 13. Migration of hMSCs in Patient 2 from 20 cells of control, CellTracker™ Green CMFDA (CMFDA) labelled, and rhodamine-derived superparamagnetic maghemite nanoparticles (SAMN-R) treatment groups. The velocity, accumulated, and Euclidean distance values for a six-hour period are shown. [141]

	Control			SAMN-R			CMFDA		
Item	Min	Max	Mean	Min	Max	Mean	Min	Max	Mean
Accumulated distance (µm)	32.82	294.80	104.90	44.64	362.05	118.83	51.73	221.71	114.01
Euclidean distance (µm)	7.24	248.21	69.32	6.87	316.28	80.86	12.22	194.51	82.98
Velocity (µm/min)	0.09	0.82	0.29	0.12	1.01	0.33	0.14	0.62	0.32

Table 14. Migration of hMSCs in Patient 3 from 50 cells of control, CellTracker™ Green CMFDA (CMFDA) labelled, and rhodamine-derived superparamagnetic maghemite nanoparticles (SAMN-R) treatment groups. The velocity, accumulated, and Euclidean distance values for a six-hour period are shown. [141]

	Control			SAMN-R			CMFDA		
Item	Min	Max	Mean	Min	Max	Mean	Min	Max	Mean
Accumulated distance (µm)	48.06	288.48	156.00	45.15	270.70	143.62	43.02	282.62	154.66
Euclidean distance (µm)	9.72	190.26	65.91	15.74	226.10	99.33	2.26	193.26	68.11
Velocity (µm/min)	0.13	0.80	0.43	0.13	0.75	0.40	0.12	0.79	0.43

Table 15. Migration of hMSCs in Patient 4 from 50 cells of control, CellTracker™ Green CMFDA (CMFDA) labelled, and rhodamine-derived superparamagnetic maghemite nanoparticles (SAMN-R) treatment groups. The velocity, accumulated, and Euclidean distance values for a six-hour period are shown. [141]

	Control			SAMN-R			CMFDA		
Item	Min	Max	Mean	Min	Max	Mean	Min	Max	Mean
Accumulated distance (µm)	33.29	179.74	90.96	30.09	181.34	84.78	37.08	263.26	79.96
Euclidean distance (µm)	9.71	147.88	61.31	8.03	102.06	40.66	3.41	243.35	42.51
Velocity (µm/min)	0.09	0.50	0.25	0.08	0.50	0.24	0.10	0.73	0.22

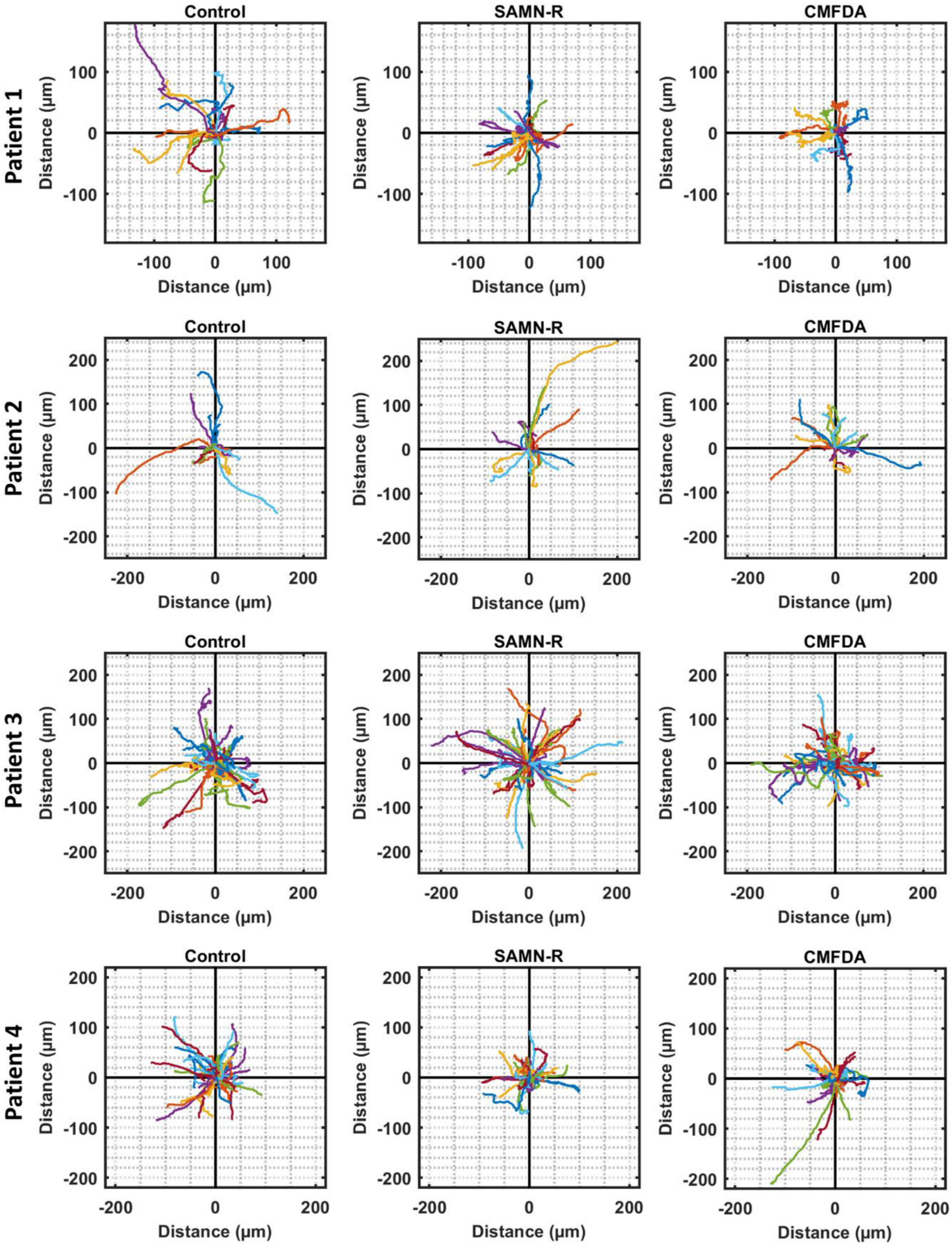

Figure 31. Rose plots of cell migration tracks. Cell migration tracks are shown from non-labelled, SAMN-R treated and CMFDA stained hMSCs from four patients. Each line represents the track of an individual cell for a six-hour period. The number of the tracks in the three groups are the same: 18, 20, 50, 50 cells from four patients, respectively.

After evaluating the results from four patients, the experimental conditions were improved. Three groups of cells (without staining, SAMN-R treating, CMFDA stained) were observed simultaneously. For this, on 35 mm glass-bottom dishes (20 mm well size, Cellvis) was embedded 3-well silicone insert (ibidi, GmbH) with 0.22 cm^2 growth area per well. In this case cells were seeded on three wells of insert (Figure 32). At the next day cells in one of the wells were treated with SAMN-R nanoparticles during 24 hours and cells in the second well were stained with CMFDA. After this time, cells in all wells were gently washed with PBS and fresh growth medium was added. Cells were observed by confocal microscope under the same conditions as the cells of the first four patients. Three fields of view from each well were chosen. Z-stacks with distance between adjacent images of 20 µm (focus on fluorescence and bright-field channel) were acquired from each field of view. Experiment was setting for six hours and during this time the images of fields of view were acquired with intervals of ten minutes. From each field of view images from bright-field channel, Green (CMFDA) and red (SAMN-R) fluorescence spectrum in sequence mode were obtained.

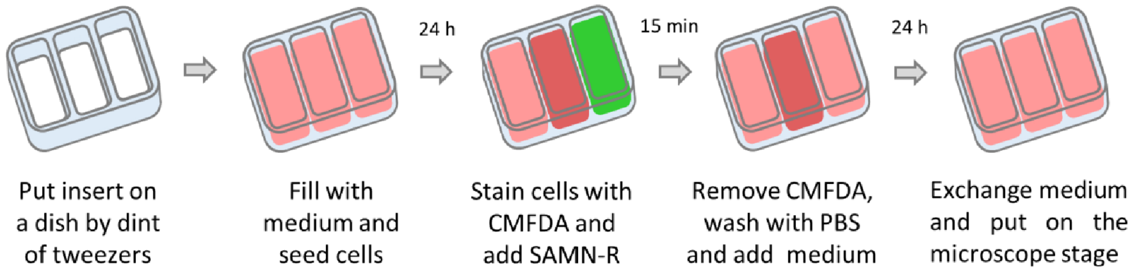

Figure 32. Cells preparation pipeline for single-cell migration experiment. Silicone insert marked with transparent blue colour. Cell culture medium marked with pink colour. CellTracker™ Green CMFDA Dye (CMFDA) mixed in serum free culture medium marked with green colour. Rhodamine-derived superparamagnetic maghemite nanoparticles (SAMN-R) in culture medium marked with red colour.

A disadvantage in this embodiment is a small grow area. It is possible to choose only three field of view from one well. On the other hand, it has some advantages. Using 3-well insert is suitable for three experiments in parallel. Also, because of short distance between of the wells and accordingly field of views, the microscope stage movement error gives less impact on the result. The cells from next four patients (Patient 5–8) were used in this type of experiment. The calculated value of velocity and accumulated and Euclidean distance hMSCs are listed in Table 16–Table 19. Rose plots of cell migration tracks from Patient 5–8 are in Figure 33.

Table 16. Migration of hMSCs in Patient 5 from 44 cells of control, CellTracker™ Green CMFDA (CMFDA) labelled, and rhodamine-derived superparamagnetic maghemite nanoparticles (SAMN-R) treatment groups. The velocity, accumulated, and Euclidean distance values for a six-hour period are shown.

Item	Control			SAMN-R			CMFDA		
	Min	Max	Mean	Min	Max	Mean	Min	Max	Mean
Accumulated distance (µm)	60.13	309.06	154.09	39.52	318.52	149.09	35.49	294.68	156.96
Euclidean distance (µm)	8.27	278.90	120.09	11.19	310.13	119.15	4.68	285.19	127.68
Velocity (µm/min)	0.17	0.86	0.43	0.11	0.88	0.41	0.10	0.82	0.44

Table 17. Migration of hMSCs in Patient 6 from 50 cells of control, CellTracker™ Green CMFDA (CMFDA) labelled, and rhodamine-derived superparamagnetic maghemite nanoparticles (SAMN-R) treatment groups. The velocity, accumulated, and Euclidean distance values for a six-hour period are shown.

Item	Control			SAMN-R			CMFDA		
	Min	Max	Mean	Min	Max	Mean	Min	Max	Mean
Accumulated distance (µm)	51.37	306.78	105.34	24.24	315.11	116.01	48.33	203.33	98.19
Euclidean distance (µm)	29.66	299.23	87.87	13.83	297.23	93.03	22.41	193.09	76.91
Velocity (µm/min)	0.14	0.85	0.29	0.07	0.88	0.32	0.13	0.56	0.27

Table 18. Migration of hMSCs in Patient 7 from 103 cells of control, CellTracker™ Green CMFDA (CMFDA) labelled, and rhodamine-derived superparamagnetic maghemite nanoparticles (SAMN-R) treatment groups. The velocity, accumulated, and Euclidean distance values for a six-hour period are shown.

Item	Control			SAMN-R			CMFDA		
	Min	Max	Mean	Min	Max	Mean	Min	Max	Mean
Accumulated distance (µm)	98.14	535.08	300.74	77.91	506.45	286.54	70.03	501.12	276.59
Euclidean distance (µm)	12.55	442.68	207.26	6.91	471.11	209.12	25.53	444.76	204.94
Velocity (µm/min)	0.27	1.49	0.84	0.22	1.40	0.80	0.19	1.39	0.77

Table 19. Migration of hMSCs in Patient 8 from 32 cells of control, CellTracker™ Green CMFDA (CMFDA) labelled, and rhodamine-derived superparamagnetic maghemite nanoparticles (SAMN-R) treatment groups. The velocity, accumulated, and Euclidean distance values for a six-hour period are shown.

Item	Control			SAMN-R			CMFDA		
	Min	Max	Mean	Min	Max	Mean	Min	Max	Mean
Accumulated distance (µm)	91.87	237.61	165.42	71.97	411.99	196.22	72.63	308.86	166.75
Euclidean distance (µm)	49.83	196.03	116.36	32.53	378.20	148.28	9.64	254.00	96.26
Velocity (µm/min)	0.26	0.66	0.46	0.20	1.15	0.55	0.20	0.86	0.46

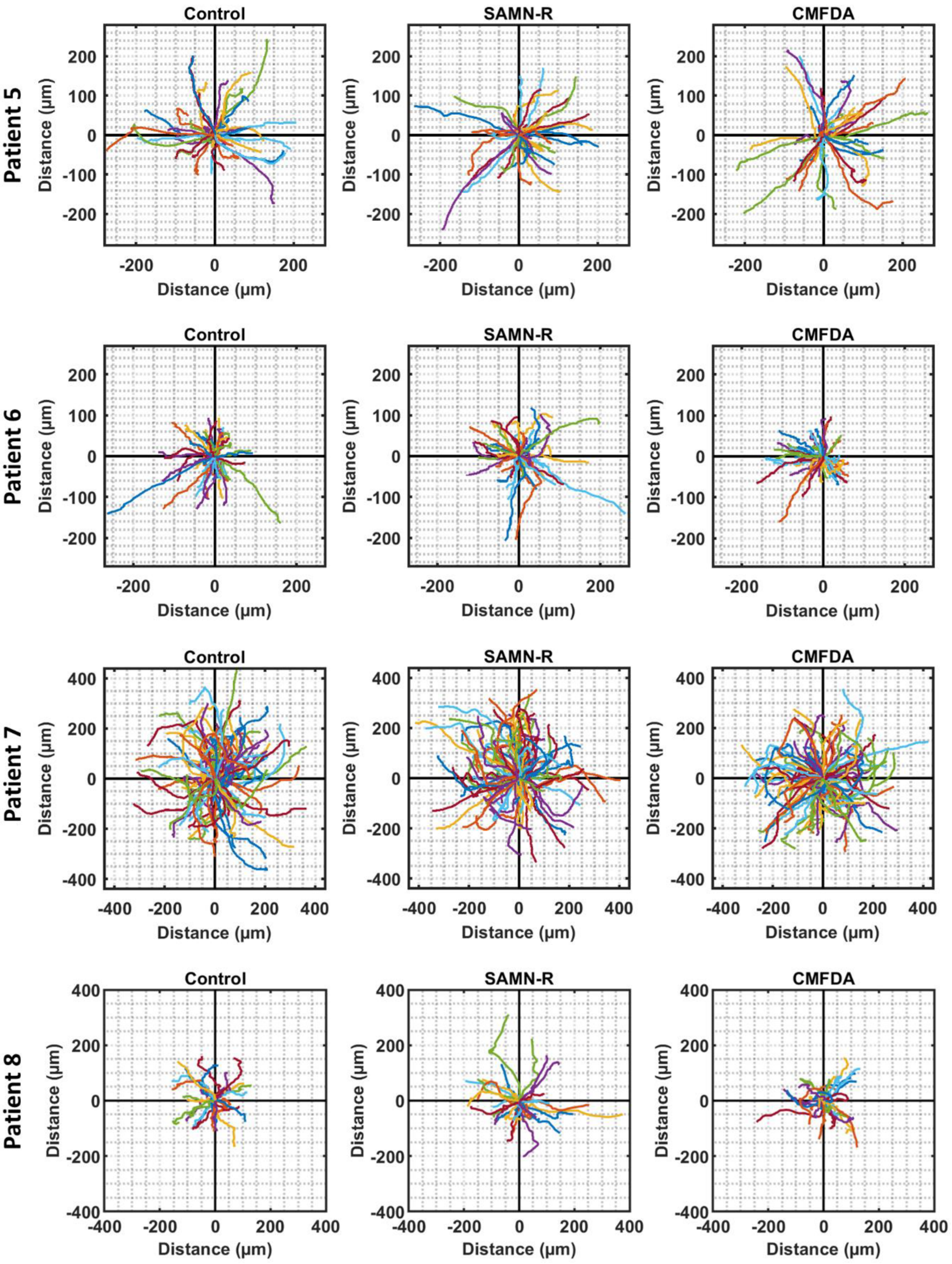

Figure 33. Rose plots of cell migration tracks. Cell migration tracks are shown from non-labelled, treated with rhodamine-derived superparamagnetic maghemite nanoparticles (SAMN-R) and stained with CellTracker™ Green CMFDA (CMFDA) hMSCs from four patients. Each line represents the track of an individual cell for a six-hour period. The numbers of the tracks in the three groups are the same: 44, 50, 103, 32 cells from four patients, respectively.

In the cell motility studies the main investigated parameter is cell velocity. In Figure 34 and Figure 35 the sets of single-cell velocities from eight patients are demonstrated. These boxplots show the data without outliers, which were defined using quartile range. In each group the number of studied cells from one patient was the same.

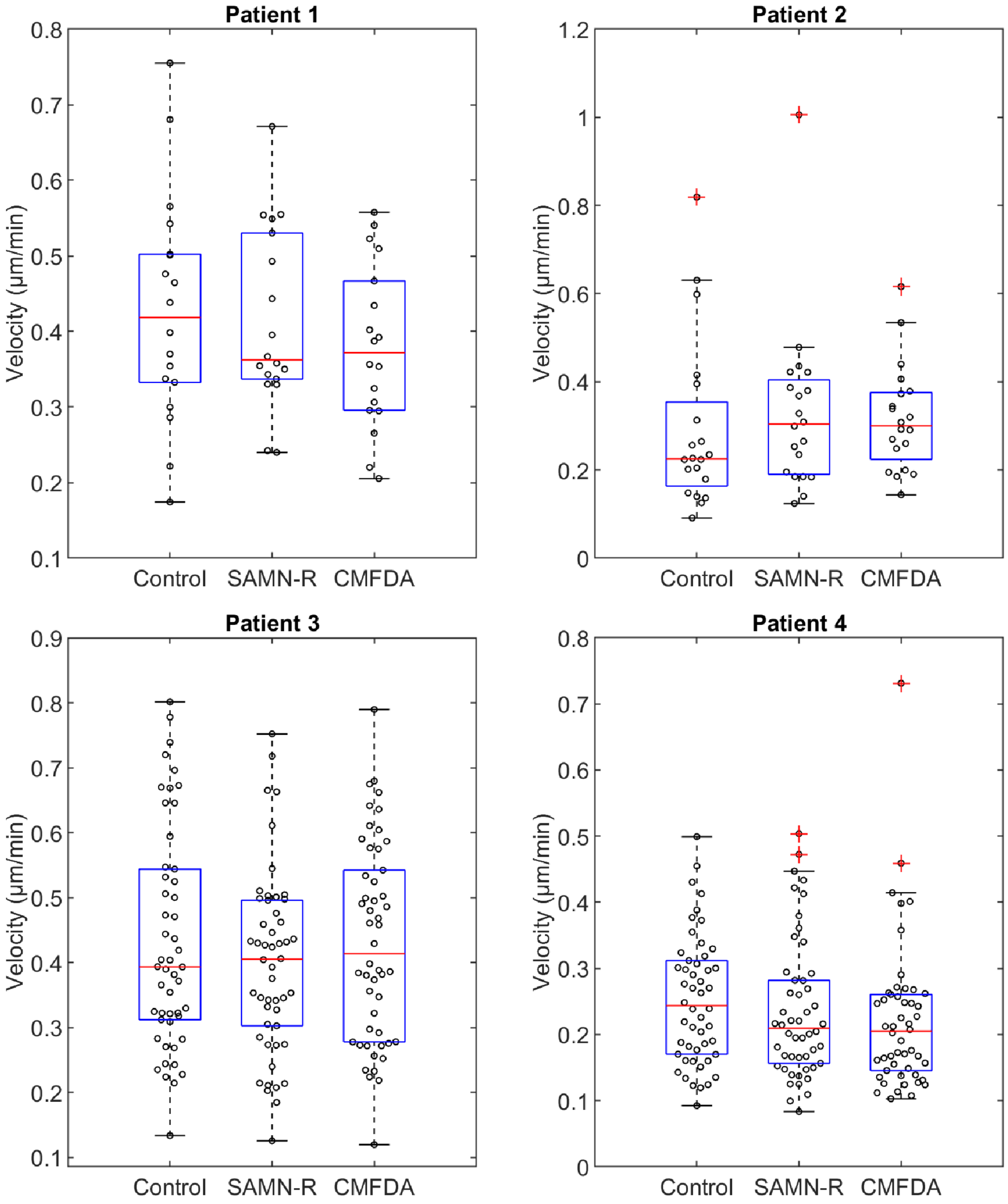

Figure 34. Calculated velocity from single hMSCs. Each box represents the complete set of single-cell velocities from four patients. There are 18 cells in each group from Patient 1, 20 cells from Patient 2, and 50 cells both from Patients 3 and 4. Boxes are composed of main box edges (25th and 75th percentiles), black dots (velocity values), central red horizontal line (median), whiskers (the most extreme values, outliers are not considered), and red squares (outliers).

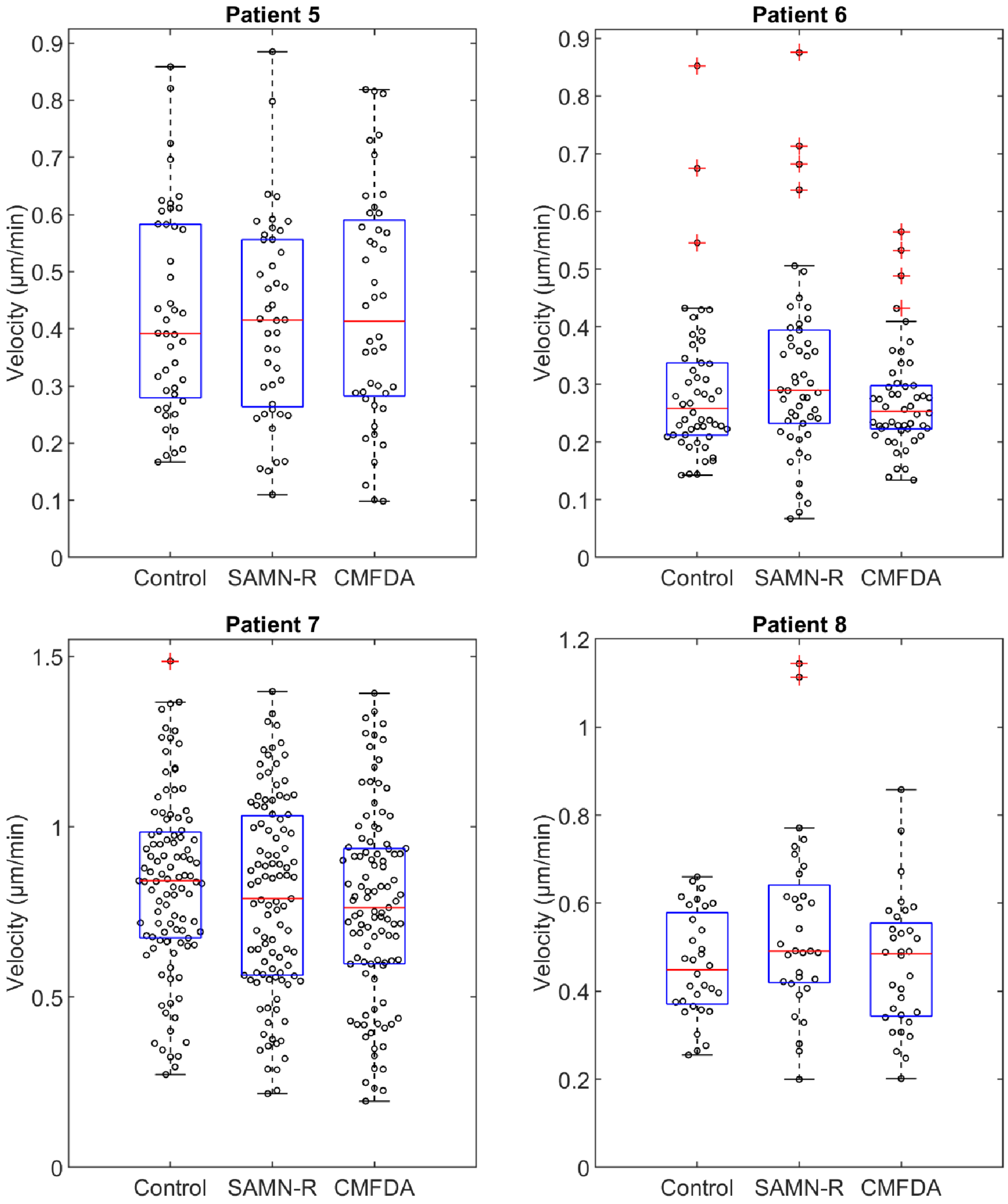

Figure 35. Calculated velocity from single hMSCs. Each box represents the complete set of single-cell velocities from four patients. There are 44 cells in each group from Patient 5, 50 cells from Patient 6, 103 cells from Patients 7, and 32 cells from Patient 8. Boxes are composed of main box edges (25th and 75th percentiles), black dots (velocity values), central red horizontal line (median), whiskers (the most extreme values, outliers are not considered), and red squares (outliers).

The effect of SANM-R and CMFDA labelling on cell motility was studied by statistical analysis performed in MATLAB software. Using the Shapiro-Wilk test [179], it was controlled whether the values in each group are normally distributed. The null hypothesis states that the values of compared groups are normally distributed. If the p-value was greater than 0.05 then the null hypothesis was accepted. The normal data distribution was not confirmed in the majority of groups (see values in regular type in the Table 20). Therefore, the Kruskal-Wallis nonparametric test [180] was used to determine whether there are any statistically significant differences between the means of the three tested groups.

Then the difference between non-labelled cells, SAMN-R-labelled cells and CMFDA-labelled cells was evaluated separately using Tukey-Kramer post hoc test [181]. In both statistical test the null hypothesis states that the means of compared groups are equal. When the p-value exceed 0.05, then the null hypothesis was accepted.

The results show that SAMN-R and CMFDA do not have a significant effect on cell motility (marked in bold in the Table 20) in the studied cells from all patients except Patient 4 (see values in regular type in the Table 20). Kruskal-Wallis test applied on the data from Patient 4 shows that there are differences at least between one of tested group. Then by the Tukey-Kramer test it was confirmed that the means of cell velocity from control and CMFDA stained cells are unequal. This result could be influenced by the fact that the groups of cells were observed separately at different times.

Table 20. Statistical tests applied on values of the velocity of single cells. Table of p-values from Shapiro-Wilk and Kruskal-Wallis, and Tukey-Kramer statistical tests. P-values greater than 0.05 marked in bold (null hypothesis is accepted).

	Statistical test						
	Shapiro-Wilk (p-value)			Kruskal-Wallis (p-value)	Tukey-Kramer (p-value)		
Group	Control	SAMN-R	CMFDA	All	Control / SAMN-R	Control / CMFDA	CMFDA / SAMN-R
Patient 1	**0.9160**	**0.1319**	**0.5933**	**0.5913**	**0.9823**	**0.5996**	**0.7129**
Patient 2	0.0057	**0.3797**	**0.7872**	**0.2585**	**0.4063**	**0.2748**	**0.9650**
Patient 3	0.0228	**0.2784**	**0.2520**	**0.6145**	**0.6902**	**0.9977**	**0.6498**
Patient 4	**0.1617**	0.0036	0.0028	0.0399	**0.2618**	0.0325	**0.6172**
Patient 5	0.0408	**0.3276**	**0.1307**	**0.8879**	**0.9292**	**0.9948**	**0.8887**
Patient 6	0.0277	**0.8141**	**0.5239**	**0.1478**	**0.3792**	**0.8257**	**0.1364**
Patient 7	**0.3051**	**0.1124**	**0.2708**	**0.2909**	**0.6075**	**0.2635**	**0.8152**
Patient 8	**0.1761**	**0.7232**	**0.3559**	**0.3060**	**0.3945**	**0.9969**	**0.3538**

According to observations, cells after mitosis cycle have the highest velocity. As seen in Figure 35 the distribution of values from Patient 7 is significantly different. There is large number of cells with velocity values higher than 1 μm/min. This may be explained by the fact that the density of cells was greater (Table 21). The large number of cells were divided during the observation time (according to cell growth curve). Therefore, it can be assumed that large number of cells could be in the stage after mitosis (G1 phase of the cell cycle). It means that these cells could have a high velocity. By conducting the long-term experiments using confocal microscopy, it was confirmed that nanoparticles do not hamper the cell division (Table 21). As shown in Figure 36, SAMN-R and CMFDA are transferred to daughter cells during mitosis. Also, their asymmetric distribution can be notice.

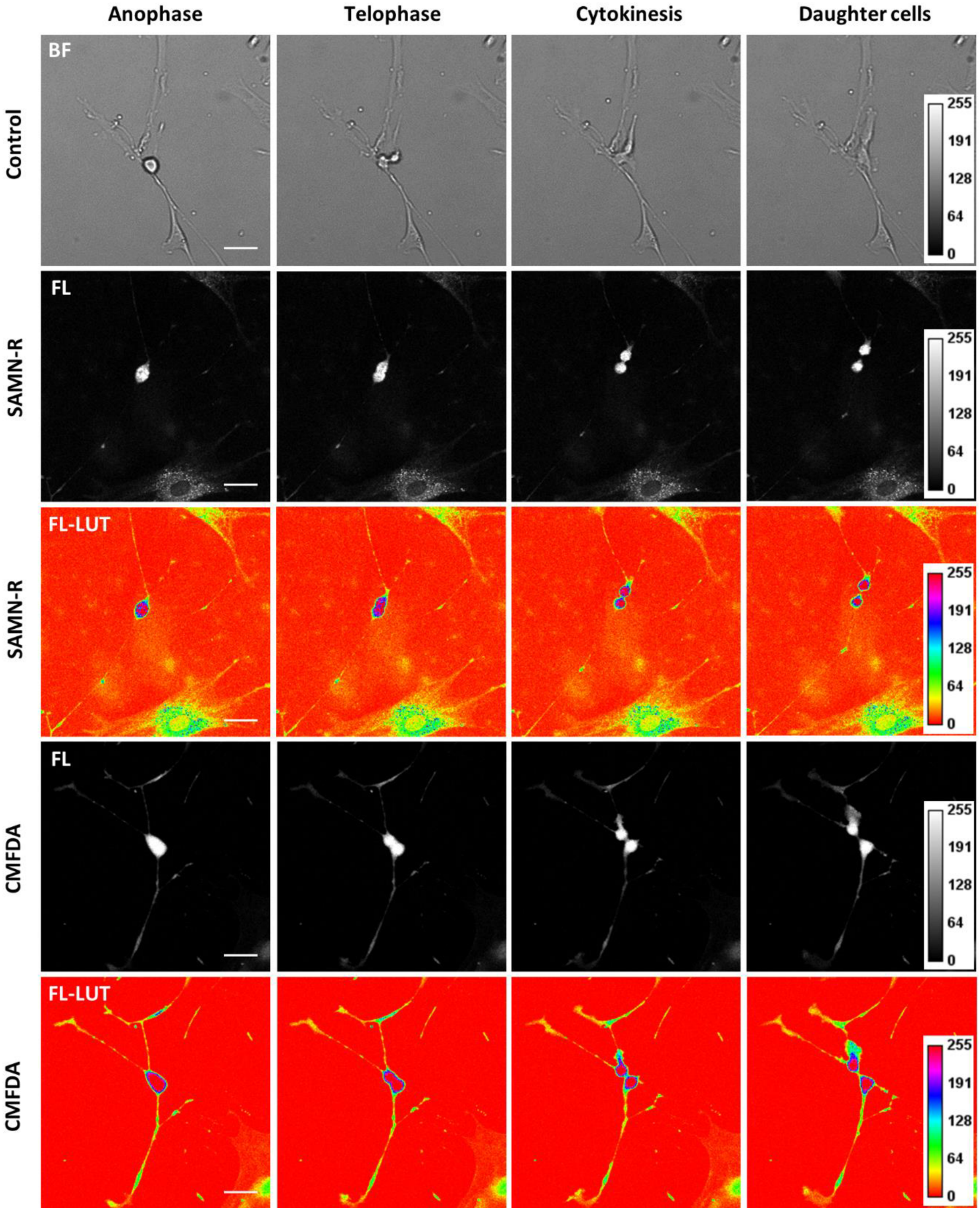

Figure 36. Division of non-labelled (control), rhodamine-derived superparamagnetic maghemite nanoparticles (SAMN-R) treated and CellTracker™ Green CMFDA Dye (CMFDA) stained hMSCs: anophase, telophase and cytokinesis mitotic phases. Images acquired with 5 min time interval by confocal microscopy: bright field (BF), fluorescence (FL) channel, heat map of fluorescence images (FL-LUT). Scale bar 50 μm, 10× magnification.

Table 21. Number of cell division during the observation time (6 hours). Data from hMSCs migration experiments.

Patient number	Number of fields of view	Density [cells·mm^{-2}]	Number of divisions		
			Control	SAMN-R	CMFDA
1	1	25	0	0	0
2	2	20	1	0	1
3	3	25	0	1	1
4	4	15	2	3	3
5	3	20	2	2	2
6	4	15	5	12	0
7	2	90	29	38	29
8	4	30	2	1	0

As previously confirmed, iron oxide nanoparticles penetrate intracellular compartment by endocytosis [97, 103, 104]. Therefore SAMN-R are localized in endosomes and lysosomes [58, 59, 61, 141]. The number of penetrated nanoparticles is random and their distribution in cytoplasm is inhomogeneous [100]. Endosomes and lysosomes are portioning into daughter cells with the random distributions [200–202]. The toxic effect of nanoparticles can affect cell mitosis. The presence of nanoparticles in the cytoplasm due to leakage from lysosomes with damaged membrane and changes in the level of ROS production can affect the process of cell division [105, 203]. The membrane of cell nucleus breaks down during mitosis. Therefore, nanoparticles have access to the inner compartment of the nucleus. Thus, they can inhibit cell division or cause mutations in the DNA [105, 203]. Previously, the possible effect of SAMN-R on cell proliferation was studied in the Chapter 6.2 was assumed that due to the possible effect of nanoparticles on the process of cell division, the mitotic cycle will be inhibited or stopped. Therefore, cell growth curve of SAMN-R treated cells will differ from the cells of the control sample. However, the difference between cell growth curves was not found, thus this assumption was not confirmed. In the study of cell proliferation (Chapter 6.2), cells were observed with a time interval of 24 hours. The setting of time-lapse experiment allows to observe cells with the shorter time interval. When studying the migration of single cells, the images from field of view were described every five or ten minutes (Chapter 7.2). Therefore, it was possible to observe cells in the different phases of mitosis. Figure 36 shows a comparison of duration of the mitotic phases of cells treated with SAMN-R, stained with CMFDA dye and cells from control sample. Significant changes were not found (quantitative analysis was not performed).

During long-term observations it has been determined that nanoparticles can remain in the intracellular compartment over several generations. Also, SAMN-R demonstrate good fluorescence which is able to maintain for a long time [60, 61, 92, 141]. Due to these properties, nanoparticles have proven to be suitable for long-term experiments.

7.3 DISCUSSION

The first initial experiments looked at the possible toxic effects of SAMN-R on cell viability and determined the optimal concentration of the nanoparticles (Chapter 6). Furthermore, the influence of SAMN-R in different concentrations was tested on 3T3 cells and hMSCs, and it was confirmed that a concentration of SAMN-R at a dose value of 20 $\mu g \cdot cm^{-2}$ is safe for living cells. This conclusion is based on the analysis of visible changes in cell morphology and changes in ROS production and cell proliferation. The selected concentration of SAMN-R was used in subsequent studies.

Nanoparticles interact with cell membrane receptors and can affect their functions. In [141], we controlled for cell size before and after nanoparticle treatment using flow cytometry analysis and confirmed that SAMN-R did not affect the size of cells and distribution of the tested CD surface molecules. MSCs were positive for CD90 and CD73 expressions, and 3T3 cells were positive for the CD90 expression. Neither cell line expressed CD45 markers. Their differentiation ability was not controlled.

Nanoparticles can also damage organelles and contribute to the disruption of the cytoskeleton, which is involved in cells' ability to move. Cells form filopodia and lamellipodia by actin polymerization [152, 197] and these cellular protrusions allow a displacement of the cytoplasm in the direction of migration. In this way, the effect on the actin can influence cells' motility, adhesion, and ability to migrate.

It was assumed that nonvisible changes in cellular structure can be observed using methods of studying cell migration, which was examined in Chapter 7.1 using the scratch assay. This is an accessible method of studying collective cell migration because it allows researchers to observe changes in cell connections, communications, motility, and the potential of wound areas to be closed under the influence of different treatments. In this part of the research, the 3T3 cells were observed. It was assumed that cells treated with SAMN-R would migrate slowly or lose their tendency to close the wound area due to changes in the expression of the cell membrane surface, which plays an important role in the regeneration process [122–124], but the statistical test did not confirm any significant effect of SAMN-R treatment on collective cell migration.

MSCs in *in vivo* conditions display an ability to migrate toward chemokines [122–124]. During this process, which includes their transendothelial migration and migration in ECM, MSCs generally migrate singly, and therefore it was decided to study the migration of MSCs as single cells (Chapter 7.2). In this part of the study, the adipose-derived hMSCs from eight patients were observed and the possible effects of SAMN-R treatment examined by comparing the speed of single-cell migration. Normally, MSCs include a population of rapidly and slowly moving cells [138, 139] and therefore the cell speed values can vary significantly between patients (Figure 34, Figure 35). The statistical analysis performed did not confirm any significant effect of SAMN-R treatment on single-cell migration.

Groups of cells were stained with the CMFDA dye to look at cell proliferation (Chapter 6.2) and collective and single-cell migration (Chapter 7). This dye is presented by the manufacturer as non-toxic and suitable for long-term experiments. CMFDA dye [167] stains entire cells, which offers advantages for the application of cell segmentation algorithms. These experiments confirmed that this dye exerts no significant effects on cell proliferation and motility.

The segmentation algorithms presented in Chapter 5.2were used for the analysis of cell proliferation and collective cell migration. The SAMN-R were not taken up into the nuclei and mainly mark the lysosomes that are distributed in the cytoplasm. The detection of the cells treated with SAMN-R was similar to that of cells stained with CMFDA. An algorithm designed for the segmentation of entire cells can be adapted by including the morphological operation of filling holes.

Cell-tracking algorithms are based on cell segmentation, but the segmentation of non-labelled cells on images acquired *via* a light microscope is problematic. Various contrast microscopic techniques can be used to visualise biological samples. Fluorescence microscopy offers an advantage in that it makes it possible to observe 3D structures in biological samples, cells in ECM, and different scaffolds, while cell labelling can help to separate different cell types in the same studied sample. In some experiments it is necessary to mark the control sample and, in this case, the use of a non-toxic dye is advisable. For this reason, this study compared the effects of CMFDA staining and SAMN-R treatment.

Chapter 5.2.4 presents an algorithm for tracking single cells. This algorithm is not fully automatic and includes manual corrections for cell detection. It is appropriate for the detection and tracking of cells that are marked with a fluorescent dye that stains whole cells. In this study, it was decided to include a control cell group without staining, and therefore manual tracking was used to ensure that all cell groups were analysed *via* the same method.

Microscope manufacturers tend to incorporate algorithms that enable automatic cell tracking into modern microscope control software but cell tracking still represents a significant challenge [183]. There are many factors that affect the efficiency of basic segmentation methods. Researchers use a variety of cell types, markers, and microscopic techniques. It is still necessary to solve the problem of tracking mitotic cells [184, 185], and researchers also use distinct experiment settings such as image resolution and time intervals. The use of deep learning algorithms is a promising solution in the field of fully automatic cell detection and tracking.

8 HUMAN ADIPOSE-DERIVED MESENCHYMAL STEM CELLS AND HL-1 CARDIAC MUSCLE CELL LINE IN CO-CULTURE

The therapeutic potential of MSCs is based on their paracrine and immunomodulatory properties [2, 204]. Damaged tissue produces some chemokines, which are the signal for MSCs to migrate in the direction of the concentration gradient of chemokines. This process is accompanied by producing of different mediators and factors, that can involve the proliferation and function of the immune cells. Also, in addition to osteoblasts, adipocytes and chondroblasts, MSCs have the capacity to differentiate into hepatocytes, epithelial cells, smooth muscle cells, cardiomyocyte-like cells, neuron-like cells, and others [2, 4]. These are the main reasons of their widespread use in tissue regeneration research and therapy [5–20, 41, 205]. To study regenerative and therapies fields of research MSCs are widly used in *ex vivo* and *in vivo* experiments. Many studies show, that they are successful in regeneration of myocardial damage after MI [9, 26, 34, 35, 37, 39].

The participation of cells in wound tissue healing after MI is studied in *in vivo* experiments. For example, in [206], rats were subjected to MI by transient coronary artery occlusion or to sham MI. Then fluorescently labelled MSCs were delivered by infusion by a left ventricular cavity. After one week a histological analysis confirmed MSCs presence in infarcted zone. The other method is the delivery of MSCs by injection. For example, in [35], MSCs were injected in the border zone of acute infarct. Later, the use of MSC in combination with ECM, such as hydrogel, helped to keep most of the applied cells in the desired zone [207, 208]. In addition, ECM gels may be functionalized with cytokines and growth factors, which promotes damage tissue regeneration. Using MSCs in *in vivo* studies shows great results. Nevertheless, there are some complications as tumorigenicity, proinflammation, and fibrosis [40, 41]. Therefore, the capacity of variety *in vitro* studies increases and research in this field is still relevant. They include basic studies on 2D as well as pseudo-3D and 3D experiments. The use of different biocompatible scaffolds of variable shapes for imitating the ECM helps to expand research in cardiac tissue engineering field [36, 42]. Thus, the *in vitro* conditions may be very close to *in vivo* experiments. Modern technologies such as bioprinting have expanded possibilities in this area. In addition, for a better understanding of cells participation in cardiac tissue regeneration, the co-culture experiments are performed in *in vitro* cardiac tissue models.

There are some studies, where isolated adult cardiomyocytes and MSCs were used in *in vitro* co-culture experiments. For example, in [32], our team used adult cardiomyocytes isolated from rat heart. By using the isolation protocol [209], a cell suspension containing the separated cells was obtained. Two wells were connected by small tunnel (cross-sectional area of 0.8 mm^2 and length of 5 mm) that were filled with type I collagen from rat tail. Collagen is a suitable material as an ECM. One well was filled with cardiomyocytes cell suspension, on the other well rat bone marrow MSCs were seeded. Cardiomyocytes produce chemokines, that stimulate MSCs to migrate toward them. This chemotaxis effect was studied. Also, it was confirmed that the orientation of collagen fibrils can affect the direction of migrating cells. In the other study [31], the transwell chambers with porous membrane were used. The lower compartment was filled with freshly isolated porcine primary adult cardiomyocytes. On the upper compartment, the porcine bone marrow MSCs were seeded. The two types of cells are separated by a porous membrane. MSCs can migrate through the pores to the other side of the membrane. Thus, the effect of chemokines or growth factors can be studied. The results show that cardiomyocytes in co-culture with MSCs had better survival and viability without affect the main mitochondrial and cells contractile functional parameters. In both methods, two types of cells were cultured without contact. The adult cardiomyocytes cell suspension contains both live and dead cells. A large number of cells die within 24 hours. Moreover, cell morphology begins to change: shrinks in length, the edges become round and curled, the density of t-tubules changes noticeably. However, cardiomyocytes (with the presence of dead cells) can be cultured for up to two weeks under suitable conditions [210, 211]. Tissue health, successful isolation, culture conditions affect cell viability. Controlling the density of living and dying cells is very problematic. Therefore, the experimental conditions are very difficult to repeat. However, the ability to select cells from different areas of the heart including a specific region of the heart following MI is the main advantage of using adult cardiomyocytes.

Another suitable way is the use of neonatal cells for co-culture experiments. In comparison with adult cardiomyocytes, isolation of neonatal cells is simpler and cell culture is easier. In the study [33] cardiomyocytes isolated from hearts of rat embryos were used in co-culture with human bone marrow MSCs. In this case, cell-to-cell contact could be observed. MSCs in suspension obtained after passage were added to cultured cardiomyocytes. Then, after 24 hours, cells were analysed. It has been found that, upon cell-to-cell contact with neonatal cells, MSCs are capable of transferring mitochondria. Probably, this may be one of the ways for MSCs to participate in the cell repair.

Unfortunately, isolation of cells from living tissue may not be available to the laboratory for different reasons. An alternative solution would be to use differentiated induced pluripotent stem cells (iPS cells) or MSCs. Adipose-derived MSCs, bone marrow MSCs and some other types have potential to differentiate into cardiomyocyte-like cells under special *in vitro* cultivation conditions. A common way is a long-term culture in a growth medium containing 5-azacytidine [27–30]. The main disadvantage of this option is the long differentiation time. These methods are labour intensive and expensive. For some laboratories, the use of proliferative cell lines may be the best solution. For example, AC16 human cardiomyocyte cell line and HL-1 cardiac muscle cell line. In this work HL-1 cardiac muscle cell line was chosen as a cardiac tissue model.

In this work hMSCs and HL-1 cells in co-culture were studied using scratch assay experiment. HL-1 cardiac muscle cell line was used as a cardiac tissue model. This cell line was chosen due to morphological, electrophysiological and gene expression characteristics. For this experiment, 2-well and 3-well silicone insert (ibidi, GmbH) with 0.22 cm^2 growth area per well was embedded on 35 mm glass-bottom dishes (20 mm well size, Cellvis) (Figure 37). Two adjacent wells of 3-well insert were filled with Claycomb growth medium. One (empty) well of 3-well insert and two wells of 2-well insert were filled with DMEM low glucose growth medium for hMSCs. After passage HL-1 cells were seeded on two adjacent wells of 3-well insert. Then hMSCs were passaged and seeded on one well of 3-well insert and two wells of 2-well insert. The density for seeding was chosen so that cell confluency could reach 80–100% during 24 hours. At the next day, 24 hours seeding, HL-1 cells were stained with CMTPX dye and hMSCs were stained with CMFDA dye. After staining cells were gently washed with PBS. Then, 2-well and 3-well silicone inserts were removed. Culture dish was filled with 3 ml of Claycomb growth medium.

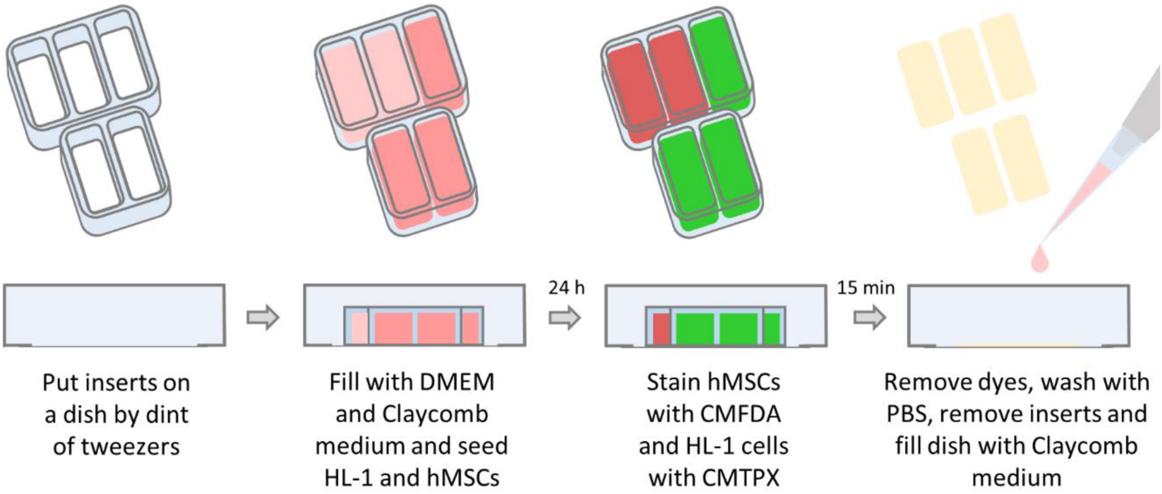

Figure 37. Pipeline of enhanced scratch assay test preparing for HL-1 and hMSCs. Silicone insert marked with transparent blue colour. HL-1 cells in Claycomb medium – light pink, hMSCs cells in DMEM – pink. CellTracker™ Green CMFDA Dye (CMFDA) mixed in serum free DMEM medium marked with green colour, and CellTracker™ Red CMTPX Dye (CMTPX) mixed in serum free Claycomb medium marked with red colour. Adhering cell on the dish after inserts removed – yellow.

Then cells on the prepared dish were placed on confocal microscope stage, equipped with incubator chamber (5% CO_2, 37°C). After 30 minutes, the image acquisition settings were set. The cell migrating was observed during 24 hours. During this time the images of field of view were acquired with 30 minutes interval. In this experiment the images were obtained from several fields of view. Three fields of view were chosen in each scratch area using multi-view mode (mark and find function). Images were acquired in three channels: bright-field, green (CMFDA) and red (SAMN-R) fluorescence spectrum. Sequence mode for image acquisition (excitation in these channels occurred separately) was set. The objective magnification of 10× was used. The size of field of view was 1.16 × 1.16 mm. It was set two Z-stacks with distance of 20 µm (focus on fluorescence and bright field channel). Images were acquired with a resolution of 1024 × 1024 pixels and a 100 Hz scan speed and bidirectional scanning. The dish was placed in humidified incubator (5% CO_2, 37°C) after image acquisition. At the next day cells were controlled. In Figure 38 images from one field of view at five-hour time intervals from start and end time are demonstrated. The scratch width was 500 ± 100 µm.

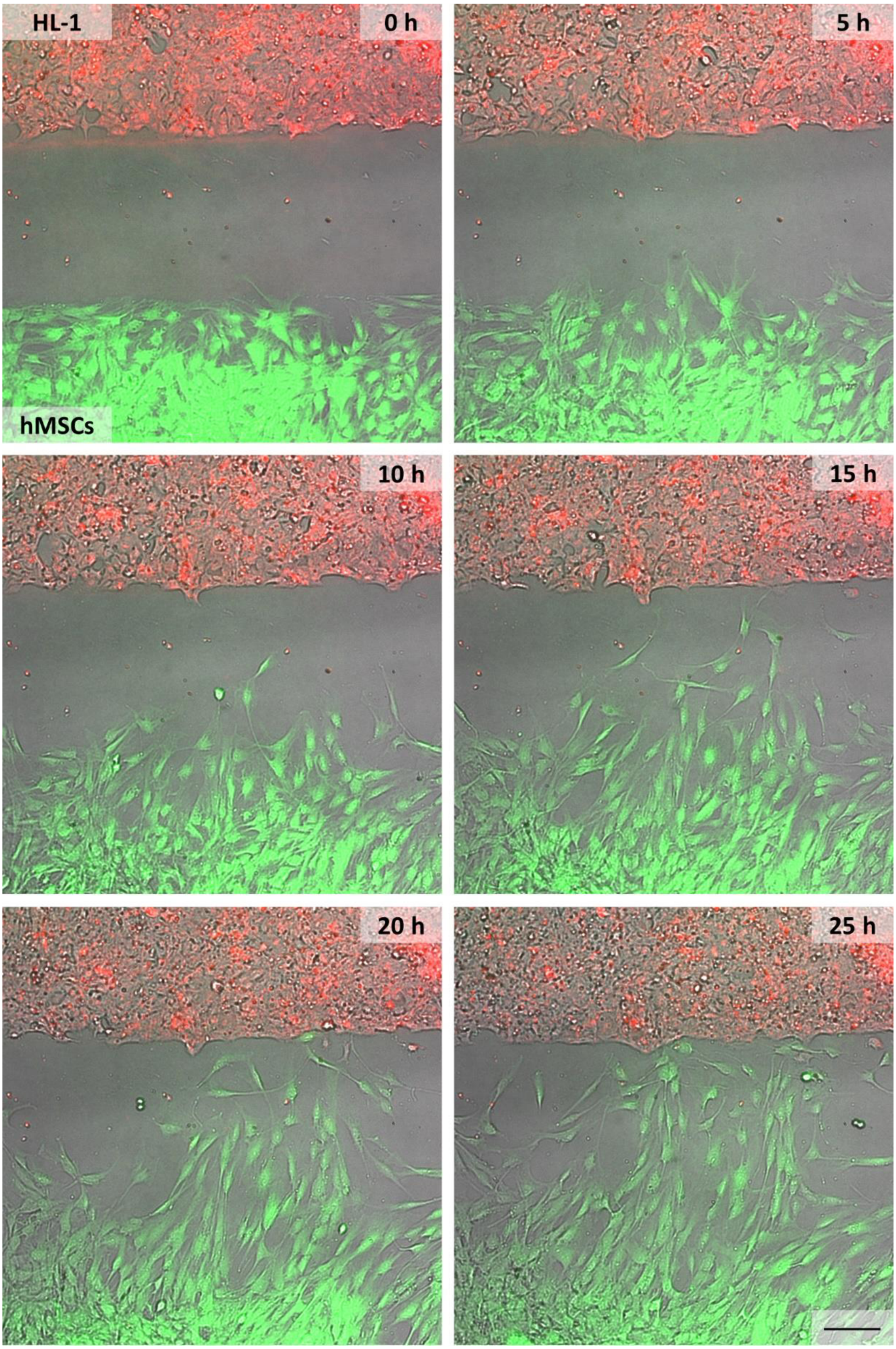

Figure 38. Scratch assay of hMSCs and HL-1 cells. Image of the same field of view at five-hour time intervals. Confocal microscopy, overlay bright-field, green (CellTracker Green CMFDA Dye) and red (CellTracker Red CMTPX Dye) channels, 10× magnification, scale bar 150 μm.

The acquired image sequences from bright-field channels were analysed by a custom segmentation algorithm (chapte 5.2.2) which were introduced before in this work. Analysis was based on calculating the open area present at the scratch area. Results from the three experiments are demonstrated in Figure 39. The graphs show scratch overgrowth of six fields of view within 24 hours.

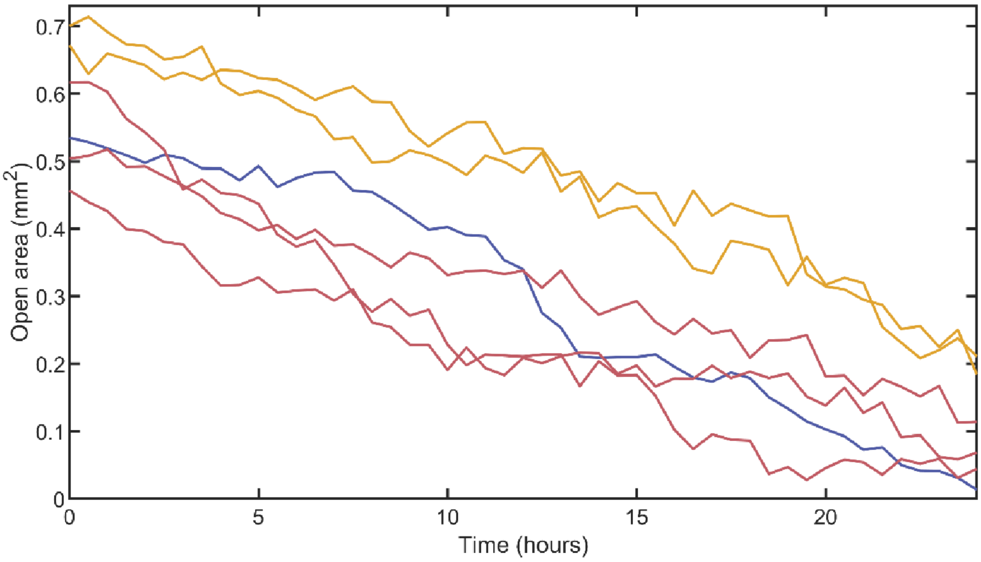

Figure 39. Scratch assay of hMSCs and HL-1 cells. Scratch overgrowth graph from three experiments (blue, red, yellow). Data from six fields of view was obtained within 24 hours with a time interval of 30 minutes.

In scratch assay experiment, hMSCs usually move as single cells. The cells migrated on the scratch area, distributed throughout the area and gradually increased their density until 100% confluency. According to observations the first contact of single hMSCs with HL-1 cells occurred within 6–12 hours.

Human adipose-derived MSCs tended to make contact in the form of nanotubes and fill open area in HL-1 cell monolayer over time (Figure 40). According to research [33], it is assumed that mitochondria are transmitted through nanotubes from hMSCs to HL-1. This assumption has not been tested yet.

Unfortunately, in this type of experiment, there was a problem of staining cells. Fluorescence weakened quickly due to the photobleaching effect. The problem can be partially solved by increasing the staining time or the concentration of the dye used. Unfortunately, this decision can adversely affect cell viability. This effect (photobleaching) was not observed in long-term experiments where hMSCs were cultured in DMEM. It can be assumed that this may happen due to reaction with the Claycomb growth medium and changes of intracellular metabolism. Another decision to solve problem of cell staining is to use alternative fluorescent dyes. In Figure 40 the hMSCs and HL-1 in co-culture within 24 hours is demonstrated. In this example hMSCs were treated with SAMN-R. In this case, the nanoparticles showed stable fluorescence for a long time. Therefore, SAMN-R can be proposed as a suitable type of cell stain for this type of experiment.

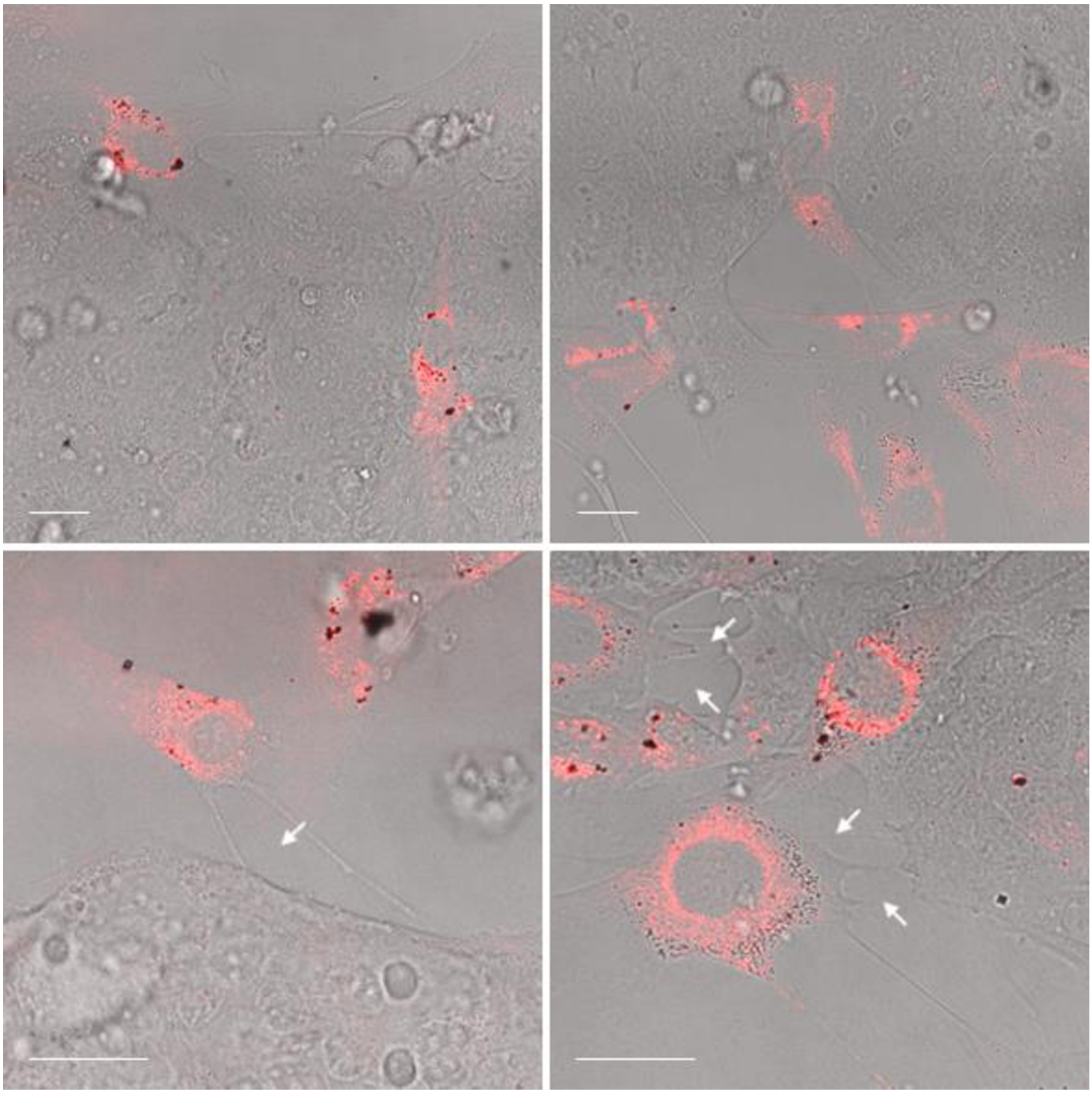

Figure 40. Cell communication of hMSCs and HL-1 cardiac muscle cell line. Red colour indicates hMSCs treated with rhodamine-derived superparamagnetic maghemite nanoparticles (SAMN-R). Nanotube formation marked with white arrow. Confocal microscopy, 63× magnification, scale bar 20 µm.

Human adipose-derived MSCs tended to make contact in the form of tunneling nanotubes and fill open area in HL-1 cell monolayer over time (Figure 40). The studies show that cells can transfer plasma membrane components, small cytoplasmic molecules and organelles between contacting cells through nanotubes [212, 213]. For example, it has been confirmed that cells are capable of transferring mitochondria [214, 215]. Thus, the formation of nanotubes can have a cell repair role. Additionally, mitochondrial transfer from hMSCs to cardiac cardiomyocytes was confirmed [33]. According to these studies, it is assumed that mitochondrial transferring through nanotubes from hMSCs to HL-1 is possible. This assumption has been tested but is not currently confirmed. The results obtained are difficult to interpret correctly. To repeat this experiment, it is necessary to update the protocol regarding the choice of dyes.

8.1 DISCUSSION

HL-1 cardiac muscle cell line express similar genes to adult atrial cardiomyocytes [143]. A confluent culture also has the ability to spontaneously contract [143, 144]. HL-1 can be used as an *in vitro* beating model, which is useful for detailed studies of action potentials in the heart muscle. Cell culture electroactivity and intracellular dynamic processes can be studied by means of *in vitro* microelectrode array (MEA) systems, which are based on extracellular recordings of voltage fluctuations and allow simultaneous and parallel recording from multiple channels for a long period of time, in which it is also possible to detect subthreshold potential changes as well as single and multiple action potentials [216, 217]. The number, design, shape, and type of metal and the coating of microelectrodes are chosen based on the type of cells in use in extant studies [218–221]. For example, the use of a nanopillar electrode array allows for the recording of intracellular action potentials from single cells in an adherent culture [222]. The use of the MEA technique is compatible with traditional patch-clamp methods [222, 223] and optical techniques [145]. Novel fluorescent voltage-sensitive dyes or genetically encoded voltage indicators (GEVIs) are used to monitor intracellular ion exchanges and protein dynamics [224, 225]. GEVIs allow for the tracking of the spatiotemporal electrical activity of single cells and tissue cultures, provide a high fluorescence response, and perfectly detect subthreshold membrane voltage changes. For instance, Accelerated Sensor of Action Potentials 1 (ASAP1) is a fluorescent membrane voltage sensor with a circularly permuted GFP that allows for the tracking of subthreshold membrane potential changes, single-action potentials, and fast trains of action potentials (up to 200 Hz) [226]. ASAP1 offers very fast kinetics of about 1–2 ms because it was originally developed for the encoding of neural communication [225, 226]. Despite this, it has also been applied to other types of cells [88, 145, 225, 226]. For example, in [145], our team performed the transient transfection of HL-1 cells with ASAP1 DNA plasmid using a linear PEI (Figure 41 (B)). In this work, a combination of MEA and fluorescence techniques has been used simultaneously to study the electrical and fluorescence recording of HL-1 cells' electrical activity in response to extracellular Ca^{2+} changes.

Gene delivery is often used in experimental medicine. Genetically modified cells can express functional ion channels and produce growth factors, antibodies, and viral vectors for therapeutic, gene therapy, and vaccine applications [85]. Magnetic nanoparticles are employed in the magnetofection method to deliver plasmids to intracellular compartments [86, 87]. For instance, iron oxide nanoparticles are biodegradable, are not cytotoxic in optimal concentrations, and their surfaces can be modified with fluorescent dyes, polymers, and proteins [81]. SPION coated with biocompatible polymers such as PEI, PLL, PEG, and Chitosan have improved the binding capability of DNA to surfaces. These magnetic nanoparticles are targeted at cells by a magnetic field that is generated by an external magnet or by endocytosis. This technique also increases the efficiency of DNA delivery and gene expression [89, 90].

In [88], we used SAMN-R nanoparticles for intracellular DNA vector delivery and post-transfection localization of this vector in the 3T3 cell line (Figure 41 (C)). The surface of SAMN-R was conjugated with Rhodamine B isothiocyanate because fluorescent labelling allows for the localisation of nanoparticles that have penetrated into cells. Their surface was modified with linear PEI and medium molecular-weight Chitosan to increase ASAP1 DNA vector adhesion. ASAP1 membrane voltage sensor with circularly permuted GFP can be detected on green channel with settings that correspond to the GFP spectrum.

SAMN-R nanoparticles can successfully penetrate HL-1 cells (Figure 41 (A)). Based on previous studies, it can be assumed that HL-1 cells can be successfully transfected using this complex of SAMN-R nanoparticles and ASAP1.

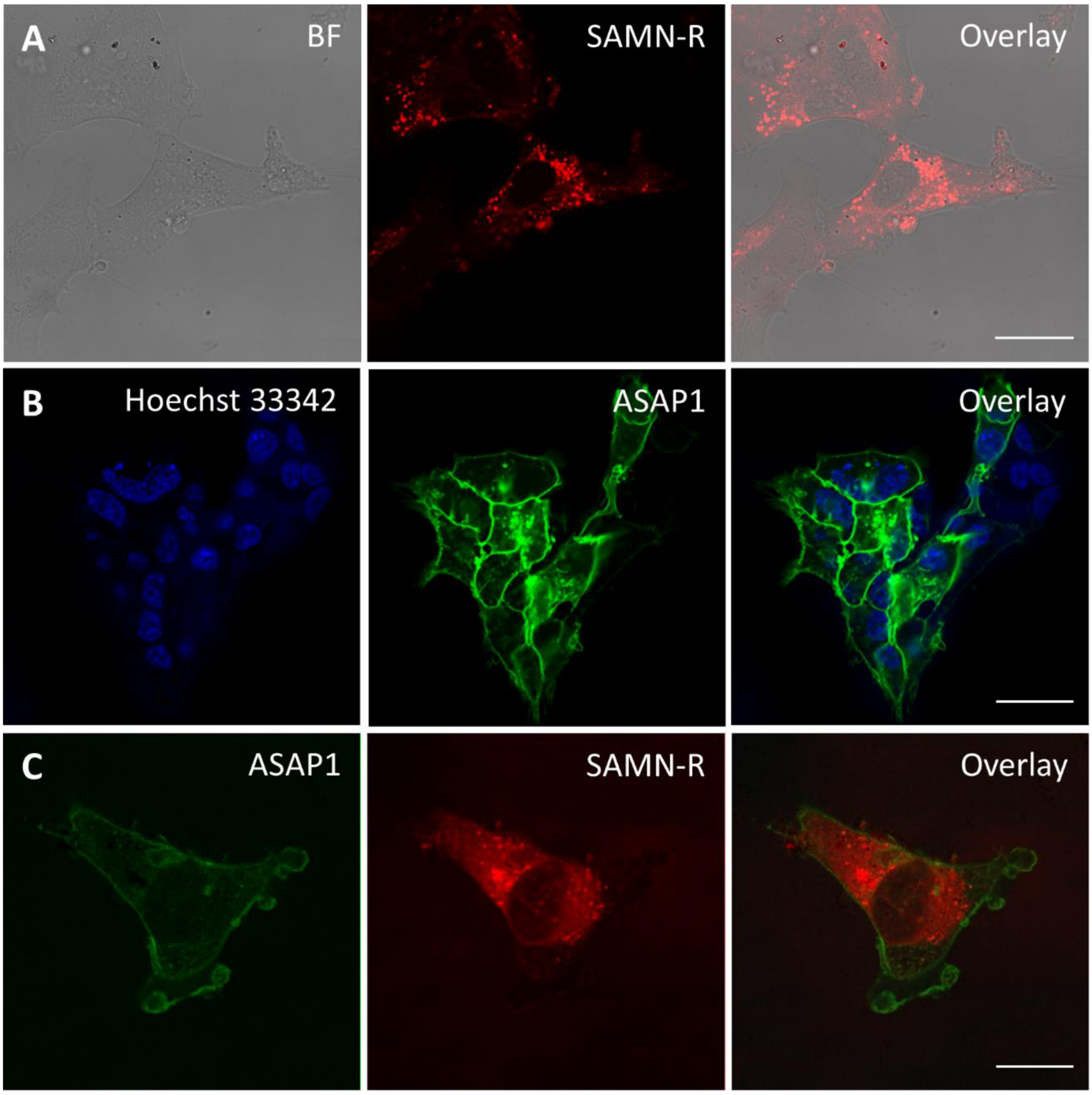

Figure 41. Confirmation of ASAP1 plasmid expression and rhodamine-derived superparamagnetic maghemite nanoparticles (SAMN-R) localization: (A) HL-1 cells treated with SAMN-R (red channel); (B) HL-1 cells expressing ASAP1 plasmid (green channel); nuclei stained with Hoechst 33342 (blue channel); (C) 3T3 cells expressing ASAP1 plasmid (green channel), SAMN-R distribution (red channel). Confocal microscopy, 63× magnification, scale bar 20 μm.

HL-1 cells are an interesting cardiac tissue model for, for instance, testing the functionality of ion channels. At another point, the possible transfer of nanoparticles into cells is of interest in conjunction with the possibility of plasmids and drugs delivery. The use of nanoparticles offers great potential in gene therapy [172].

Studies of cell-to-cell communication between hMSCs and cardiac tissue offer great potential in regenerative medicine. Previous studies have confirmed that hMSCs differentiated to cardiomyocytes and have the ability to perform spontaneous beating [29]. It can be assumed that they may possess electroactivity when introduced into HL-1 cardiac cell line. This supposition can be confirmed by the use of, for example, MEA systems. In [227], mouse bone marrow MSCs were added to an HL-1 monolayer cultured on MEA dishes and it was confirmed that MSCs affect the frequency of the spontaneous beating of HL-1 cells.

There are some studies that have looked at the interactions between MSCs and HL-1 cell lines such as gained gap junctions, the secreting of paracrine factors, and the antiapoptotic effect [123, 227–230]. In this study, adipose-derived hMSCs and HL-1 cardiac cell lines were used in *in vitro* co-culture experiments. In this work the scratch assay was performed to confirm whether HL-1 cells give a signal that causes hMSCs to migrate toward them, and it was observed that hMSCs tend to migrate toward the HL-1 and close the wound area (Figure 38). The first contact of these two cell lines usually occurred 6–12 hours after the removal of the inserts used to create a wound area, which had a width of 500±100 µm. The speed of the first contacting cells corresponds to the maximum speed of hMSCs in conditions without a chemoattractant or any type of stimulation (Chapter 7.2). The character and rate of wound closure of all hMSCs proved to be similar (data not shown), while it was also observed that hMSCs in co-culture with HL-1 cells form contacts as tunneling nanotubes (Figure 40). A number of studies have confirmed the possibility of mitochondrial transfer through formed nanotubes [33, 214, 215].

This study attempted to confirm the ability of hMSCs to transfer mitochondria to HL-1 cells during the first contact. Unfortunately, it was not possible to draw unambiguous conclusions based on the first results. For this experiment, hMSCs mitochondria was stained with MitoLite™ Red FX600 (AAT Bioquest, Inc., USA) and the membranes of both cell types with CellBrite™ Steady 650 Membrane Staining Kit (Biotium, Inc., USA). For HL-1, the stained mitochondria were found (data not shown). It was assumed that they can be stained *via* a small amount of dye in the medium or during the contact. It can also be a small piece of hMSCs filopodia. This being so, the results obtained cannot be interpreted correctly without confirming or refuting the assumption.

HL-1 cells in co-culture with MSCs are a promising experimental model and offer significant potential in the field of heart disease research and cardiac tissue regeneration. Future research would benefit from studying this connection in the context of hMSCs and HL-1 cardiac cell line, while the properties of both cell lines open up interesting possibilities in the fields of the application of transfection methods and cell electroactivity.

9 OVERALL CONCLUSIONS

This work focused on the application of fluorescent methods in use in *in vitro* studies to the field of regenerative medicine. Of particular interest is the possibility of using MSCs in cardiac tissue regeneration and the application of modern fluorescent probes including nanoparticles as SPION for long-term cell observation.

Bone marrow MSCs were widely used in the first studies in this area since they were the first to be identified as cultures of MSCs. Bone marrow is one of the largest resources of this cell type and their isolation offers minimal risk for patients, but recent studies have shown that MSCs isolated from different tissues have very different functions. They differ in their ability to differentiate into a variety of cell types, express growth, and regenerative factors, among other elements, and therefore have different roles and success levels in tissue regeneration. This work has made use of adipose-derived MSCs due to their great potential in cardiac tissue regeneration, as has been shown in many previous studies. Adipose tissue is an accessible and large source of MSCs, while their ability to be isolated during local anaesthesia reduces the risk to the patient. If one is to focus on the field of cardiac tissue regeneration, it is necessary to select an appropriate cardiac tissue model. Initially, isolated adult cardiomyocytes were used but, unfortunately, their long-time cultivation is very demanding and difficult, so it was decided to use an adherent cell line. The HL-1 cardiac muscle cell line was chosen due to its morphological, electrophysiological, and gene expression characteristics, which are similar to adult atrial cardiomyocytes. Some studies have examined MSCs and HL-1 cells in co-culture. Both cell lines offer appropriate properties and functions for *in vitro* cardiac tissue model; therefore, in this work it was decided to use adipose-derived MSCs and HL-1 cardiac muscle cell line. The subculturing procedures and the preparation of the experimental samples were performed in a clean room in biosafety conditions. The protocols for the subculturing and use of chemicals are shown in Chapter 4.1.

It is necessary to use microscopic techniques for 2D and 3D imaging when studying tissue engineering and regenerative medicine. Cardiac tissue engineering measurements are usually performed on 3D structures such as tissues, biocompatible scaffolds, and ECM gels. Such studies include the imaging of 3D structures and the determination of cell distribution in 3D models, while in co-culture experiments, it is necessary to mark cells to separate different cultures from each other. Fluorescent labelling is often used for this purpose. It was decided for this work to use confocal fluorescence microscopy (Leica TCS SP8 X). The advantage of this technique is that it allows for the possibility of 3D imaging, while modern microscopic software allows the establishment of long-term experiments. The main problems with long-term studies of living cells and necessary conditions are discussed in Chapter 4.2, which looks at magnification and type of objectives, culture vessels and coatings, culture incubation conditions, fluorescent probes, and the possibilities and limitations of long-term experiments. In this work, the confocal microscope was equipped with a stage top incubator (the Stage Top Chamber, OKOLAB) to provide the culture conditions necessary for long-term experiments.

There is a wide range of fluorescent dyes available, but only a small number of dyes are suitable for long-term cell observation. Usually, the choice of dyes is based on their long-term stability, non-toxicity, method of interaction with biological samples, and excitation and emission spectra. The use of fluorescent dyes in terms of suitability for long-term imaging and image processing is discussed in Chapter 5.

SPION are widely used as a cell marker in contemporary research, being applied in many *in vitro* and *in vivo* studies including the field of regenerative medicine. Their properties are affected by their composition, size, and surface coating, and therefore it is very important to study these properties and their interactions with biological samples. This work made use of SAMN-R nanoparticles. It was necessary to study properties such as excitation and emission spectra, stability, and toxicity since these nanoparticles are not a commercial product (being available from the regional centre of advanced technologies and materials, Palacký University, Olomouc). The results of the colocalization analysis are detailed in Chapter 5.1. The experiment confirmed that SAMN-R are mainly to be found in lysosomes and not in cell nuclei. The optimal settings of excitation and emission spectra were described using the Lambda square (λ^2) fluorescence mapping function and it was found that the maximum excitation and emission values of SAMN-R are 560 nm and 581 nm, respectively.

The previous study confirmed that SAMN-R can maintain their colloidal stability in water for at least six months but lose these properties in a cell growth medium because they bind with the proteins contained in the medium. This changes the zeta-potential to lower values and, as a result, nanoparticles form clusters and sediments on the cover of culture vessels and adherent cells. Despite this, SAMN-R can successfully penetrate cell membranes to reach the intracellular compartment. Unfortunately, SPION can promote increases in ROS production, which can exert a toxic effect on living cells. In the previous study, the concentration used was determined in units of mass per volume ($\mu g \cdot mL^{-1}$) but, in this work, it was decided to use the dose parameter of nanoparticles in terms of mass per unit area surface of the culture vessel ($\mu g \cdot cm^{-2}$) since the suspension of SAMN-R does not retain a colloidal state in the culture medium. The results of the study of the toxicity effect of SAMN-R on hMSCs and 3T3 cells are detailed in Chapter 6. It was determined that the dose value of $20\ \mu g \cdot cm^{-2}$ is optimal, and therefore it was used in the following experiments.

Based on the fact that SPION can affect the functions of organelles such as mitochondria and nuclei, it was decided to study their effects on cell proliferation and motility. The 3T3 cell line was used in the study of cell proliferation, while the analysis was performed based on the growth curve obtained. Non-staining cells treated with SAMN-R and CMFDA stained cells were used for this experiment. The subsequent statistical analysis did not confirm that SAMN-R treatment and CMFDA staining exert a significant effect on cell proliferation. The results are shown in detail in Chapter 6.2.

The effects of SAMN-R on collective migration were examined by means of a scratch assay, for which the 3T3 cell line was used. The ability of 3T3 cells to migrate into the wound area was studied, and the results were quantified statistically. It was not confirmed that SAMN-R treatment and CMFDA staining exert a significant effect on collective cell migration. The results can be seen in Chapter 7.1.

Single-cell migration was studied *via* adipose-derived hMSCs taken from eight patients (Chapter 7.2) and the cell migration velocity was compared to non-staining cells treated with SAMN-R and CMFDA stained cells. The duration of the experiments was set to six hours and the frame rate to five and ten minutes. In the first presented experiments, the samples were observed one after the other, after which the conditions of experiments were improved, and samples were observed simultaneously. The statistical analysis did not reveal any significant effect of SAMN-R treatment on single-cell migration velocity, but the difference between the mean velocity of non-staining cells and CMFDA staining cells from one patient were considered statistically significant. The samples gained during this experiment were not observed simultaneously, which could affect the result.

The model employed to study the interactions between hMSCs and HL-1 cardiac muscle cell line as cardiac tissue is detailed in Chapter 8. The scratch assay test was applied here, and two cell lines were cultured separately, after which the ability of hMSCs to migrate toward the HL-1 cell monolayer was observed. The targeted migration of hMSCs toward HL-1 cells was observed and it was seen that hMSCs tend to repair the wound and form a monolayer with HL-1 cells. The hMSCs also formed connections in the form of tunneling nanotubes. These are specific connections that can be used to transfer plasma membrane components, small cytoplasmic molecules, and organelles. This model is appropriate for the study of cell-to-cell contacts and their role in cell repair. This being so, studies of the communication between hMSC and HL-1 cardiac muscle cell line can yield important results for further research in the field of cardiac tissue regeneration.

Based on the results obtained in this work, it can be confirmed that SAMN-R are appropriate cell markers for living cells. In recommended doses for cell treatment, they have proven their stability, non-toxicity, ability to maintain a good fluorescent signal for a long time, and ability to transfer into daughter cells. It can be confirmed that SAMN-R are suitable cell markers for tissue regeneration research. The set goals of this work were achieved, and the results obtained have great potential for further research in this field.

The image processing algorithms that were used to perform the quantitative analysis of the cell proliferation and migration studies are detailed in Chapter 5.2. The statistical analyses and image processing were performed using the MATLAB (The MathWorks, Inc.) computing environment.

The main results can be found in [141], while the other significant results have been published in [24, 32, 88, 145, 176]. Given the above findings, it could be concluded that all the main objectives of this thesis have been met.

REFERENCES

[1] FITZSIMMONS, Ross E. B., Matthew S. MAZUREK, Agnes SOOS a Craig A. SIMMONS. Mesenchymal stromal/stem cells in regenerative medicine and tissue engineering. *Stem Cells International* [online]. 2018, **2018**, 1–16. ISSN 1687-966X. DOI:10.1155/2018/8031718

[2] HAN, Yu, Xuezhou LI, Yanbo ZHANG, Yuping HAN, Fei CHANG a Jianxun DING. Mesenchymal stem cells for regenerative medicine. *Cells* [online]. 2019, **8**(8), 886. ISSN 2073-4409. DOI:10.3390/cells8080886

[3] IKEGAME, Yuka, Kentaro YAMASHITA, Shin-Ichiro HAYASHI, Hiroshi MIZUNO, Masahiro TAWADA, Fukka YOU, Kiyofumi YAMADA, Yoshitaka TANAKA, Yusuke EGASHIRA, Shigeru NAKASHIMA, Shin-Ichi YOSHIMURA a Toru IWAMA. Comparison of mesenchymal stem cells from adipose tissue and bone marrow for ischemic stroke therapy. *Cytotherapy* [online]. 2011, **13**(6), 675–685. ISSN 14653249. DOI:10.3109/14653249.2010.549122

[4] FAN, Xing-Liang, Yuelin ZHANG, Xin LI a Qing-Ling FU. Mechanisms underlying the protective effects of mesenchymal stem cell-based therapy. *Cellular and Molecular Life Sciences* [online]. 2020, **77**(14), 2771–2794. ISSN 1420-682X. DOI:10.1007/s00018-020-03454-6

[5] BARBA, Marta, Claudia CICIONE, Camilla BERNARDINI, Fabrizio MICHETTI a Wanda LATTANZI. Adipose-derived mesenchymal cells for bone regereneration: state of the art. *BioMed Research International* [online]. 2013, **2013**, 1–11. ISSN 2314-6133. DOI:10.1155/2013/416391

[6] JONES, Elena a Xuebin YANG. Mesenchymal stem cells and bone regeneration: Current status. *Injury* [online]. 2011, **42**(6), 562–568. ISSN 00201383. DOI:10.1016/j.injury.2011.03.030

[7] TALÉNS-VISCONTI, Raquel. Hepatogenic differentiation of human mesenchymal stem cells from adipose tissue in comparison with bone marrow mesenchymal stem cells. *World Journal of Gastroenterology* [online]. 2006, **12**(36), 5834. ISSN 1007-9327. DOI:10.3748/wjg.v12.i36.5834

[8] BANAS, Agnieszka, Takumi TERATANI, Yusuke YAMAMOTO, Makoto TOKUHARA, Fumitaka TAKESHITA, Mitsuhiko OSAKI, Takashi KATO, Hitoshi OKOCHI a Takahiro OCHIYA. Rapid hepatic fate specification of adipose-derived stem cells and their therapeutic potential for liver failure. *Journal of Gastroenterology and Hepatology* [online]. 2009, **24**(1), 70–77. ISSN 08159319. DOI:10.1111/j.1440-1746.2008.05496.x

[9] MAJKA, Marcin, Maciej SUŁKOWSKI, Bogna BADYRA a Piotr MUSIAŁEK. Concise review: Mesenchymal stem cells in cardiovascular regeneration: Emerging research directions and clinical applications. *STEM CELLS Translational Medicine* [online]. 2017, **6**(10), 1859–1867. ISSN 21576564. DOI:10.1002/sctm.16-0484

[10] KURAITIS, Drew, Marc RUEL a Erik J. SUURONEN. Mesenchymal stem cells for cardiovascular regeneration. *Cardiovascular Drugs and Therapy* [online]. 2011, **25**(4), 349–362. ISSN 0920-3206. DOI:10.1007/s10557-011-6311-y

[11] YANG, Mei, Qingfeng LI, Lingling SHENG, Hua LI, Rui WENG a Tao ZAN. Bone marrow–derived mesenchymal stem cells transplantation accelerates tissue expansion by promoting skin regeneration during expansion. *Annals of Surgery* [online]. 2011, **253**(1), 202–209. ISSN 0003-4932. DOI:10.1097/SLA.0b013e3181f9ba1ah

[12] SHOKRGOZAR, Mohammad Ali, Maryam FATTAHI, Shahin BONAKDAR, Iraj Ragerdi KASHANI, Mohammad MAJIDI, Nooshin HAGHIGHIPOUR, Vahid BAYATI, Hassan SANATI a Seyyed Nasirolddin SAEEDI. Healing potential of mesenchymal stem cells cultured on a collagen-based scaffold for skin regeneration. *Iranian biomedical journal* [online]. 2012, **16**(2), 68–76. DOI:10.6091/ibj.1053.2012

[13] HAN, Sufang, Bin WANG, Xing LI, Zhifeng XIAO, Jin HAN, Yannan ZHAO, Yongxiang FANG, Yanyun YIN, Bing CHEN a Jianwu DAI. Bone marrow-derived mesenchymal stem cells in three-dimensional culture promote neuronal regeneration by neurotrophic protection and immunomodulation. *Journal of Biomedical Materials Research Part A* [online]. 2016, **104**(7), 1759–1769. ISSN 15493296. DOI:10.1002/jbm.a.35708

[14] DI SUMMA, P.G., P.J. KINGHAM, W. RAFFOUL, M. WIBERG, G. TERENGHI a D.F. KALBERMATTEN. Adipose-derived stem cells enhance peripheral nerve regeneration. *Journal of Plastic, Reconstructive & Aesthetic Surgery* [online]. 2010, **63**(9), 1544–1552. ISSN 17486815. DOI:10.1016/j.bjps.2009.09.012

[15] VINARDELL, T., S. D. THORPE, C. T. BUCKLEY a D. J. KELLY. Chondrogenesis and integration of mesenchymal stem cells within an in vitro cartilage defect repair model. *Annals of Biomedical Engineering* [online]. 2009, **37**(12), 2556–2565. ISSN 0090-6964. DOI:10.1007/s10439-009-9791-1

[16] FELLOWS, Christopher R., Csaba MATTA, Roza ZAKANY, Ilyas M. KHAN a Ali MOBASHERI. Adipose, bone marrow and synovial joint-derived mesenchymal stem cells for cartilage repair. *Frontiers in Genetics* [online]. 2016, **7**. ISSN 1664-8021. DOI:10.3389/fgene.2016.00213

[17] DEMIRAYAK, Bengi, Nurşen YÜKSEL, Onur Sinan ÇELIK, Cansu SUBAŞI, Gökhan DURUKSU, Z. Seda UNAL, Demir Kürşat YILDIZ a Erdal KARAÖZ. Effect of bone marrow and adipose tissue-derived mesenchymal stem cells on the natural course of corneal scarring after penetrating injury. *Experimental Eye Research* [online]. 2016, **151**, 227–235. ISSN 00144835. DOI:10.1016/j.exer.2016.08.011

[18] BANDEIRA, Francisco, Tze-Wei GOH, Melina SETIAWAN, Gary Hin-Fai YAM a Jodhbir S. MEHTA. Cellular therapy of corneal epithelial defect by adipose mesenchymal stem cell-derived epithelial progenitors. *Stem Cell Research & Therapy* [online]. 2020, **11**(1), 14. ISSN 1757-6512. DOI:10.1186/s13287-019-1533-1

[19] BAE, Sang-Woo, Kang-Woog LEE, Jae-Hyun PARK, JunHee LEE, Cho-Rok JUNG, JunJie YU, Hwi-Yool KIM a Dae-Hyun KIM. 3D bioprinted artificial trachea with epithelial cells and chondrogenic-differentiated bone marrow-derived mesenchymal stem cells. *International Journal of Molecular Sciences* [online]. 2018, **19**(6), 1624. ISSN 1422-0067. DOI:10.3390/ijms19061624

[20] SHIN, Yoo Seob, Jae Won CHOI, Ju-Kyeong PARK, Yoo Suk KIM, Soon Sim YANG, Byoung-Hyun MIN a Chul-Ho KIM. Tissue-engineered tracheal reconstruction using mesenchymal stem cells seeded on a porcine cartilage powder scaffold. *Annals of Biomedical Engineering* [online]. 2015, **43**(4), 1003–1013. ISSN 0090-6964. DOI:10.1007/s10439-014-1126-1

[21] KOLLAR, Katarina, Matthew M. COOK, Kerry ATKINSON a Gary BROOKE. Molecular mechanisms involved in mesenchymal stem cell migration to the site of acute myocardial infarction. *International Journal of Cell Biology* [online]. 2009, **2009**, 1–8. ISSN 1687-8876. DOI:10.1155/2009/904682

[22] WU, Yaojiong a Robert C. H. ZHAO. The role of chemokines in mesenchymal stem cell homing to myocardium. *Stem Cell Reviews and Reports* [online]. 2012, **8**(1), 243–250. ISSN 1550-8943. DOI:10.1007/s12015-011-9293-z

[23] WEN, Zhuzhi, Shaoxin ZHENG, Changqing ZHOU, Jingfeng WANG a Tong WANG. Repair mechanisms of bone marrow mesenchymal stem cells in myocardial infarction. *Journal of Cellular and Molecular Medicine* [online]. 2011, **15**(5), 1032–1043. ISSN 15821838. DOI:10.1111/j.1582-4934.2010.01255.x

[24] BAIAZITOVA, Larisa, Josef SKOPALIK, Vratislav CMIEL, Jiri CHMELIK, Ondrej SVOBODA a Ivo PROVAZNIK. Modern semi-automatic set-up for testing cell migration with impact for therapy of myocardial infarction. In: *World Congress on Medical Physics and Biomedical Engineering 2018* [online]. 68/3. Singapore: IFMBE Proceedings, 2019, s. 155–159. ISBN 978-981-10-9022-6. DOI:10.1007/978-981-10-9023-3_28

[25] PARK, Siwan, Hwanseok JANG, Byung Soo KIM, Changmo HWANG, Gi Seok JEONG a Yongdoo PARK. Directional migration of mesenchymal stem cells under an SDF-1α gradient on a microfluidic device. *PLOS ONE* [online]. 2017, **12**(9), e0184595. ISSN 1932-6203. DOI:10.1371/journal.pone.0184595

[26] CAI, Anping, Ruofeng QIU, Liwen LI, Dongdan ZHENG, Yugang DONG, Danqing YU, Yuli HUANG, Shaoqi RAO, Yingling ZHOU a Weiyi MAI. Atorvastatin treatment of rats with ischemia-reperfusion injury improves adipose-derived mesenchymal stem cell migration and survival via the SDF-1α/CXCR-4 axis. *PLoS ONE* [online]. 2013, **8**(12), e79100. ISSN 1932-6203. DOI:10.1371/journal.pone.0079100

[27] HUANG, Congxin. Differentiation potential of human mesenchymal stem cells derived from adipose tissue and bone marrow to sinus node-like cells. *Molecular Medicine Reports* [online]. 2011, 108–113. ISSN 1791-2997. DOI:10.3892/mmr.2011.611

[28] XU, Wenrong, Xiran ZHANG, Hui QIAN, Wei ZHU, Xiaochun SUN, Jiabo HU, Hong ZHOU a Yongchang CHEN. Mesenchymal stern cells from adult human bone marrow differentiate into a cardiomyocyte phenotype in vitro. *Experimental Biology and Medicine* [online]. 2004, **229**(7), 623–631. ISSN 1535-3702. DOI:10.1177/153537020422900706

[29] RANGAPPA, Sunil, Chen FEN, Eng Hin LEE, Ariff BONGSO a Eugene Sim Kwang WEI. Transformation of adult mesenchymal stem cells isolated from the fatty tissue into cardiomyocytes. *The Annals of Thoracic Surgery* [online]. 2003, **75**(3), 775–779. ISSN 00034975. DOI:10.1016/S0003-4975(02)04568-X

[30] TOMITA, Shinji, R.-K. LI, Richard D. WEISEL, Donald A. G. MICKLE, E.-J. KIM, Tetsuro SAKAI a Z.-Q. JIA. Autologous transplantation of bone marrow cells improves damaged heart function. *Circulation* [online]. 1999, **100**(Supplement 2), 247–256. ISSN 0009-7322. DOI:10.1161/01.CIR.100.suppl_2.II-247

[31] MIKLÍKOVÁ, M., D. JARKOVSKÁ, M. ČEDÍKOVÁ, J. ŠVÍGLEROVÁ, J. KUNCOVÁ, L. NALOS, T. KUBÍKOVÁ, V. LIŠKA, M. HOLUBOVÁ, D. LYSÁK, M. KRÁLÍČKOVÁ, L. VIŠTEJNOVÁ a M. ŠTENGL. Beneficial effects of mesenchymal stem cells on adult porcine cardiomyocytes in non-contact co-culture. *Physiological Research* [online]. 2018, S619–S631. ISSN 1802-9973. DOI:10.33549/physiolres.934051

[32] BAIAZITOVA, Larisa, Josef SKOPALIK, Vratislav CMIEL, Jiri CHMELIK, Ondrej SVOBODA, Zdenka FOHLEROVA, Jaromir HUBALEK a Ivo PROVAZNIK. Characterization of cells migration through cardiac tissue using advanced microscopy techniques and matlab simulation. In: *2015 Computing in Cardiology Conference (CinC)* [online]. B.m.: IEEE, 2015, s. 1125–1128. ISBN 978-1-5090-0685-4. DOI:10.1109/CIC.2015.7411113

[33] PLOTNIKOV, E. Y., T. G. KHRYAPENKOVA, A. K. VASILEVA, M. V. MAREY, S. I. GALKINA, N. K. ISAEV, E. V. SHEVAL, V. Y. POLYAKOV, G. T. SUKHIKH a D. B. ZOROV. Cell-to-cell cross-talk between mesenchymal stem cells and cardiomyocytes in co-culture. *Journal of Cellular and Molecular Medicine* [online]. 2008, **12**(5a), 1622–1631. ISSN 15821838. DOI:10.1111/j.1582-4934.2007.00205.x

[34] ORLIC, Donald, Jan KAJSTURA, Stefano CHIMENTI, David M. BODINE, Annarosa LERI a Piero ANVERSA. Bone marrow stem cells regenerate infarcted myocardium. *Pediatric Transplantation* [online]. 2003, **7**, 86–88. ISSN 13973142. DOI:10.1034/j.1399-3046.7.s3.13.x

[35] ORLIC, D., J. KAJSTURA, S. CHIMENTI, F. LIMANA, I. JAKONIUK, F. QUAINI, B. NADAL-GINARD, D. M. BODINE, A. LERI a P. ANVERSA. Mobilized bone marrow cells repair the infarcted heart, improving function and survival. *Proceedings of the National Academy of Sciences* [online]. 2001, **98**(18), 10344–10349. ISSN 0027-8424. DOI:10.1073/pnas.181177898

[36] PEREZ-ESTENAGA, Inigo, Felipe PROSPER a Beatriz PELACHO. Allogeneic mesenchymal stem cells and biomaterials: The perfect match for cardiac repair? *International Journal of Molecular Sciences* [online]. 2018, **19**(10), 3236. ISSN 1422-0067. DOI:10.3390/ijms19103236

[37] HU, Xinyang, Jianan WANG, Jie CHEN, Ronghua LUO, Aina HE, Xiaojie XIE a Jiahui LI. Optimal temporal delivery of bone marrow mesenchymal stem cells in rats with myocardial infarction. *European Journal of Cardio-Thoracic Surgery* [online]. 2007, **31**(3), 438–443. ISSN 10107940. DOI:10.1016/j.ejcts.2006.11.057

[38] SWIJNENBURG, Rutger-Jan, Johannes A. GOVAERT, Koen E.A. VAN DER BOGT, Jeremy I. PEARL, Mei HUANG, William STEIN, Grant HOYT, Hannes VOGEL, Christopher H. CONTAG, Robert C. ROBBINS a Joseph C. WU. Timing of bone marrow cell delivery has minimal effects on cell viability and cardiac recovery after myocardial infarction. *Circulation: Cardiovascular Imaging* [online]. 2010, **3**(1), 77–85. ISSN 1941-9651. DOI:10.1161/CIRCIMAGING.109.872085

[39] MIAS, Celine, Olivier LAIREZ, Elodie TROUCHE, Jerome RONCALLI, Denis CALISE, Marie-Helene SEGUELAS, Catherine ORDENER, Marie-Dominique PIERCECCHI-MARTI, Nathalie AUGE, Anne Negre SALVAYRE, Philippe BOURIN, Angelo PARINI a Daniel CUSSAC. Mesenchymal stem cells promote matrix metalloproteinase secretion by cardiac fibroblasts and reduce cardiac ventricular fibrosis after myocardial infarction. *Stem Cells* [online]. 2009, **27**(11), 2734–2743. ISSN 10665099. DOI:10.1002/stem.169

[40] LAZENNEC, Gwendal a Christian JORGENSEN. Concise review: Adult multipotent stromal cells and cancer: Risk or benefit? *Stem Cells* [online]. 2008, **26**(6), 1387–1394. ISSN 10665099. DOI:10.1634/stemcells.2007-1006

[41] SATIJA, Neeraj Kumar, Vimal Kishor SINGH, Yogesh Kumar VERMA, Pallavi GUPTA, Shilpa SHARMA, Farhat AFRIN, Menka SHARMA, Pratibha SHARMA, R. P. TRIPATHI a G. U. GURUDUTTA. Mesenchymal stem cell-based therapy: a new paradigm in regenerative medicine. *Journal of Cellular and Molecular Medicine* [online]. 2009, **13**(11–12), 4385–4402. ISSN 15821838. DOI:10.1111/j.1582-4934.2009.00857.x

[42] CHAUDHURI, Rusha, Madhumitha RAMACHANDRAN, Pearl MOHARIL, Megha HARUMALANI a Amit K. JAISWAL. Biomaterials and cells for cardiac tissue engineering: Current choices. *Materials Science and Engineering: C* [online]. 2017, **79**, 950–957. ISSN 09284931. DOI:10.1016/j.msec.2017.05.121

[43] SONG, Young Hye, Seung Hee SHON, Mengrou SHAN, Abraham D STROOCK a Claudia FISCHBACH. Adipose-derived stem cells increase angiogenesis through matrix metalloproteinase-dependent collagen remodeling. *Integrative Biology* [online]. 2016, **8**(2), 205–215. ISSN 1757-9694. DOI:10.1039/C5IB00277J

[44] QASIM, Muhammad, Farhan HAQ, Min Hee KANG a Jin Hoi KIM. 3D printing approaches for cardiac tissue engineering and role of immune modulation in tissue regeneration. *International Journal of Nanomedicine* [online]. 2019, **Volume 14**, 1311–1333. ISSN 1178-2013. DOI:10.2147/IJN.S189587

[45] KEDZIOREK, Dorota A. a Dara L. KRAITCHMAN. Superparamagnetic iron oxide labeling of stem cells for MRI tracking and delivery in cardiovascular disease. In: *Methods in Molecular Biology* [online]. 2010, s. 171–183. DOI:10.1007/978-1-60761-705-1_11

[46] YILMAZ, Ali, Sabine RÖSCH, Handan YILDIZ, Siegfried KLUMPP a Udo SECHTEM. First multiparametric cardiovascular magnetic resonance study using ultrasmall superparamagnetic iron oxide nanoparticles in a patient with acute myocardial infarction. *Circulation* [online]. 2012, **126**(15), 1932–1934. ISSN 0009-7322. DOI:10.1161/CIRCULATIONAHA.112.108167

[47] DADFAR, Seyed Mohammadali, Karolin ROEMHILD, Natascha I. DRUDE, Saskia VON STILLFRIED, Ruth KNÜCHEL, Fabian KIESSLING a Twan LAMMERS. Iron oxide nanoparticles: Diagnostic, therapeutic and theranostic applications. *Advanced Drug Delivery Reviews* [online]. 2019, **138**, 302–325. ISSN 0169409X. DOI:10.1016/j.addr.2019.01.005

[48] ITTRICH, H., K. PELDSCHUS, N. RAABE, M. KAUL a G. ADAM. Superparamagnetic iron oxide nanoparticles in biomedicine: applications and developments in diagnostics and therapy. *RöFo - Fortschritte auf dem Gebiet der Röntgenstrahlen und der bildgebenden Verfahren* [online]. 2013, **185**(12), 1149–1166. ISSN 1438-9029. DOI:10.1055/s-0033-1335438

[49] VANGIJZEGEM, Thomas, Dimitri STANICKI a Sophie LAURENT. Magnetic iron oxide nanoparticles for drug delivery: applications and characteristics. *Expert Opinion on Drug Delivery* [online]. 2019, **16**(1), 69–78. ISSN 1742-5247. DOI:10.1080/17425247.2019.1554647

[50] PENG, Xiang-Hong, Ximei QIAN, Hui MAO, Andrew Y WANG, Zhuo (Georgia) CHEN, Shuming NIE a Dong M SHIN. Targeted magnetic iron oxide nanoparticles for tumor imaging and therapy. *International Journal of Nanomedicine* [online]. 2008, **3**(3), 311–321. ISSN 1178-2013. DOI:10.2147/IJN.S2824

[51] KIEVIT, Forrest M. a Miqin ZHANG. Surface engineering of iron oxide nanoparticles for targeted cancer therapy. *Accounts of Chemical Research* [online]. 2011, **44**(10), 853–862. ISSN 0001-4842. DOI:10.1021/ar2000277

[52] CHERAGHIPOUR, Elham, Sirus JAVADPOUR a Ali Reza MEHDIZADEH. Citrate capped superparamagnetic iron oxide nanoparticles used for hyperthermia therapy. *Journal of Biomedical Science and Engineering* [online]. 2012, **05**(12), 715–719. ISSN 1937-6871. DOI:10.4236/jbise.2012.512089

[53] BIETENBECK, Michael, Anca FLORIAN, Cornelius FABER, Udo SECHTEM a Ali YILMAZ. Remote magnetic targeting of iron oxide nanoparticles for cardiovascular diagnosis and therapeutic drug delivery: where are we now? *International Journal of Nanomedicine* [online]. 2016, **Volume 11**, 3191–3203. ISSN 1178-2013. DOI:10.2147/IJN.S110542

[54] QIAO, Ruirui, Chunhui YANG a Mingyuan GAO. Superparamagnetic iron oxide nanoparticles: from preparations to in vivo MRI applications. *Journal of Materials Chemistry* [online]. 2009, **19**(35), 6274. ISSN 0959-9428. DOI:10.1039/b902394a

[55] CHELLURI, Lakshmi Kiran, Vinod Kumar VERMA, Suguna Ratnakar KAMARAJU, Ravindranath KANCHERLA, Lakshmi K KONA, Syed Sultan BEEVI, Tanya DEBNATH, P USHA SHALINI, Syed Ali ARBAB a Ram Mohan VADAPALLI. Fluorescent magnetic iron oxide nanoparticles for cardiac precursor cell selection from stromal vascular fraction and optimization for magnetic resonance imaging. *International Journal of Nanomedicine* [online]. 2015, **10**, 711–726. ISSN 1178-2013. DOI:10.2147/IJN.S75445

[56] REDDY, L. Harivardhan, José L. ARIAS, Julien NICOLAS a Patrick COUVREUR. Magnetic nanoparticles: Design and characterization, toxicity and biocompatibility, pharmaceutical and biomedical applications. *Chemical Reviews* [online]. 2012, **112**(11), 5818–5878. ISSN 0009-2665. DOI:10.1021/cr300068p

[57] MARKIDES, H., M. ROTHERHAM a A. J. EL HAJ. Biocompatibility and toxicity of magnetic nanoparticles in regenerative medicine. *Journal of Nanomaterials* [online]. 2012, **2012**, 1–11. ISSN 1687-4110. DOI:10.1155/2012/614094

[58] HAVRDOVA, M., K. POLAKOVA, J. SKOPALIK, M. VUJTEK, A. MOKDAD, M. HOMOLKOVA, J. TUCEK, J. NEBESAROVA a R. ZBORIL. Field emission scanning electron microscopy (FE-SEM) as an approach for nanoparticle detection inside cells. *Micron* [online]. 2014, **67**, 149–154. ISSN 09684328. DOI:10.1016/j.micron.2014.08.001

[59] SVATKOVA, Marketa, Katerina POLAKOVA, Josef SKOPALIK, Vitezslav BREZINA, Jana NEBESAROVA a Radek ZBORIL. Live in vitro monitoring of stem cell labeling process by SPIO nanoparticles using advanced microscopic techniques. In: *CONFERENCE PROCEEDINGS - NANOCON 2012*. 2012, s. 1–7.

[60] SKOPALIK, Josef, Katerina POLAKOVA, Marketa HAVRDOVA, Ivan JUSTAN, Massimiliano MAGRO, David MILDE, Lucia KNOPFOVA, Jan SMARDA, Helena POLAKOVA, Eva GABRIELOVA, Fabio VIANELLO, Jaroslav MICHALEK a Radek ZBORIL. Mesenchymal stromal cell labeling by new uncoated superparamagnetic maghemite nanoparticles in comparison with commercial Resovist &ndash; an initial in vitro study. *International Journal of Nanomedicine* [online]. 2014, **9**, 5355–5372. ISSN 1178-2013. DOI:10.2147/IJN.S66986

[61] CMIEL, Vratislav, Josef SKOPALIK, Katerina POLAKOVA, Jan SOLAR, Marketa HAVRDOVA, David MILDE, Ivan JUSTAN, Massimiliano MAGRO, Zenon STARCUK a Ivo PROVAZNIK. Rhodamine bound maghemite as a long-term dual imaging nanoprobe of adipose tissue-derived mesenchymal stromal cells. *European Biophysics Journal* [online]. 2017, **46**(5), 433–444. ISSN 0175-7571. DOI:10.1007/s00249-016-1187-1

[62] MURPHY, Douglas B. *Fundamentals of light microscopy and electronic imaging*. New York: Wiley-Liss: A JOHN WILEY & SONS, INC., PUBLICATION, 2001. ISBN 04-712-5391-X.

[63] Fluorescent probes. *Thermo Fisher Scientific* [online]. [vid. 2020-09-04]. Dostupné z: https://www.thermofisher.com/cz/en/home/life-science/protein-biology/protein-biology-learning-center/protein-biology-resource-library/pierce-protein-methods/fluorescent-probes.html

[64] ABDELLAH, Marwan, Ahmet BILGILI, Stefan EILEMANN, Henry MARKRAM a Felix SCHÜRMANN. A physically plausible model for rendering highly scattering fluorescent participating media [online]. 2017. Dostupné z: http://arxiv.org/abs/1706.03024

[65] WILSON, Martin. Introduction to widefield microscopy. *Leica Microsystems* [online]. 2017. Dostupné z: https://www.leica-microsystems.com/science-lab/introduction-to-widefield-microscopy/

[66] *If imaging: Widefield versus confocal microscopy* [online]. 2019 [vid. 2021-05-26]. Dostupné z: https://www.ptglab.com/news/blog/if-imaging-widefield-versus-confocal-microscopy/

[67] ISHIKAWA-ANKERHOLD, Hellen C., Richard ANKERHOLD a Gregor P. C. DRUMMEN. Advanced fluorescence microscopy techniques—FRAP, FLIP, FLAP, FRET and FLIM. *Molecules* [online]. 2012, **17**(4), 4047–4132. ISSN 1420-3049. DOI:10.3390/molecules17044047

[68] BORLINGHAUS, R. Th. The white confocal. *The European Physical Journal Plus* [online]. 2012, **127**(10), 1–9. ISSN 2190-5444. DOI:10.1140/epjp/i2012-12131-x

[69] BORLINGHAUS, Rolf T a Lioba KUSCHEL. White light laser: The ultimate source for confocal microscopy. *Leica Microsystems* [online]. 2012 [vid. 2021-05-26]. Dostupné z: https://www.leica-microsystems.com/science-lab/white-light-laser/

[70] BIRK, Holger, Johann ENGELHARDT, Rafael STORZ, Nicole HARTMANN, Joachim BRADL a Heinrich ULRICH. Programmable beam-splitter for confocal laser scanning microscopy. *Proc. SPIE 4621, Three-Dimensional and Multidimensional Microscopy: Image Acquisition and Processing IX* [online]. 2002, 1–12. DOI:10.1117/12.467841

[71] BORLINGHAUS, Rolf T. What is a Spectral Detector (SP Detector)?: Technology of SP8 confocal microscope. *Leica Microsystems* [online]. 2019 [vid. 2020-11-07]. Dostupné z: https://www.leica-microsystems.com/science-lab/what-is-a-spectral-detector-sp-detector/

[72] BORLINGHAUS, Rolf T. Spectral detection – how to define the spectral bands that collect probe-specific emission. *Leica Microsystems* [online]. 2013 [vid. 2020-11-07]. Dostupné z: https://www.leica-microsystems.com/science-lab/spectral-detection-how-to-define-the-spectral-bands-that-collect-probe-specific-emission/

[73] HELL, Stefan W. a Jan WICHMANN. Breaking the diffraction resolution limit by stimulated emission: stimulated-emission-depletion fluorescence microscopy. *Optics Letters* [online]. 1994, **19**(11), 780. ISSN 0146-9592. DOI:10.1364/OL.19.000780

[74] RUST, Michael J, Mark BATES a Xiaowei ZHUANG. Sub-diffraction-limit imaging by stochastic optical reconstruction microscopy (STORM). *Nature Methods* [online]. 2006, **3**(10), 793–796. ISSN 1548-7091. DOI:10.1038/nmeth929

[75] BETZIG, E., G. H. PATTERSON, R. SOUGRAT, O. W. LINDWASSER, S. OLENYCH, J. S. BONIFACINO, M. W. DAVIDSON, J. LIPPINCOTT-SCHWARTZ a H. F. HESS. Imaging intracellular fluorescent proteins at nanometer resolution. *Science* [online]. 2006, **313**(5793), 1642–1645. ISSN 0036-8075. DOI:10.1126/science.1127344

[76] HESS, Samuel T., Thanu P.K. GIRIRAJAN a Michael D. MASON. Ultra-high resolution imaging by fluorescence photoactivation localization microscopy. *Biophysical Journal* [online]. 2006, **91**(11), 4258–4272. ISSN 00063495. DOI:10.1529/biophysj.106.091116

[77] HUANG, Bo, Min WU, Wenqin WANG, Pietro DE CAMILLI a Xiaowei ZHUANG. Three-dimensional super-resolution fluorescence microscopy and its application to clathrin mediated endocytosis. *Biophysical Journal* [online]. 2009, **96**(3), 16a. ISSN 00063495. DOI:10.1016/j.bpj.2008.12.987

[78] SCHUMACHER, Jan a Louise BERTRAND. THUNDER technology note. *Leica Microsystems* [online]. 2019 [vid. 2020-11-02]. Dostupné z: https://www.leica-microsystems.com/index.php?id=24637

[79] GAO, Liang, Liren ZHU, Chiye LI a Lihong V. WANG. Nonlinear light-sheet fluorescence microscopy by photobleaching imprinting. *Journal of The Royal Society Interface* [online]. 2014, **11**(93), 20130851. ISSN 1742-5689. DOI:10.1098/rsif.2013.0851

[80] DONAHUE, Nathan D., Handan ACAR a Stefan WILHELM. Concepts of nanoparticle cellular uptake, intracellular trafficking, and kinetics in nanomedicine. *Advanced Drug Delivery Reviews* [online]. 2019, **143**, 68–96. ISSN 0169409X. DOI:10.1016/j.addr.2019.04.008

[81] SCHWAMINGER, S. P., D. BAUER, P. FRAGA-GARCÍA, F. E. WAGNER a S. BERENSMEIER. Oxidation of magnetite nanoparticles: Impact on surface and crystal properties. *CrystEngComm* [online]. 2017, **19**(2), 246–255. ISSN 1466-8033. DOI:10.1039/C6CE02421A

[82] BULTE, Jeff W. M., Piotr WALCZAK, Bernhard GLEICH, Jürgen WEIZENECKER, Denis E. MARKOV, Hans C. J. AERTS, Hans BOEVE, Jörn BORGERT a Michael KUHN. MPI cell tracking: what can we learn from MRI? In: John B. WEAVER a Robert C. MOLTHEN, ed. *Medical Imaging 2011: Biomedical Applications in Molecular, Structural, and Functional Imaging* [online]. 2011, s. 79650Z. DOI:10.1117/12.879844

[83] RAMASWAMY, Sharan, Jane B. GRECO, Mehmet C. ULUER, Zijun ZHANG, Zhuoli ZHANG, Kenneth W. FISHBEIN a Richard G. SPENCER. Magnetic resonance imaging of chondrocytes labeled with superparamagnetic iron oxide nanoparticles in tissue-engineered cartilage. *Tissue Engineering Part A* [online]. 2009, **15**(12), 3899–3910. ISSN 1937-3341. DOI:10.1089/ten.tea.2008.0677

[84] KYRTATOS, Panagiotis G., Pauliina LEHTOLAINEN, Manfred JUNEMANN-RAMIREZ, Ana GARCIA-PRIETO, Anthony N. PRICE, John F. MARTIN, David G. GADIAN, Quentin A. PANKHURST a Mark F. LYTHGOE. Magnetic tagging increases delivery of circulating progenitors in vascular injury. *JACC: Cardiovascular Interventions* [online]. 2009, **2**(8), 794–802. ISSN 19368798. DOI:10.1016/j.jcin.2009.05.014

[85] CHAHAL, P, Y DUROCHER a A KAMEN. Cell transfection. 2011.

[86] DOBSON, J. Gene therapy progress and prospects: magnetic nanoparticle-based gene delivery. *Gene Therapy* [online]. 2006, **13**(4), 283–287. ISSN 0969-7128. DOI:10.1038/sj.gt.3302720

[87] JINTURKAR, Kaustubh A., Mohan N. RATHI a Ambikanandan MISRA. Gene delivery using physical methods. In: *Challenges in Delivery of Therapeutic Genomics and Proteomics* [online]. B.m.: Elsevier, 2011, s. 83–126. DOI:10.1016/B978-0-12-384964-9.00003-7

[88] SVOBODA, Ondrej, Josef SKOPALIK, Larisa BAIAZITOVA, Vratislav CMIEL, Tomas POTOCNAK, Ivo PROVAZNIK, Zdenka FOHLEROVA a Jaromir HUBALEK. DNA intracellular delivery into 3T3 cell line using fluorescence magnetic ferumoxide nanoparticles. In: *IFMBE Proceedings* [online]. Singapore: Springer Singapore, 2019, s. 149–153. ISBN 978-981-10-9022-6. DOI:10.1007/978-981-10-9023-3_27

[89] GOODWIN, Tyler a Leaf HUANG. *Nonviral vectors. we have come a long way* [online]. B.m.: Elsevier, 2014. ISBN 9780128001486. DOI:10.1016/B978-0-12-800148-6.00001-8

[90] DURÁN, María Carolina, Saskia WILLENBROCK, Annette BARCHANSKI, Jessika-M V MÜLLER, Arianna MAIOLINI, Jan T SOLLER, Stephan BARCIKOWSKI, Ingo NOLTE, Karsten FEIGE a Hugo MURUA ESCOBAR. Comparison of nanoparticle-mediated transfection methods for DNA expression plasmids: efficiency and cytotoxicity. *Journal of Nanobiotechnology* [online]. 2011, **9**(1), 47. ISSN 1477-3155. DOI:10.1186/1477-3155-9-47

[91] VENERANDO, Rina, Giovanni MIOTTO, Massimiliano MAGRO, Marco DALLAN, Davide BARATELLA, Emanuela BONAIUTO, Radek ZBORIL a Fabio VIANELLO. Magnetic nanoparticles with covalently bound self-assembled protein corona for advanced biomedical applications. *The Journal of Physical Chemistry C* [online]. 2013, **117**(39), 20320–20331. ISSN 1932-7447. DOI:10.1021/jp4068137

[92] MAGRO, Massimiliano, Giulietta SINIGAGLIA, Luca NODARI, Jiri TUCEK, Katerina POLAKOVA, Zdenek MARUSAK, Sara CARDILLO, Gabriella SALVIULO, Umberto RUSSO, Roberto STEVANATO, Radek ZBORIL a Fabio VIANELLO. Charge binding of rhodamine derivative to OH− stabilized nanomaghemite: Universal nanocarrier for construction of magnetofluorescent biosensors. *Acta Biomaterialia* [online]. 2012, **8**(6), 2068–2076. ISSN 17427061. DOI:10.1016/j.actbio.2012.02.005

[93] XIAO, Yufen a Jianzhong DU. Superparamagnetic nanoparticles for biomedical applications. *Journal of Materials Chemistry B* [online]. 2020, **8**(3), 354–367. ISSN 2050-750X. DOI:10.1039/C9TB01955C

[94] TALAIE, Tara, Stephen J.P. PRATT, Camilo VANEGAS, Su XU, R. Frank HENN, Paul YAROWSKY a Richard M. LOVERING. Site-specific targeting of platelet-rich plasma via superparamagnetic nanoparticles. *Orthopaedic Journal of Sports Medicine* [online]. 2015, **3**(1), 232596711456618. ISSN 2325-9671. DOI:10.1177/2325967114566185

[95] HUANG, Gang, Huabing CHEN, Ying DONG, Xiuquan LUO, Haijun YU, Zachary MOORE, Erik A. BEY, David A. BOOTHMAN a Jinming GAO. Superparamagnetic iron oxide nanoparticles: amplifying ROS stress to improve anticancer drug efficacy. *Theranostics* [online]. 2013, **3**(2), 116–126. ISSN 1838-7640. DOI:10.7150/thno.5411

[96] LIMBACH, Ludwig K., Yuchun LI, Robert N. GRASS, Tobias J. BRUNNER, Marcel A. HINTERMANN, Martin MULLER, Detlef GUNTHER a Wendelin J. STARK. Oxide nanoparticle uptake in human lung fibroblasts: Effects of particle size, agglomeration, and diffusion at low concentrations. *Environmental Science & Technology* [online]. 2005, **39**(23), 9370–9376. ISSN 0013-936X. DOI:10.1021/es051043o

[97] ZHAO, Jiacheng a Martina H. STENZEL. Entry of nanoparticles into cells: The importance of nanoparticle properties. *Polymer Chemistry* [online]. 2018, **9**(3), 259–272. ISSN 1759-9954. DOI:10.1039/C7PY01603D

[98] MANZANARES, Dar\'\io a Valent\'\in CEÑA. Endocytosis: the nanoparticle and submicron nanocompounds gateway into the cell. *Pharmaceutics*. 2020, **12**(4), 371.

[99] YAMEEN, Basit, Won Il Il CHOI, Cristian VILOS, Archana SWAMI, Jinjun SHI a Omid C C FAROKHZAD. Insight into nanoparticle cellular uptake and intracellular targeting. *Journal of controlled release*. 2014, **190**, 485–499.

[100] SUMMERS, Huw D., Paul REES, Mark D. HOLTON, M. ROWAN BROWN, Sally C. CHAPPELL, Paul J. SMITH a Rachel J. ERRINGTON. Statistical analysis of nanoparticle dosing in a dynamic cellular system. *Nature Nanotechnology* [online]. 2011, **6**(3), 170–174. ISSN 1748-3387. DOI:10.1038/nnano.2010.277

[101] ZHANG, Sulin, Ju LI, George LYKOTRAFITIS, Gang BAO a Subra SURESH. Size-dependent endocytosis of nanoparticles. *Advanced Materials* [online]. 2009, **21**(4), 419–424. ISSN 09359648. DOI:10.1002/adma.200801393

[102] FIGUEIREDO BORGOGNONI, Camila, Joo Hyoung KIM, Valtencir ZUCOLOTTO, Harald FUCHS a Kristina RIEHEMANN. Human macrophage responses to metal-oxide nanoparticles: a review. *Artificial Cells, Nanomedicine, and Biotechnology* [online]. 2018, **46**(sup2), 694–703. ISSN 2169-1401. DOI:10.1080/21691401.2018.1468767

[103] PANZARINI, Elisa, Stefania MARIANO, Elisabetta CARATA, Francesco MURA, Marco ROSSI a Luciana DINI. Intracellular transport of silver and gold nanoparticles and biological responses: an update. *International Journal of Molecular Sciences* [online]. 2018, **19**(5), 1305. ISSN 1422-0067. DOI:10.3390/ijms19051305

[104] REIFARTH, Martin, Stephanie HOEPPENER a Ulrich S. SCHUBERT. Uptake and intracellular fate of engineered nanoparticles in mammalian cells: Capabilities and limitations of transmission electron microscopy-polymer-based nanoparticles. *Advanced Materials* [online]. 2018, **30**(9), 1703704. ISSN 09359648. DOI:10.1002/adma.201703704

[105] FRÖHLICH, Eleonore. The role of surface charge in cellular uptake and cytotoxicity of medical nanoparticles. *International Journal of Nanomedicine* [online]. 2012, 5577. ISSN 1178-2013. DOI:10.2147/IJN.S36111

[106] YU, Zhongjie, Qi LI, Jing WANG, Yali YU, Yin WANG, Qihui ZHOU a Peifeng LI. Reactive oxygen species-related nanoparticle toxicity in the biomedical field. *Nanoscale Research Letters* [online]. 2020, **15**(1), 115. ISSN 1556-276X. DOI:10.1186/s11671-020-03344-7

[107] RAY, Paul D., Bo-Wen HUANG a Yoshiaki TSUJI. Reactive oxygen species (ROS) homeostasis and redox regulation in cellular signaling. *Cellular Signalling* [online]. 2012, **24**(5), 981–990. ISSN 08986568. DOI:10.1016/j.cellsig.2012.01.008

[108] STONE, Vicki, Helinor JOHNSTON a Roel P. F. SCHINS. Development of in vitro systems for nanotoxicology: methodological considerations. *Critical Reviews in Toxicology* [online]. 2009, **39**(7), 613–626. ISSN 1040-8444. DOI:10.1080/10408440903120975

[109] PROCKOP, Darwin J. Marrow stromal cells as stem cells for nonhematopoietic tissues. *Science* [online]. 1997, **276**(5309), 71–74. ISSN 0036-8075. DOI:10.1126/science.276.5309.71

[110] FRIEDENSTEIN, A.J., J.F. GORSKAJA a N.N. KULAGINA. Fibroblast precursors in normal and irradiated mouse hematopoietic organs. *Experimental Hematology*. 1976, **4**(5), 267–274.

[111] AFANASYEV, Boris V., Elena E. ELSTNER a Axel R. ZANDER. Friedenstein, founder of the mesenchymal stem cell concept. *Cellular Therapy and Transplantation* [online]. 2009, **1**(3), 35–38. DOI:10.3205/ctt-2009-en-000029.01

[112] FRIEDENSTEIN, A. J., I. I. PIATETZKY-SHAPIRO a K. V. PETRAKOVA. Osteogenesis in transplants of bone marrow cells. *Development* [online]. 1966, **16**(3), 381–390. ISSN 1477-9129. DOI:10.1242/dev.16.3.381

[113] CAPLAN, Arnold I. Mesenchymal stem cells. *Journal of Orthopaedic Research* [online]. 1991, **9**(5), 641–650. ISSN 0736-0266. DOI:10.1002/jor.1100090504

[114] OWEN, Maureen. Marrow stromal stem cells. *Journal of Cell Science* [online]. 1988, **1988**(Supplement_10), 63–76. ISSN 1477-9137. DOI:10.1242/jcs.1988.Supplement_10.5

[115] HORWITZ, E.M., K. LE BLANC, M. DOMINICI, I. MUELLER, I. SLAPER-CORTENBACH, F.C. MARINI, R.J. DEANS, D.S. KRAUSE a A. KEATING. Clarification of the nomenclature for MSC: The international society for cellular therapy position statement. *Cytotherapy* [online]. 2005, **7**(5), 393–395. ISSN 14653249. DOI:10.1080/14653240500319234

[116] DOMINICI, M., K. LE BLANC, I. MUELLER, I. SLAPER-CORTENBACH, F.C MARINI, D.S. KRAUSE, R.J. DEANS, A. KEATING, D.J. PROCKOP a E.M. HORWITZ. Minimal criteria for defining multipotent mesenchymal stromal cells. The International Society for Cellular Therapy position statement. *Cytotherapy* [online]. 2006, **8**(4), 315–317. ISSN 14653249. DOI:10.1080/14653240600855905

[117] DENU, Ryan A., Steven NEMCEK, Debra D. BLOOM, A. Daisy GOODRICH, Jaehyup KIM, Deane F. MOSHER a Peiman HEMATTI. Fibroblasts and mesenchymal stromal/stem cells are phenotypically indistinguishable. *Acta Haematologica* [online]. 2016, **136**(2), 85–97. ISSN 0001-5792. DOI:10.1159/000445096

[118] PITTENGER, M. F. Multilineage potential of adult human mesenchymal stem cells. *Science* [online]. 1999, **284**(5411), 143–147. ISSN 00368075. DOI:10.1126/science.284.5411.143

[119] SCHMELZER, Eva, Daniel T. MCKEEL a Jörg C. GERLACH. Characterization of human mesenchymal stem cells from different tissues and their membrane encasement for prospective transplantation therapies. *BioMed Research International* [online]. 2019, **2019**, 1–13. ISSN 2314-6133. DOI:10.1155/2019/6376271

[120] ULLAH, Imran, Raghavendra Baregundi SUBBARAO a Gyu Jin RHO. Human mesenchymal stem cells - current trends and future prospective. *Bioscience Reports* [online]. 2015, **35**(2). ISSN 0144-8463. DOI:10.1042/BSR20150025

[121] CHAMBERLAIN, Giselle, James FOX, Brian ASHTON a Jim MIDDLETON. Concise review: Mesenchymal stem cells: their phenotype, differentiation capacity, immunological features, and potential for homing. *Stem Cells* [online]. 2007, **25**(11), 2739–2749. ISSN 10665099. DOI:10.1634/stemcells.2007-0197

[122] ZACHAR, Lukáš, Darina BAČENKOVÁ a Ján ROSOCHA. Activation, homing, and role of the mesenchymal stem cells in the inflammatory environment. *Journal of Inflammation Research* [online]. 2016, **Volume 9**, 231–240. ISSN 1178-7031. DOI:10.2147/JIR.S121994

[123] VAN LINTHOUT, S., K. SAVVATIS, K. MITEVA, J. PENG, J. RINGE, K. WARSTAT, C. SCHMIDT-LUCKE, M. SITTINGER, H.-P. SCHULTHEISS a C. TSCHÖPE. Mesenchymal stem cells improve murine acute coxsackievirus B3-induced myocarditis. *European Heart Journal* [online]. 2011, **32**(17), 2168–2178. ISSN 0195-668X. DOI:10.1093/eurheartj/ehq467

[124] JIMENEZ-PUERTA, Gonzalo José, Juan Antonio MARCHAL, Elena LÓPEZ-RUIZ a Patricia GÁLVEZ-MARTÍN. Role of mesenchymal stromal cells as therapeutic agents: potential mechanisms of action and implications in their clinical use. *Journal of Clinical Medicine* [online]. 2020, **9**(2), 445. ISSN 2077-0383. DOI:10.3390/jcm9020445

[125] HAHN, Woong, Wook-Bum PYUN, Dong-Sik KIM, Won-Sun YOO, Sung-Dong LEE, Jung-Hee WON, Gil Ja SHIN, Jong-Mook KIM a Sunyoung KIM. Enhanced cardioprotective effects by coexpression of two isoforms of hepatocyte growth factor from naked plasmid DNA in a rat ischemic heart disease model. *The Journal of Gene Medicine* [online]. 2011, **13**(10), 549–555. ISSN 1099498X. DOI:10.1002/jgm.1603

[126] LI, Lili, Yao ZHANG, Yongli LI, Bo YU, Yan XU, ShiDan ZHAO a Zhenzhong GUAN. Mesenchymal stem cell transplantation attenuates cardiac fibrosis associated with isoproterenol-induced global heart failure. *Transplant International* [online]. 2008, **21**(12), 1181–1189. ISSN 09340874. DOI:10.1111/j.1432-2277.2008.00742.x

[127] DEUSE, T., C. PETER, P. W.M. FEDAK, T. DOYLE, H. REICHENSPURNER, W. H. ZIMMERMANN, T. ESCHENHAGEN, W. STEIN, J. C. WU, R. C. ROBBINS a S. SCHREPFER. Hepatocyte growth factor or vascular endothelial growth factor gene transfer maximizes mesenchymal stem cell-based myocardial salvage after acute myocardial Infarction. *Circulation* [online]. 2009, **120**(11_suppl_1), S247–S254. ISSN 0009-7322. DOI:10.1161/CIRCULATIONAHA.108.843680

[128] HSIAO, Sarah Tzu-Feng, Azar ASGARI, Zerina LOKMIC, Rodney SINCLAIR, Gregory James DUSTING, Shiang Yong LIM a Rodney James DILLEY. Comparative analysis of paracrine factor expression in human adult mesenchymal stem cells derived from bone marrow, adipose, and dermal tissue. *Stem Cells and Development* [online]. 2012, **21**(12), 2189–2203. ISSN 1547-3287. DOI:10.1089/scd.2011.0674

[129] PENN, M S, J PASTORE, T MILLER a R ARAS. SDF-1 in myocardial repair. *Gene Therapy* [online]. 2012, **19**(6), 583–587. ISSN 0969-7128. DOI:10.1038/gt.2012.32

[130] HOHMANN a DEHGHANI. The cytoskeleton—a complex interacting meshwork. *Cells* [online]. 2019, **8**(4), 362. ISSN 2073-4409. DOI:10.3390/cells8040362

[131] SEETHARAMAN, Shailaja a Sandrine ETIENNE-MANNEVILLE. Cytoskeletal crosstalk in cell migration. *Trends in Cell Biology* [online]. 2020, **30**(9), 720–735. ISSN 09628924. DOI:10.1016/j.tcb.2020.06.004

[132] ZENGEL, Pamela, Anna NGUYEN-HOANG, Christoph SCHILDHAMMER, Roman ZANTL, Valentin KAHL a Elias HORN. μ-Slide Chemotaxis: A new chamber for long-term chemotaxis studies. *BMC Cell Biology* [online]. 2011, **12**(1), 21. ISSN 1471-2121. DOI:10.1186/1471-2121-12-21

[133] JONKMAN, James E. N., Judith A. CATHCART, Feng XU, Miria E. BARTOLINI, Jennifer E. AMON, Katarzyna M. STEVENS a Pina COLARUSSO. An introduction to the wound healing assay using live-cell microscopy. *Cell Adhesion & Migration* [online]. 2014, **8**(5), 440–451. ISSN 1933-6918. DOI:10.4161/cam.36224

[134] ANTANAVICIUTE, Laima, Sophie DUBACQ a Olivier VARET. An embedded application for cell culture confluency estimation using the InCellis ® Smart Cell Imaging System. *BioTechniques* [online]. 2018, **64**(3), 127. ISSN 0736-6205. DOI:10.2144/btn-2017-0115

[135] HAENEL, Frauke a Norbert GARBOW. Cell counting and cnfluency analysis as quality controls in cell-based assays. *Perkin Elmer Inc.* 2014, 1–5.

[136] Quantifying confluency to reduce MSC passage timing variation. *Nikon Helthcare* [online]. [vid. 2021-02-05]. Dostupné z: https://www.healthcare.nikon.com/en/ss/cell-image-lab/case/c10.html

[137] BOWLES, Annie C., Brittni A. SCRUGGS a Bruce A. BUNNELL. Mesenchymal stem cell-based therapy in a mouse model of experimental autoimmune encephalomyelitis (EAE). In: *Animal Models for Stem Cell Therapy. Methods in Molecular Biology (Methods and Protocols)* [online]. New York: Humana Press, 2014, s. 303–319. ISBN 978-1-4939-1452-4. DOI:10.1007/978-1-4939-1453-1_25

[138] HAASTERS, Florian, Wolf Christian PRALL, David ANZ, Carole BOURQUIN, Christoph PAUTKE, Stefan ENDRES, Wolf MUTSCHLER, Denitsa DOCHEVA a Matthias SCHIEKER. Morphological and immunocytochemical characteristics indicate the yield of early progenitors and represent a quality control for human mesenchymal stem cell culturing. *Journal of Anatomy* [online]. 2009, **214**(5), 759–767. ISSN 00218782. DOI:10.1111/j.1469-7580.2009.01065.x

[139] SMITH, Jason R., Radhika POCHAMPALLY, Anthony PERRY, Shu-Ching HSU a Darwin J. PROCKOP. Isolation of a highly clonogenic and multipotential subfraction of adult stem cells from bone marrow stroma. *Stem Cells* [online]. 2004, **22**(5), 823–831. ISSN 10665099. DOI:10.1634/stemcells.22-5-823

[140] L. RAMOS, Teresa, Luis Ignacio SÁNCHEZ-ABARCA, Sandra MUNTIÓN, Silvia PRECIADO, Noemí PUIG, Guillermo LÓPEZ-RUANO, Ángel HERNÁNDEZ-HERNÁNDEZ, Alba REDONDO, Rebeca ORTEGA, Concepción RODRÍGUEZ, Fermín SÁNCHEZ-GUIJO a Consuelo DEL CAÑIZO. MSC surface markers (CD44, CD73, and CD90) can identify human MSC-derived extracellular vesicles by conventional flow cytometry. *Cell Communication and Signaling* [online]. 2016, **14**(1), 2. ISSN 1478-811X. DOI:10.1186/s12964-015-0124-8

[141] BAIAZITOVA, Larisa, Josef SKOPALIK, Jiri CHMELIK, Inna ZUMBERG, Vratislav CMIEL, Katerina POLAKOVA a Ivo PROVAZNIK. The effect of rhodamine-derived superparamagnetic maghemite nanoparticles on the motility of human mesenchymal stem cells and mouse embryonic fibroblast cells. *Molecules* [online]. 2019, **24**(7), 1192. ISSN 1420-3049. DOI:10.3390/molecules24071192

[142] ALT, Eckhard, Yasheng YAN, Sebastian GEHMERT, Yao-Hua SONG, Andrew ALTMAN, Sanga GEHMERT, Daynene VYKOUKAL a Xiaowen BAI. Fibroblasts share mesenchymal phenotypes with stem cells, but lack their differentiation and colony-forming potential. *Biology of the Cell* [online]. 2011, **103**(4), 197–208. ISSN 02484900. DOI:10.1042/BC20100117

[143] CLAYCOMB, W. C., N. A. LANSON, B. S. STALLWORTH, D. B. EGELAND, J. B. DELCARPIO, A. BAHINSKI a N. J. IZZO. HL-1 cells: A cardiac muscle cell line that contracts and retains phenotypic characteristics of the adult cardiomyocyte. *Proceedings of the National Academy of Sciences* [online]. 1998, **95**(6), 2979–2984. ISSN 0027-8424. DOI:10.1073/pnas.95.6.2979

[144] WHITE, Steven M., Phillip E. CONSTANTIN a William C. CLAYCOMB. Cardiac physiology at the cellular level: use of cultured HL-1 cardiomyocytes for studies of cardiac muscle cell structure and function. *American Journal of Physiology-Heart and Circulatory Physiology* [online]. 2004, **286**(3), H823–H829. ISSN 0363-6135. DOI:10.1152/ajpheart.00986.2003

[145] SVOBODA, Ondrej, Larisa BAIAZITOVA, Vratislav CMIEL, Josef SKOPALIK, Zdenka FOHLEROVA, Jaromir HUBALEK a Ivo PROVAZNIK. Simultaneous electrical and fluorescence recording of HL-1 cells electrical activity in response to extracellular calcium stimulation. In: *2018 Computing in Cardiology Conference (CinC)* [online]. 2018, s. 1–4. DOI:10.22489/CinC.2018.103

[146] Cell culture basics: handbook. *Invitrogen and Gibco by Life technologies* [online]. [vid. 2021-05-27]. Dostupné z: https://www.vanderbilt.edu/viibre/CellCultureBasicsEU.pdf

[147] Mesenchymal stem cell culture protocols. *Sigma-Aldrich* [online]. [vid. 2020-04-16]. Dostupné z: https://www.sigmaaldrich.com/CZ/en/technical-documents/protocol/cell-culture-and-cell-culture-analysis/stem-cell-culture/mesenchymal-stem-cell-culture-protocols

[148] 3t3 cell culture protocol. *Sigma-Aldrich* [online]. [vid. 2020-05-04]. Dostupné z: https://cect.umd.edu/sites/cect.umd.edu/files/resource_documents/3T3 Fibroblast culture.pdf

[149] HL-1 cells. *Sigma-Aldrich* [online]. [vid. 2020-06-15]. Dostupné z: https://www.sigmaaldrich.com/CZ/en/technical-documents/protocol/cell-culture-and-cell-culture-analysis/mammalian-cell-culture/hl-1-cells

[150] ROSS, Stephen T, John R ALLEN a Michael W DAVIDSON. Chapter 2 - Practical considerations of objective lenses for application in cell biology. In: Jennifer C WATERS a Torsten WITTMAN, ed. *Quantitative Imaging in Cell Biology* [online]. B.m.: Academic Press, 2014, Methods in Cell Biology, s. 19–34. ISSN 0091-679X. DOI:https://doi.org/10.1016/B978-0-12-420138-5.00002-1

[151] WILSON, Martin. Immersion objectives: using oil, glycerol, or water to overcome some of the limits of resolution. *Leica Microsystems* [online]. 2017 [vid. 2020-11-08]. Dostupné z: https://www.leica-microsystems.com/science-lab/immersion-objectives-using-oil-glycerol-or-water-to-overcome-some-of-the-limits-of-resolution/

[152] YAMAMOTO, Akiko, Shuzo MISHIMA, Norio MARUYAMA a Masae SUMITA. Quantitative evaluation of cell attachment to glass, polystyrene, and fibronectin- or collagen-coated polystyrene by measurement of cell adhesive shear force and cell detachment energy. *Journal of Biomedical Materials Research* [online]. 2000, **50**(2), 114–124. ISSN 00219304. DOI:10.1002/(SICI)1097-4636(200005)50:2<114::AID-JBM4>3.0.CO;2-6

[153] HARNETT, Elaine M., John ALDERMAN a Terri WOOD. The surface energy of various biomaterials coated with adhesion molecules used in cell culture. *Colloids and Surfaces B: Biointerfaces* [online]. 2007, **55**(1), 90–97. ISSN 09277765. DOI:10.1016/j.colsurfb.2006.11.021

[154] *The guide to live cell imaging* [online]. Dostupné z: https://www.leica-microsystems.com/science-lab/e-book-the-guide-to-live-cell-imaging/?nlc=20200828-SFDC-009950

[155] ICHA, Jaroslav, Michael WEBER, Jennifer C. WATERS a Caren NORDEN. Phototoxicity in live fluorescence microscopy, and how to avoid it. *BioEssays* [online]. 2017, **39**(8), 1700003. ISSN 02659247. DOI:10.1002/bies.201700003

[156] FluoCells^{TM} Prepared Slide #1 (BPAE cells with MitoTracker^{TM} Red CMXRos, Alexa Fluor^{TM} 488 Phalloidin, and DAPI). *Thermo Fisher Scientific* [online]. [vid. 2020-09-28]. Dostupné z: https://www.thermofisher.com/order/catalog/product/F36924#/F36924

[157] Spectra viewer tool. *Thermo Fisher Scientific* [online]. [vid. 2020-09-28]. Dostupné z: https://www.thermofisher.com/cz/en/home/life-science/cell-analysis/labeling-chemistry/fluorescence-spectraviewer.html

[158] DURAND, R E a P L OLIVE. Cytotoxicity, mutagenicity and DNA damage by Hoechst 33342. *Journal of Histochemistry & Cytochemistry* [online]. 1982, **30**(2), 111–116. ISSN 0022-1554. DOI:10.1177/30.2.7061816

[159] BisBenzimide H 33342 trihydrochloride. *Sigma-Aldrich* [online]. [vid. 2020-06-05]. Dostupné z: https://www.sigmaaldrich.com/CZ/en/product/sigma/14533

[160] PURSCHKE, Martin, Noemi RUBIO, Kathryn D. HELD a Robert W. REDMOND. Phototoxicity of Hoechst 33342 in time-lapse fluorescence microscopy. *Photochemical & Photobiological Sciences* [online]. 2010, **9**(12), 1634. ISSN 1474-905X. DOI:10.1039/c0pp00234h

[161] SIEMANN, Dietmar W. a Peter C. KENG. Cell cycle specific toxicity of the Hoechst 33342 stain in untreated or irradiated murine tumor cells. *Cancer research*. 1986, **46**(7), 3556–3559.

[162] Hoechst 33342 nucleic acid stain. *Thermo Fisher Scientific* [online]. [vid. 2020-06-05]. Dostupné z: https://www.thermofisher.com/order/catalog/product/H1399?SID=srch-srp-H1399#/H1399?SID=srch-srp-H1399

[163] Calcein AM viability dye. *Thermo Fisher Scientific* [online]. [vid. 2020-06-05]. Dostupné z: https://www.thermofisher.com/order/catalog/product/C3099?SID=srch-srp-C3099#/C3099?SID=srch-srp-C3099

[164] XIU MING WANG, Paul I. TERASAKI, George W. RANKIN, David CHIA, HUI PING ZHONG a Steven HARDY. A new microcellular cytotoxicity test based on calcein AM release. *Human Immunology* [online]. 1993, **37**(4), 264–270. ISSN 01988859. DOI:10.1016/0198-8859(93)90510-8

[165] Calcein-AM. *Sigma-Aldrich* [online]. [vid. 2020-06-05]. Dostupné z: https://www.sigmaaldrich.com/CZ/en/product/sigma/17783

[166] SEBASTIÀ, Jordi, Rosa CRISTÒFOL, Manuela MARTÍN, Eduard RODRÍGUEZ-FARRÉ a Coral SANFELIU. Evaluation of fluorescent dyes for measuring intracellular glutathione content in primary cultures of human neurons and neuroblastoma SH-SY5Y. *Cytometry Part A* [online]. 2003, **51A**(1), 16–25. ISSN 15524922. DOI:10.1002/cyto.a.10003

[167] CellTracker^{TM} Green CMFDA Dye. *Thermo Fisher Scientific* [online]. [vid. 2020-06-05]. Dostupné z: https://www.thermofisher.com/order/catalog/product/C2925#/C2925

[168] CellTracker^{TM} Red CMTPX Dye. *Thermo Fisher Scientific* [online]. [vid. 2020-06-05]. Dostupné z: https://www.thermofisher.com/order/catalog/product/C34552#/C34552

[169] CellMask^{TM} Plasma Membrane Stains. *Thermo Fisher Scientific* [online]. [vid. 2020-05-05]. Dostupné z: https://www.thermofisher.com/document-connect/document-connect.html?url=https%3A%2F%2Fassets.thermofisher.com%2FTFS-Assets%2FLSG%2Fmanuals%2FCellMask_Plasma_Membrane_Stains_PI.pdf&title=Q2VsbE1hc2sgUGxhc21hIE1lbWJyYW5lIFN0YWlucw==

[170] Wheat Germ Agglutinin Conjugates. *Thermo Fisher Scientific* [online]. [vid. 2020-05-05]. Dostupné z: https://www.thermofisher.com/document-connect/document-connect.html?url=https%3A%2F%2Fassets.thermofisher.com%2FTFS-Assets%2FLSG%2Fmanuals%2Fmp00831.pdf&title=V2hlYXQgR2VybSBBZ2dsdXRpbmluIENvbmp1Z2F0ZXM=

[171] CellBrite® Steady Membrane Staining Kits. *Biotium* [online]. [vid. 2021-05-27]. Dostupné z: https://biotium.com/product/cellbrite-steady-membrane-staining-kits/

[172] UTHAMAN, S, M MUTHIAH, I K PARK a C S CHO. Fabrication and development of magnetic particles for gene therapy. In: *Polymers and Nanomaterials for Gene Therapy*. B.m.: Woodhead Publishing, 2016, s. 215–230.

[173] DUNN, Kenneth W., Malgorzata M. KAMOCKA a John H. MCDONALD. A practical guide to evaluating colocalization in biological microscopy. *American Journal of Physiology-Cell Physiology* [online]. 2011, **300**(4), C723–C742. ISSN 0363-6143. DOI:10.1152/ajpcell.00462.2010

[174] Lambda square mapping and FLIM: Explore photonic landscapes with the Leica TCS SP5 X. *Leica Microsystems* [online]. [vid. 2021-05-26]. Dostupné z: https://downloads.leica-microsystems.com/Leica TCS SP5 X/Brochures/Leica Lambda Square Mapping and FLIM-Brochure_EN.pdf

[175] BARADEZ, Marc-Olivier a Damian MARSHALL. The use of multidimensional image-based analysis to accurately monitor cell growth in 3D bioreactor culture. *PLoS ONE* [online]. 2011, **6**(10), e26104. ISSN 1932-6203. DOI:10.1371/journal.pone.0026104

[176] BAIAZITOVA, Larisa, Josef SKOPALIK, Ondrej SVOBODA, Jiri CHMELIK a Ivo PROVAZNIK. Fluorescence method for measuring cell proliferation by image analysis of cell confluency. In: *XVII. Workshop of Physical Chemists and Electrochemists: Book of abstracts*. Brno, Czech Republic: Masaryk University - MUNI PRESS, 2017, s. 47–48.

[177] BOBADILLA, Ana Victoria Ponce, Jazmine ARÉVALO, Eduard SARRÓ, Helen M. BYRNE, Philip K. MAINI, Thomas CARRARO, Simone BALOCCO, Anna MESEGUER a Tomás ALARCÓN. In vitro cell migration quantification method for scratch assays. *Journal of The Royal Society Interface* [online]. 2019, **16**(151), 20180709. ISSN 1742-5689. DOI:10.1098/rsif.2018.0709

[178] KAUANOVA, Sholpan, Arshat URAZBAYEV a Ivan VOROBJEV. The frequent sampling of wound scratch assay reveals the "opportunity" window for quantitative evaluation of cell motility-impeding drugs. *Frontiers in Cell and Developmental Biology* [online]. 2021, **9**. ISSN 2296-634X. DOI:10.3389/fcell.2021.640972

[179] SHAPIRO, S. S. a M. B. WILK. An analysis of variance test for normality (complete Samples). *Biometrika* [online]. 1965, **52**(3/4), 591. ISSN 00063444. DOI:10.2307/2333709

[180] SHESKIN, David J. *Handbook of parametric and nonparametric statistical procedures*. B.m.: crc Press, 2020.

[181] DRISCOLL, Wade C. Robustness of the ANOVA and Tukey-Kramer statistical tests. *Computers & Industrial Engineering* [online]. 1996, **31**(1–2), 265–268. ISSN 03608352. DOI:10.1016/0360-8352(96)00127-1

[182] FEITH, Marek, Tomáš VIČAR, Jaromír GUMULEC, Martina RAUDENSKÁ, Anette GJÖRLOFF WINGREN, Michal MASAŘÍK a Jan BALVAN. Quantitative phase dynamics of cancer cell populations affected by blue light. *Applied Sciences* [online]. 2020, **10**(7), 2597. ISSN 2076-3417. DOI:10.3390/app10072597

[183] ULMAN, Vladimír, Martin MAŠKA, Klas E G MAGNUSSON, Olaf RONNEBERGER, Carsten HAUBOLD, Nathalie HARDER, Pavel MATULA, Petr MATULA, David SVOBODA, Miroslav RADOJEVIC, Ihor SMAL, Karl ROHR, Joakim JALDÉN, Helen M BLAU, Oleh DZYUBACHYK, Boudewijn LELIEVELDT, Pengdong XIAO, Yuexiang LI, Siu-Yeung CHO, Alexandre C DUFOUR, Jean-Christophe OLIVO-MARIN, Constantino C REYES-ALDASORO, Jose A SOLIS-LEMUS, Robert BENSCH, Thomas BROX, Johannes STEGMAIER, Ralf MIKUT, Steffen WOLF, Fred A HAMPRECHT, Tiago ESTEVES, Pedro QUELHAS, Ömer DEMIREL, Lars MALMSTRÖM, Florian JUG, Pavel TOMANCAK, Erik MEIJERING, Arrate MUÑOZ-BARRUTIA, Michal KOZUBEK a Carlos ORTIZ-DE-SOLORZANO. An objective comparison of cell-tracking algorithms. *Nature Methods* [online]. 2017, **14**(12), 1141–1152. ISSN 1548-7091. DOI:10.1038/nmeth.4473

[184] MAGNUSSON, Klas E. G., Joakim JALDEN, Penney M. GILBERT a Helen M. BLAU. Global linking of cell tracks using the viterbi algorithm. *IEEE Transactions on Medical Imaging* [online]. 2015, **34**(4), 911–929. ISSN 0278-0062. DOI:10.1109/TMI.2014.2370951

[185] HALLER, Stefan, Mangal PRAKASH, Lisa HUTSCHENREITER, Tobias PIETZSCH, Carsten ROTHER, Florian JUG, Paul SWOBODA a Bogdan SAVCHYNSKYY. A primal-dual solver for large-scale tracking-by-assignment. In: Silvia CHIAPPA a Roberto CALANDRA, ed. *Proceedings of the Twenty Third International Conference on Artificial Intelligence and Statistics* [online]. B.m.: PMLR, 2020, s. 2539–2549. Proceedings of Machine Learning Research. Dostupné z: http://proceedings.mlr.press/v108/haller20a.html

[186] VICAR, Tomas, Jaromir GUMULEC, Jan BALVAN, Michal HRACHO a Radim KOLAR. Label-free nuclear staining reconstruction in quantitative phase images using deep learning. In: *World Congress on Medical Physics and Biomedical Engineering 2018* [online]. Singapore: Springer Singapore, 2019, s. 239–242. DOI:10.1007/978-981-10-9035-6_43

[187] *NIST/SEMATECH e-handbook of statistical methods* [online]. DOI:10.18434/M32189

[188] STARK, Wendelin J. Nanoparticles in biological systems. *Angewandte Chemie International Edition* [online]. 2011, **50**(6), 1242–1258. ISSN 14337851. DOI:10.1002/anie.200906684

[189] YANG, Zhen, John A. BOGOVIC, Aaron CARASS, Mao YE, Peter C. SEARSON a Jerry L. PRINCE. Automatic cell segmentation in fluorescence images of confluent cell monolayers using multi-object geometric deformable model. In: Sebastien OURSELIN a David R. HAYNOR, ed. *MEDICAL IMAGING 2013: IMAGE PROCESSING* [online]. Lake Buena Vista, FL: Proceedings of SPIE, 2013, s. 866904. DOI:10.1117/12.2006603

[190] SHEN, Jianhuo, Teng LI, Chuanrui HU, Hong HE a Jianfei LIU. Automatic cell segmentation using mini-u-net on fluorescence in situ hybridization images. In: Horst K. HAHN a Kensaku MORI, ed. *Medical Imaging 2019: Computer-Aided Diagnosis* [online]. San Diego, CA: SPIE, 2019, s. 101. ISBN 9781510625471. DOI:10.1117/12.2513394

[191] SALVI, Massimo, Umberto MORBIDUCCI, Francesco AMADEO, Rosaria SANTORO, Francesco ANGELINI, Isotta CHIMENTI, Diana MASSAI, Elisa MESSINA, Alessandro GIACOMELLO, Maurizio PESCE a Filippo MOLINARI. Automated segmentation of fluorescence microscopy images for 3D cell detection in human-derived cardiospheres. *Scientific Reports* [online]. 2019, **9**(1), 6644. ISSN 2045-2322. DOI:10.1038/s41598-019-43137-2

[192] ARIAS, Laís, Juliano PESSAN, Ana VIEIRA, Taynara LIMA, Alberto DELBEM a Douglas MONTEIRO. Iron oxide nanoparticles for biomedical applications: A perspective on synthesis, drugs, antimicrobial activity, and toxicity. *Antibiotics* [online]. 2018, **7**(2), 46. ISSN 2079-6382. DOI:10.3390/antibiotics7020046

[193] SINGH, Neenu, Gareth J.S. JENKINS, Romisa ASADI a Shareen H. DOAK. Potential toxicity of superparamagnetic iron oxide nanoparticles (SPION). *Nano Reviews* [online]. 2010, **1**(1), 5358. ISSN 2000-5121. DOI:10.3402/nano.v1i0.5358

[194] FRONZA, M., B. HEINZMANN, M. HAMBURGER, S. LAUFER a I. MERFORT. Determination of the wound healing effect of Calendula extracts using the scratch assay with 3T3 fibroblasts. *Journal of Ethnopharmacology* [online]. 2009, **126**(3), 463–467. ISSN 03788741. DOI:10.1016/j.jep.2009.09.014

[195] HOSTANSKA, Katarina, Matthias ROSTOCK, Joerg MELZER, Stephan BAUMGARTNER a Reinhard SALLER. A homeopathic remedy from arnica, marigold, St. John's wort and comfrey accelerates in vitro wound scratch closure of NIH 3T3 fibroblasts. *BMC Complementary and Alternative Medicine* [online]. 2012, **12**(1), 100. ISSN 1472-6882. DOI:10.1186/1472-6882-12-100

[196] ADDIS, Roberta, Sara CRUCIANI, Sara SANTANIELLO, Emanuela BELLU, Giorgia SARAIS, Carlo VENTURA, Margherita MAIOLI a Giorgio PINTORE. Fibroblast proliferation and migration in wound healing by phytochemicals: Evidence for a novel synergic outcome. *International Journal of Medical Sciences* [online]. 2020, **17**(8), 1030–1042. ISSN 1449-1907. DOI:10.7150/ijms.43986

[197] HAMMERSCHMIDT, Matthias a Doris WEDLICH. Regulated adhesion as a driving force of gastrulation movements. *Development* [online]. 2008, **135**(22), 3625–3641. ISSN 1477-9129. DOI:10.1242/dev.015701

[198] SCHINDELIN, Johannes, Ignacio ARGANDA-CARRERAS, Erwin FRISE, Verena KAYNIG, Mark LONGAIR, Tobias PIETZSCH, Stephan PREIBISCH, Curtis RUEDEN, Stephan SAALFELD, Benjamin SCHMID, Jean-Yves TINEVEZ, Daniel James WHITE, Volker HARTENSTEIN, Kevin ELICEIRI, Pavel TOMANCAK a Albert CARDONA. Fiji: an open-source platform for biological-image analysis. *Nature Methods* [online]. 2012, **9**(7), 676–682. ISSN 1548-7091. DOI:10.1038/nmeth.2019

[199] RUEDEN, Curtis T., Johannes SCHINDELIN, Mark C. HINER, Barry E. DEZONIA, Alison E. WALTER, Ellen T. ARENA a Kevin W. ELICEIRI. ImageJ2: ImageJ for the next generation of scientific image data. *BMC Bioinformatics* [online]. 2017, **18**(1), 529. ISSN 1471-2105. DOI:10.1186/s12859-017-1934-z

[200] BERGELAND, Trygve, Jannicke WIDERBERG, Oddmund BAKKE a Tommy W. NORDENG. Mitotic partitioning of endosomes and lysosomes. *Current Biology* [online]. 2001, **11**(9), 644–651. ISSN 09609822. DOI:10.1016/S0960-9822(01)00177-4

[201] WARREN, Graham. Membrane partitioning during cell division. *Annual Review of Biochemistry* [online]. 1993, **62**(1), 323–348. ISSN 0066-4154. DOI:10.1146/annurev.bi.62.070193.001543

[202] BIRKY, C. WILLIAM. The partitioning of cytoplasmic organelles at cell division. In: *Aspects of Cell Regulation* [online]. B.m.: Elsevier, 1983, s. 49–89. DOI:10.1016/B978-0-12-364376-6.50009-0

[203] ABDAL DAYEM, Ahmed, Mohammed HOSSAIN, Soo LEE, Kyeongseok KIM, Subbroto SAHA, Gwang-Mo YANG, Hye CHOI a Ssang-Goo CHO. The role of reactive oxygen species (ROS) in the biological activities of metallic nanoparticles. *International Journal of Molecular Sciences* [online]. 2017, **18**(1), 120. ISSN 1422-0067. DOI:10.3390/ijms18010120

[204] SHI, M., Z.-W. LIU a F.-S. WANG. Immunomodulatory properties and therapeutic application of mesenchymal stem cells. *Clinical & Experimental Immunology* [online]. 2011, **164**(1), 1–8. ISSN 00099104. DOI:10.1111/j.1365-2249.2011.04327.x

[205] CAGLIANI, Joaquin, Daniel GRANDE, Ernesto P MOLMENTI, Edmund J. MILLER a Horacio L.R. RILO. Immunomodulation by mesenchymal stromal cells and their clinical applications. *Journal Of Stem Cell & Regenerative Biology* [online]. 2017, **3**(2), 1–14. ISSN 24710598. DOI:10.15436/2471-0598.17.022

[206] BARBASH, Israel M., Pierre CHOURAQUI, Jack BARON, Micha S. FEINBERG, Sharon ETZION, Ariel TESSONE, Liron MILLER, Esther GUETTA, Dov ZIPORI, Laurence H. KEDES, Robert A. KLONER a Jonathan LEOR. Systemic delivery of bone marrow–derived mesenchymal stem cells to the infarcted myocardium. *Circulation* [online]. 2003, **108**(7), 863–868. ISSN 0009-7322. DOI:10.1161/01.CIR.0000084828.50310.6A

[207] BAI, Rui, Lei TIAN, Yi LI, Jiao ZHANG, Yujie WEI, Zhigeng JIN, Zhiqiang LIU a Huiliang LIU. Combining ECM hydrogels of cardiac bioactivity with stem cells of high cardiomyogenic potential for myocardial repair. *Stem Cells International* [online]. 2019, **2019**, 1–14. ISSN 1687-966X. DOI:10.1155/2019/6708435

[208] KIM, Chan Woo, Chan Joon KIM, Eun-Hye PARK, Seungbae RYU, Yunki LEE, Eunmin KIM, Kwonyoon KANG, Kwan Yong LEE, Eun-Ho CHOO, Byung-Hee HWANG, Ho-Joong YOUN, Ki Dong PARK a Kiyuk CHANG. MSC-encapsulating in situ cross-linkable gelatin hydrogels to promote myocardial repair. *ACS Applied Bio Materials* [online]. 2020, **3**(3), 1646–1655. ISSN 2576-6422. DOI:10.1021/acsabm.9b01215

[209] BÉBAROVÁ, Markéta, Peter MATEJOVIČ, Olga ŠVECOVÁ, Roman KULA, Milena ŠIMURDOVÁ a Jiří ŠIMURDA. Nicotine at clinically relevant concentrations affects atrial inward rectifier potassium current sensitive to acetylcholine. *Naunyn-Schmiedeberg's Archives of Pharmacology* [online]. 2017, **390**(5), 471–481. ISSN 0028-1298. DOI:10.1007/s00210-017-1341-z

[210] LOUCH, William E., Katherine A. SHEEHAN a Beata M. WOLSKA. Methods in cardiomyocyte isolation, culture, and gene transfer. *Journal of Molecular and Cellular Cardiology* [online]. 2011, **51**(3), 288–298. ISSN 00222828. DOI:10.1016/j.yjmcc.2011.06.012

[211] NIPPERT, Franziska, Rolf SCHRECKENBERG a Klaus-Dieter SCHLÜTER. Isolation and cultivation of adult rat cardiomyocytes. *Journal of Visualized Experiments* [online]. 2017, (128). ISSN 1940-087X. DOI:10.3791/56634

[212] GERDES, Hans-Hermann, Nickolay V. BUKORESHTLIEV a João F.V. BARROSO. Tunneling nanotubes: A new route for the exchange of components between animal cells. *FEBS Letters* [online]. 2007, **581**(11), 2194–2201. ISSN 00145793. DOI:10.1016/j.febslet.2007.03.071

[213] RUSTOM, A. Nanotubular highways for intercellular organelle transport. *Science* [online]. 2004, **303**(5660), 1007–1010. ISSN 0036-8075. DOI:10.1126/science.1093133

[214] SPEES, J. L., S. D. OLSON, M. J. WHITNEY a D. J. PROCKOP. Mitochondrial transfer between cells can rescue aerobic respiration. *Proceedings of the National Academy of Sciences* [online]. 2006, **103**(5), 1283–1288. ISSN 0027-8424. DOI:10.1073/pnas.0510511103

[215] KOYANAGI, Masamichi, Ralf P. BRANDES, Judith HAENDELER, Andreas M. ZEIHER a Stefanie DIMMELER. Cell-to-cell connection of endothelial progenitor cells with cardiac myocytes by nanotubes. *Circulation Research* [online]. 2005, **96**(10), 1039–1041. ISSN 0009-7330. DOI:10.1161/01.RES.0000168650.23479.0c

[216] SPIRA, Micha E. a Aviad HAI. Multi-electrode array technologies for neuroscience and cardiology. *Nature Nanotechnology* [online]. 2013, **8**(2), 83–94. ISSN 1748-3387. DOI:10.1038/nnano.2012.265

[217] PLENZ, Dietmar, Craig V. STEWART, Woodrow SHEW, Hongdian YANG, Andreas KLAUS a Tim BELLAY. Multi-electrode array recordings of neuronal avalanches in organotypic cultures. *Journal of Visualized Experiments* [online]. 2011, (54). ISSN 1940-087X. DOI:10.3791/2949

[218] DIDIER, Charles M, Avra KUNDU, David DEROO a Swaminathan RAJARAMAN. Development of in vitro 2D and 3D microelectrode arrays and their role in advancing biomedical research. *Journal of Micromechanics and Microengineering* [online]. 2020, **30**(10), 103001. ISSN 0960-1317. DOI:10.1088/1361-6439/ab8e91

[219] OJOVAN, Silviya M., Noha RABIEH, Nava SHMOEL, Hadas EREZ, Eilon MAYDAN, Ariel COHEN a Micha E. SPIRA. A feasibility study of multi-site,intracellular recordings from mammalian neurons by extracellular gold mushroom-shaped microelectrodes. *Scientific Reports* [online]. 2015, **5**(1), 14100. ISSN 2045-2322. DOI:10.1038/srep14100

[220] RYYNÄNEN, Tomi, Anssi PELKONEN, Kestutis GRIGORAS, Oili M. E. YLIVAARA, Tanja HYVÄRINEN, Jouni AHOPELTO, Mika PRUNNILA, Susanna NARKILAHTI a Jukka LEKKALA. Microelectrode array with transparent ALD TiN electrodes. *Frontiers in Neuroscience* [online]. 2019, **13**. ISSN 1662-453X. DOI:10.3389/fnins.2019.00226

[221] SVOBODA, Ondrej, Josef SKOPALIK, Larisa BAIAZITOVA, Eva GABRIELOVA, Vratislav CMIEL, Ivo PROVAZNIK, Zdenka FOHLEROVA a Jaromir HUBALEK. An evaluation of different coatings for TiN microelectrode chambers used for neonatal cardiomyocytes. *Computing in Cardiology* [online]. 2016, **43**, 365–368. ISSN 2325887X. DOI:10.22489/cinc.2016.107-309

[222] LIN, Ziliang Carter, Allister F. MCGUIRE, Paul W. BURRIDGE, Elena MATSA, Hsin-Ya LOU, Joseph C. WU a Bianxiao CUI. Accurate nanoelectrode recording of human pluripotent stem cell-derived cardiomyocytes for assaying drugs and modeling disease. *Microsystems & Nanoengineering* [online]. 2017, **3**(1), 16080. ISSN 2055-7434. DOI:10.1038/micronano.2016.80

[223] VARDI, Roni, Amir GOLDENTAL, Shira SARDI, Anton SHEININ a Ido KANTER. Simultaneous multi-patch-clamp and extracellular-array recordings: Single neuron reflects network activity. *Scientific Reports* [online]. 2016, **6**(1), 36228. ISSN 2045-2322. DOI:10.1038/srep36228

[224] KANNAN, Madhuvanthi, Ganesh VASAN a Vincent A. PIERIBONE. Optimizing strategies for developing genetically encoded voltage indicators. *Frontiers in Cellular Neuroscience* [online]. 2019, **13**. ISSN 1662-5102. DOI:10.3389/fncel.2019.00053

[225] LEE, Elizabeth E.L. a Francisco BEZANILLA. Biophysical characterization of genetically encoded voltage sensor ASAP1: Dynamic range improvement. *Biophysical Journal* [online]. 2017, **113**(10), 2178–2181. ISSN 00063495. DOI:10.1016/j.bpj.2017.10.018

[226] ST-PIERRE, François, Jesse D MARSHALL, Ying YANG, Yiyang GONG, Mark J SCHNITZER a Michael Z LIN. High-fidelity optical reporting of neuronal electrical activity with an ultrafast fluorescent voltage sensor. *Nature Neuroscience* [online]. 2014, **17**(6), 884–889. ISSN 1097-6256. DOI:10.1038/nn.3709

[227] MURELI, Shwetha, Christopher P. GANS, Dan J. BARE, David L. GEENEN, Nalin M. KUMAR a Kathrin BANACH. Mesenchymal stem cells improve cardiac conduction by upregulation of connexin 43 through paracrine signaling. *American Journal of Physiology-Heart and Circulatory Physiology* [online]. 2013, **304**(4), H600–H609. ISSN 0363-6135. DOI:10.1152/ajpheart.00533.2012

[228] BOOMSMA, Robert A. a David L. GEENEN. Evidence for transfer of membranes from mesenchymal stem cells to HL-1 cardiac cells. *Stem Cells International* [online]. 2014, **2014**, 1–9. ISSN 1687-966X. DOI:10.1155/2014/653734

[229] BADER, A, A BRODARAC, R HETZER, YH CHOI a C STAMM. Paracrine effects of cord blood-mesenchymal stem cells on apoptotic events and cell death of postischaemic HL-1 cardiomyocytes. *The Thoracic and Cardiovascular Surgeon* [online]. 2012, **60**(S 01). ISSN 0171-6425. DOI:10.1055/s-0031-1297866

[230] ANAN, Mayumi, Kazuyoshi UCHIHASHI, Shigehisa AOKI, Aki MATSUNOBU, Akifumi OOTANI, Koichi NODE a Shuji TODA. A promising culture model for analyzing the interaction between adipose tissue and cardiomyocytes. *Endocrinology* [online]. 2011, **152**(4), 1599–1605. ISSN 0013-7227. DOI:10.1210/en.2010-1106

LIST OF ABBREVIATIONS

3T3	NIH 3T3 cell line
2D	Two-dimensional
3D	Three-dimensional
AM	Acetoxymethyl
AOBS	Acousto-optical tunable beam-splitter
AOTF	Acousto-optical tunable filter
ASAP1	Accelerated Sensor of Action Potentials 1
bFGF	Basic fibroblast growth factor
CMFDA	CellTracker™ Green CMFDA Dye
CMTPX	CellTracker™ Red CMTPX Dye
CNN	Convolution Neural Network
DEAE	Diethylaminoethyl
DHM	Digital holographic microscopy
DIC	Differential interference contrast
DLS	Dynamic light scattering
DMEM	Dulbecco's Modified Eagle Medium
DMSO	Dimethyl sulfoxide
DNA	Deoxyribonucleic acid
ECM	Extracellular matrix
FBS	Foetal bovine serum
FGF	Fibroblast growth factor
FITC	Fluorescein
FN	Fibronectin
FPALM	Fluorescence photoactivation localization microscopy
GEVIs	Genetically encoded voltage indicators
GFP	Green Fluorescent Protein
HA	Hyaluronic acid
HBSS	Hank's balanced salt solution
HGF	Hepatocyte growth factor
HL-1	Cardiac muscle cell line
hMSCs	Human mesenchymal stem cells
HUVEC	Human umbilical vein endothelial cells
HyD	Hybrid detector
ICAM-1	Intracellular adhesion molecule 1
IDO	Indoleamine 2,3-dioxygenase
IFN-γ	Interferon-γ
IGF-1	Insulin-like growth factor 1
IL-1β	Interleukin-1 β
IL-8	Interleukin-8
IMC	Integrated modulation contrast
ISCT	International Society for Cellular Therapy
LSFM	Light-sheet fluorescence microscopy
MEA	Microelectrode array
MI	Myocardial infarction
MMP-2	Matrix metalloproteinase 2
MOC	Manders overlap coefficient

MRI	Magnetic resonance imaging
MSCs	Mesenchymal stem cells
NA	Numerical aperture
NGF	Nerve growth factor
NO	Nitric oxide
PALM	Photoactivated localization microscopy
PBS	Phosphate buffered saline
PCC	Pearson's correlation coefficient
PCF	Photonic crystal fibre
PCM	Phase Contrast Microscopy
PDGF	Platelet-derived growth factor
PDL	Poly-d-lysine
PEG	Polyethylene Glycol
PEI	Polyethyleneimine
PGE-2	Prostaglandin E2
PLL	Poly-l-lysine
PMT	Photomultiplier tubes
PPV	Positive predictive value
RESOLFT	Reversible saturable optically linear fluorescence transitions
ROI	Region of interest
ROS	Reactive oxygen species
SAMN-R	Rhodamine-derived superparamagnetic maghemite nanoparticles
SDF-1	Stromal cell-derived factor 1
SEM	Scanning electron microscopy
SP	Spectral
SPION	Superparamagnetic iron oxide nanoparticles
SQUID	Superconducting quantum interference device
STED	Stimulated emission depletion microscopy
STORM	Stochastic optical reconstruction microscopy
TEM	Transmission electron microscope
TGF-β	Transforming growth factor-β
TNF-α	Tumour necrosis factor-α
TPR	True positive rate
VCAM-1	Vascular cell adhesion molecule 1
VEGF	Vascular endothelial growth factor
VN	Vitronectin
WLL	White light laser

LIST OF FIGURES

LIST OF TABLES